



# **Diploma Thesis**

# Respiratory airflow simulations and experiments investigating superimposed high-frequency jet ventilation

carried out for the purpose of obtaining the degree of Diplom-Ingenieur (Dipl.-Ing.) submitted at TU Wien, Faculty of Mechanical and Industrial Engineering

# Clemens Hochmayr, BSc.

Mat.Nr.: 11831646

under the supervision of Univ.Prof. Dipl.-Ing. Dr.techn. Margit Gföhler Institute of Engineering Design and Product Development

Ao. Univ.Prof. Dipl.-Ing. Dr.techn. Michael Harasek Institute of Chemical, Environmental & Bioscience Engineering

Vienna, 16.08.2023



# **Affidavit**

I declare in lieu of oath that I wrote this thesis and performed the associated research myself, using only literature cited in this volume. If text passages from sources are used literally, they are marked as such.

I confirm that this work is original and has not been submitted elsewhere for any examination, nor is it currently under consideration for a thesis elsewhere.

I acknowledge that the submitted work will be checked electronically-technically using suitable and state-of-the-art means (plagiarism detection software). On the one hand, this ensures that the submitted work was prepared according to the high-quality standards within the applicable rules to ensure good scientific practice "Code of Conduct" at the TU Wien. On the other hand, a comparison with other student theses avoids violations of my personal copyright.

Vienna, 08.08.2023

City and Date

Clemens Hochmayn Signature



# **Abstract**

**Introduction:** In mechanical ventilation, a machine takes over breathing for a patient. Superimposed high-frequency jet ventilation (SHFJV) is a mechanical ventilation technique that uses high-frequency jet ventilation (HFJV) and low-frequency jet ventilation (LFJV) simultaneously. While SHFJV has clinical fields of application, the exact mechanisms of action are still mostly unknown. The aim of this thesis is to investigate the impact of SHFJV on the lungs using fluid dynamics simulations and experiments.

**Methods:** An idealized lung model suitable for respiratory airflow studies was created. This model was used for computational fluid dynamics (CFD) simulations. After mesh independence studies, multiple CFD simulations mimicking different phases of SHFJV were performed employing three different turbulence models. Furthermore, micro particle image velocimetry (µPIV) experiments imitating airflow through lower airway bifurcations and alveoli were conducted to compare simulated and experimental results.

Results and Discussion: Simulation outcome analyses examining velocity-, turbulence-, and pressure distributions yielded reasonable results for all employed turbulence models. Experimentally determined velocity vector fields showed good agreement with the simulations in some respects, but also discrepancies. While the model could be implemented and verified well, more work and adjustments are necessary to truly validate simulation results.

Conclusion and Outlook: Comparison of the three turbulence models shows only minor differences in the flow field during SHFJV. Fluid flow is mostly laminar. However, areas of turbulence in the upper airways are still present. µPIV can be used to study SHFJV, but multiple methodological challenges arise. The idealized lung model can be verified and roughly validated, although not perfectly, as experimental results and simulated results show differences. Possible mechanical SHFJV effects can be mostly attributed to HFJV, while LFJV is more involved in gas exchange mechanisms. Further research is needed to confirm the reliability of the utilized methodology and the implied conclusions.

# **Acknowledgements**

First and foremost, I would like to express my gratitude to Margit Gföhler and Michael Harasek, my thesis supervisors, for their patient guidance, encouragements, and giving me the chance to work in a motivated team on a meaningful project.

Furthermore, my grateful thanks are extended to Seyyed Hossein Monsefi for his helpful advice and assistance regarding CFD simulations, and Theresia Baumgartner for her useful hints towards successful PIV experiments.

Moreover, I want to thank Clemens Mulley for providing his expertise and infrastructure with respect to additive manufacturing.

Finally, I wish to thank my parents, Gabriele and Alexander Hochmayr, as well as all my grandparents, for their unconditional support and encouragement throughout my studies.

# **Table of Contents**

1 Introduction	1
2 Theoretical Framework	3
2.1 Fundamental considerations of respiration and ventilation	3
2.1.1 Important aspects of the human respiratory system	3
2.1.2 Working principles of SHFJV	5
2.1.3 Mechanical modeling of the human lungs	8
2.2 CFD for respiratory airflow simulations	11
2.2.1 The CFD workflow	11
2.2.2 Governing equations for respiratory airflow simulations	13
2.2.3 RANS models for respiratory airflow simulations	16
2.2.4 LES models for respiratory airflow simulations	18
2.2.5 Meshing considerations for turbulent CFD simulations	20
2.2.6 Solver considerations for turbulent CFD simulations	23
2.3 PIV for respiratory airflow experiments	24
2.3.1 Functional concept of PIV	24
2.3.2 Tomographic 3D PIV	26
2.3.3 PIV for microfluid investigations	27
2.3.4 Use cases of PIV in respiratory research	28
3 Methods	30
3.1 Design: Idealized lung model for respiratory airflow studies	30
3.2 Implementation: Fluid dynamics simulations	32
3.2.1 Outline of the performed simulations	32
3.2.2 Mesh independence studies	36
3.2.3 Entirely laminar simulations	41
3.2.4 Combined SST $k$ - $\omega$ and laminar simulations	42
3.2.5 Combined LES and laminar simulations	43

· · · · · ·	44
3.3.1 Outline of the experimental µPIV setup	45
3.3.2 Design and manufacturing of the microchannels	46
3.3.3 Lower airway and alveolar µPIV experiments	50
4 Results and Discussion	53
4.1 Mesh independence studies	53
4.2 SHFJV simulations	56
4.2.1 Mean velocity distributions	57
4.2.2 Velocity fluctuations and turbulence properties	64
4.2.3 Pressure distributions	67
4.3 μPIV experiments	70
4.4 Comparison of simulated and experimental flow patterns	76
5 Conclusion and Outlook	79
5.1 Turbulence model influence on simulated SHFJV	79
5.2 Feasibility of PIV to study SHFJV	80
5.3 Verification and validation of the SHFJV CFD model	82
5.3 Verification and validation of the SHFJV CFD model	83
5.3 Verification and validation of the SHFJV CFD model	83
5.3 Verification and validation of the SHFJV CFD model	83 84 87
5.3 Verification and validation of the SHFJV CFD model	83 84 87
5.3 Verification and validation of the SHFJV CFD model	83 84 93 98
5.3 Verification and validation of the SHFJV CFD model	83 84 93 98
5.3 Verification and validation of the SHFJV CFD model  5.4 Implications for the mechanisms of action during SHFJV  5.5 Future perspectives and opportunities for improvement  List of References  List of Tables  List of Abbreviations	83849398100

# 1 Introduction

Mechanical ventilation is a form of life support, where a ventilator, also called respirator or breathing machine, takes over the work of breathing when a patient is not able to do so sufficiently on their own. Ventilators are generally used to deliver high concentrations of oxygen into the lungs and get rid of remaining carbon dioxide [1].

While most conventional ventilators work with respiration patterns mimicking physiological breathing, some novel approaches try to increase patient benefit by deliberately altering the ventilation pattern. One of these exceptions is the concept of SHFJV. It is a pressure driven ventilation technique that uses two jet streams with different frequencies simultaneously [2]. While the LFJV creates a breathing profile similar to that of normal human breathing, the HFJV superimposes this stream continuously with small sinusoidal pressure changes.

This ventilation technique already has some clinical fields of application and delivered promising results in the treatment of acute respiratory distress syndrome (ARDS), which is a life-threatening condition. In ARDS, due to inflammation of the lungs, further leading to the collapse of alveolar units, the lungs cannot provide the body enough oxygen. It is proposed that in patients with ARDS, SHFJV promotes the recruitment of collapsed alveoli, thereby reenabling the lungs to perform gas exchange. However, the exact consequences and mechanisms of action of SHFJV are still mostly unknown [3].

Current theories that provide a satisfactory explanation on how conventional ventilation works cannot be directly transferred to SHFJV. Especially, the detailed effects of the superimposed signal on the airflow in the respiratory airways and alveoli is an important area of interest and subject of future research.

Biomedical engineers and researchers are nowadays relying on computational tools to assist in predicting fluid flow such as air inside the human body. Simulations can provide information that is nearly impossible to be obtained experimentally [4]. In addition to these CFD approaches, a wide range of diagnostic methods for experimental fluidic research has been developed. One option is to use PIV to experimentally determine flow fields [5].

Combining modern fluid research methods with SHFJV, a previous diploma thesis written



at TU Wien [6] already aimed to find out more about the airflow in the upper airways during SHFJV by means of CFD. Building upon [6], in a preliminary project to the thesis at hand, a model of an entire lung branch suitable for CFD simulations was created. First airflow studies in the lower airways were conducted. Subsequently, the aim of this work is to improve the developed model and perform a more thorough analysis of the airflow during SHFJV.

Precisely, the following research questions have been defined to be answered by means of CFD simulations and PIV experiments:

- In CFD simulations, what influence does the chosen turbulence model have on the airflow in the lungs during SHFJV?
- Which PIV experiments can be performed to gain insight into the airflow behavior in the lungs during SHFJV?
- How does the CFD-simulated airflow compare to the PIV experiments?
- What conclusions can be made about the airflow behavior in the respiratory tract during SHFJV?



# 2 Theoretical Framework

In preparation for the practical model development, a thorough literature search was carried out. The aim of this measure was to obtain essential information about medical considerations of the lungs, SHFJV, common mechanical modeling types of ventilation, CFD, and PIV. Building on the presented fundamentals, a unique model, which is specially tailored to the task at hand, can subsequently be developed.

# 2.1 Fundamental considerations of respiration and ventilation

In order to conduct appropriate simulations and experiments, interdisciplinary knowledge from biomedical engineering and related areas is necessary. A combination of morphological, physiological, and pathological aspects, as well as physical basics of the human lungs must be considered. Furthermore, a certain understanding of practical applications of mechanical ventilation, especially SHFJV, is important.

## 2.1.1 Important aspects of the human respiratory system

Morphologically, the lungs consist of a highly branched bronchial system, at the end of which the alveoli dilate. The bronchial tree of the human lungs has 23 divisions on average (Figure 1). From the 16<sup>th</sup> division onwards, alveoli are formed, with the last divisions in particular ending in numerous alveoli. Accordingly, the airways of the first 15 generations represent the conducting airways, whereas the bronchioles and alveoli corresponding to the 16<sup>th</sup> to 23<sup>rd</sup> generation represent the acinar airways responsible for gas exchange [7].

The job of the bronchial system is to ensure adequate and uniform airflow towards the alveoli. The actual gas exchange between the alveolar air and the blood takes place exclusively in the alveoli. In this way, around 300 million alveoli with a total surface area of 80 to 100 square meters are formed. Due to the strong branching of the bronchial tree, there is an elevation of the effective area for gas exchange by a factor of about 1000 [8].

From a physiological viewpoint, it is important to mention that the volume of the lungs is made up of the anatomical dead space and the alveolar space. The anatomical dead space is about 150 milliliters in adults and extends from the mouth to the 16th division of the bronchial tree [8].

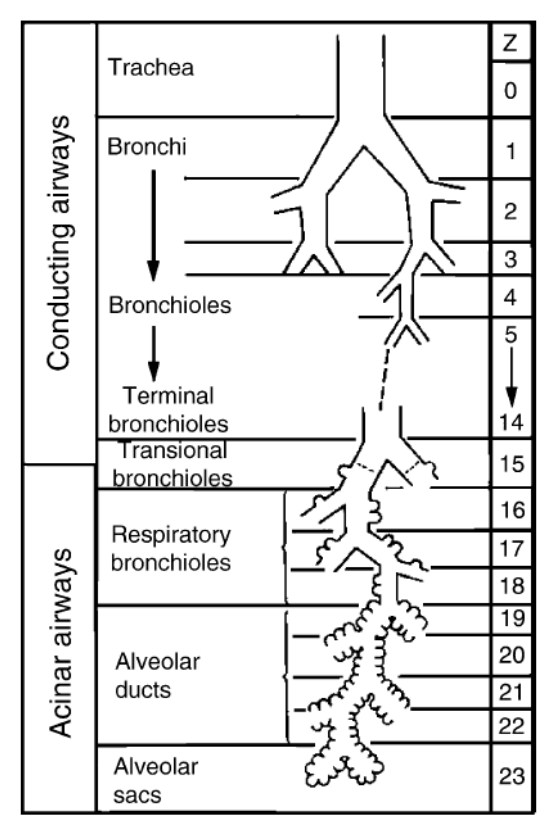


Figure 1: Sketch of human airway system with generations of branching from trachea to alveoli [9].

The alveolar space in adults is about 3 to 4 liters. Since the inhaled air always must pass through the anatomical dead space before it reaches the alveolar space, not the entire respiratory minute volume contributes to ventilation. The volume inhaled and exhaled with each breath is the called the tidal volume. It is around 0.5 liters at rest but can increase several times under load. At a breathing rate of about 15 breaths per minute, this results in a respiratory minute volume of 7.5 liters per minute [8].

Regarding the pathological aspects of the lungs, ARDS is a common cause for insufficient breathing. In ARDS, multiple pathomechanisms are responsible for serious morphological and functional changes in the lungs, so that adequate oxygenation of the patient using conventional ventilation is often no longer possible. Precisely, due to inflammation of the lung tissue, a permeability disturbance of the alveolar wall occurs. This disturbance promotes the development interstitial and intraalveolar edema, which in turn makes gas exchange considerably more difficult. Damage to the alveolar wall also leads to a decrease in surfactant production. Surfactant is a surface-active substance produced in the alveoli and secreted onto the surface of the alveolar epithelium. Since surfactant reduces the surface tension of the alveoli so that the lungs can unfold properly, a decreased surfactant production consequently leads to the collapse of alveoli or entire functional alveolar units [3].

#### 2.1.2 Working principles of SHFJV

In conventional pressure-controlled ventilation, the ventilator sets the airway pressure at the beginning of the trachea for any given time. This setting of an inspiratory pressure, as well as an associated positive end-expiratory pressure (PEEP) in the alveoli, generates a pressure gradient along which the airflow follows during inspiration and expiration. Often, this airflow is carried from the respirator to the patient via an endotracheal tube, which goes directly through the glottis into the trachea and represents a single air in- and outlet. Another conventional airway device is the laryngeal mask, which forms an airtight seal on top the glottis and represents a single air in- and outlet as well.

In SHFJV, however, two jet airstreams with different frequencies and pressures are applied. The most sophisticated SHFJV product line on the market today is the TwinStream jet ventilator series (Carl Reiner GmbH, Vienna, Austria). Oxygen provided by the TwinStream jet ventilator (Figure 2) reaches the patient via a jet laryngoscope (Figure 3) or a jet converter. The jet laryngoscope is a supraglottic airway device, consisting of a steel tube equipped with two nozzles integrated in the body for simultaneous administration of HFJV and LFJV. A third and fourth nozzle placed close to the tip of the device allow airway pressure- and gas concentration monitoring [2]. The jet converter is an adapter that can connect to any endotracheal tube or laryngeal mask, making it possible to use jet ventilation on a conventionally intubated patients [10].

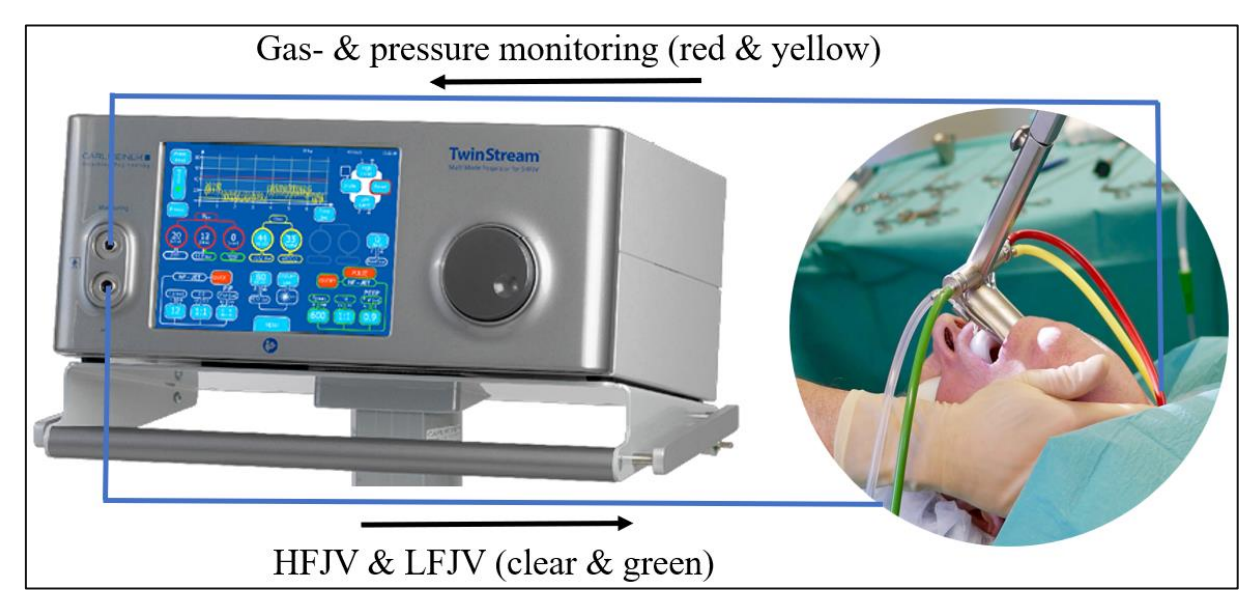


Figure 2: Working principle of the TwinStream ventilation system. SHFJV is performed via applying the highand low-frequency jet streams through the jet laryngoscope. By monitoring gas concentrations and pressure changes, a closed feedback loop is created. Modified after [11].

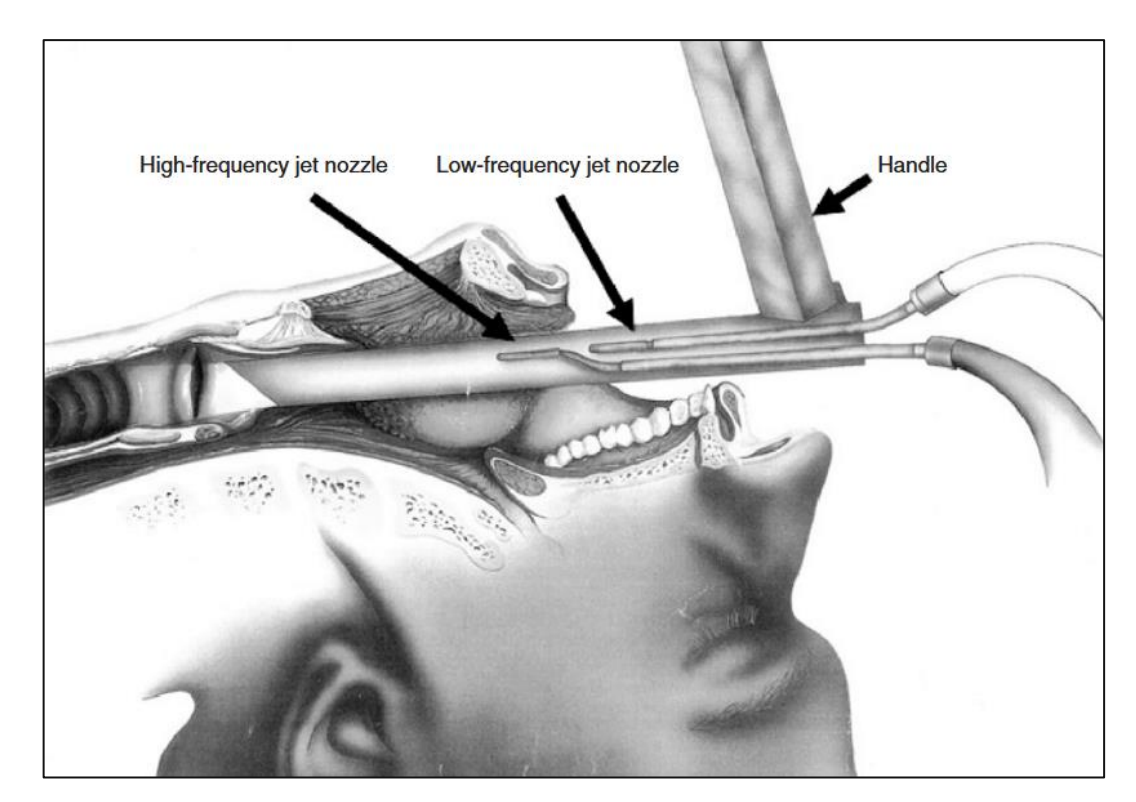


Figure 3: Schematic drawing of the jet laryngoscope. Two cannulas for HFJV and LFJV are integrated apart from each other. A third and fourth cannula (not shown in this figure) continuously measures pressure and gas concentrations at the tip [2].

The continuously pulsating high-frequency jet stream works at a frequency between 1.67 and 15 Hertz, corresponding to 100 to 900 breaths per minute. It is superimposed with the low-frequency jet stream at 0.167 to 0.2 Hertz. corresponding to 10 to 12 breaths per minute, generating the main inspiratory and expiratory pressure changes. The combination of these two streams results in phased airway pressure changes (Figure 4) analogous to conventional ventilation, but overlayed by permanent pressure fluctuations. The jet ventilations thereby also provide the upper and lower pressure levels [2].

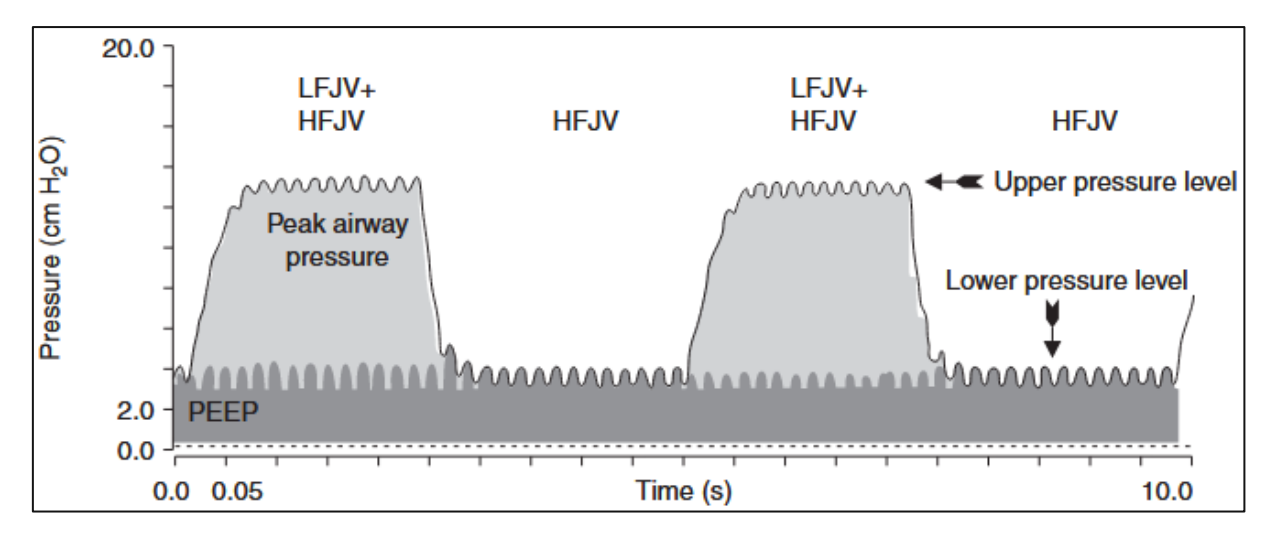


Figure 4: Symbolic pressure curve during SHFJV. Two cycles of LFJV are superimposed with continuous HFJV [2].

In patients with ARDS, methods of ventilation technology like SHFJV have been developed to make gas exchange more effective and to avoid the negative effects of high airway pressure on the lungs and cardiovascular system. In contrast to previously used volume-controlled forms of ventilation, which could not meet expectations, pressurecontrolled forms are now being used more and more [3].

There are different opinions about the mechanisms of action during SHFJV as a treatment for ARDS. Most users attribute the improved gas exchange under jet ventilation to an increased mean airway pressure and lower peak airway pressures. An increase in lung volume may be a direct result of HFJV. The increase in functional residual capacity reopens collapsed alveoli, thereby regaining the gas exchange surface lost to ARDS. The turbulent flow of the jet gas is also expected to result in better mixing of the respiratory gas and in a forced diffusion mechanism at the alveolar membrane. Impressive results in the treatment of ARDS with SHFJV have already been achieved in the clinical setting (Figure 5), showing an increase in ventilated lung areas through recruitment of collapsed alveoli [3].

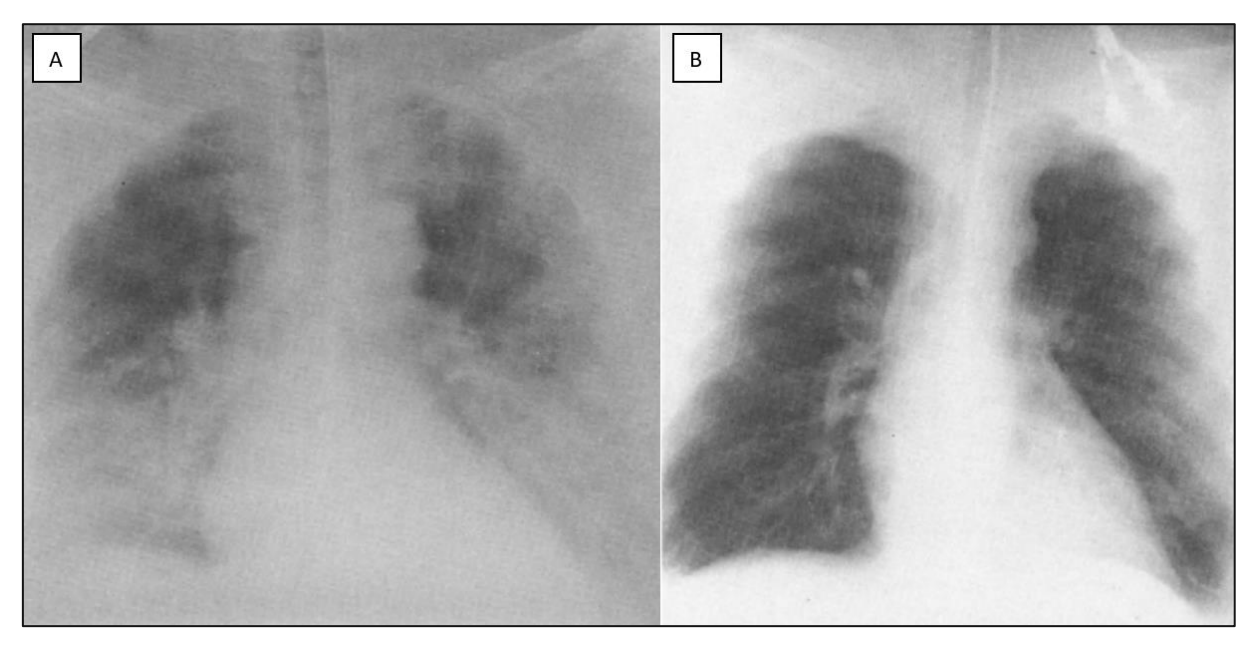


Figure 5: Lung X-ray of a patient with ARDS. Bright areas mark dense tissue or obstructions, while dark areas indicate cavities. A: Patient receiving conventional ventilation. B: The same patient after 24 hours of SHFJV. Modified after [3].

However, it must be noted that all current theories on mechanisms of action during SHFJV are not sufficiently proven jet. Even though practical results are promising, the goal to find detailed evidence for the validity of SHFJV is still subject of ongoing research.

#### 2.1.3 Mechanical modeling of the human lungs

The field of lung mechanics deals with pressures acting on the respiratory system and the changes in air volume that they produce. In mechanical ventilation, the ventilator and the respiratory system of the patient form a connected system. The static and dynamic behavior of this system can mathematically be described by an equation of motion. In lung physiology, the mechanical properties of the respiratory system are approximated using simple physical models. The simplest three-dimensional (3D) model of the respiratory system consists of a tube and an elastic balloon (Figure 6) [12].

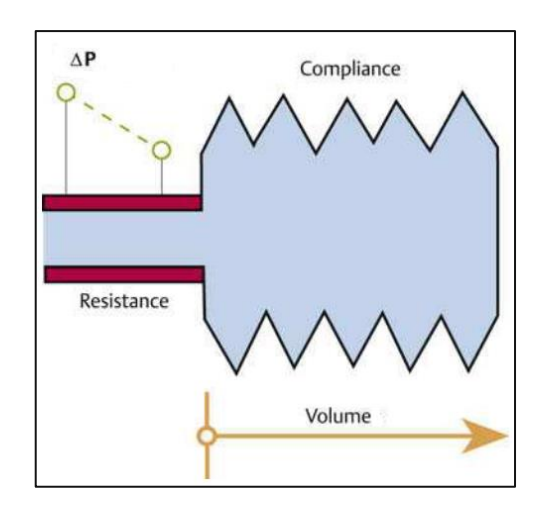


Figure 6: Physical model of the respiratory system composed of a cylindrical tube with resistance R and an elastic balloon with the compliance C. Modified after [13].

The sum of all passive mechanical properties of the respiratory system is assigned to two model components, tube and balloon. The flow resistance R of the tube describes the sum of all flow resistances of the entire respiratory system. The compliance  $\boldsymbol{c}$  of the balloon describes the sum of all elastic properties of the respiratory system. Constants for resistance and compliance can be approximated by clinical measurements [12].

If the system is given a pressure  $p_{in}$  from the outside, it changes its volume until the static alveolar pressure  $p_{alv}$  is equal to  $p_{in}$ . In order for the system to change its volume (for air to flow into the system), the pressure  $p_{in}$  must overcome opposite pressures, that of the tube (dynamic, resistive pressure  $p_{res}$ ) and that of the balloon (static, alveolar pressure  $p_{alv}$ ).  $p_{alv}$  depends on the momentary volume in the lungs V, while  $p_{res}$  depends on the change in volume, that is on the volume flow rate  $\dot{V}$ . This relationship is mathematically given through the following equation of motion [12]:

$$p_{in} = p_{alv}(V) + p_{res}(\dot{V}) = \frac{1}{C} * V \pm R * \dot{V}$$
(1)

depending on the direction of the volume flow, into or out of the respiratory system. For the situation of mechanical ventilation, equation (1) must be extended. If a PEEP is applied, the static pressure at the end of the expiration corresponds to the PEEP [12]:

$$p_{in} = \frac{1}{C} * V + PEEP \pm R * \dot{V}$$
 (2)

This also means that  $p_{in}$  only equals  $p_{alv}$  in the breaks between inspiration and expiration, where no volume flow is occurring. During inspiration and expiration, the alveolar pressure response  $p_{alv}$  can be expressed as:

$$p_{alv} = p_{in} \pm p_{res}(\dot{V}) = p_{in} \pm R * \dot{V}$$
(3)

This means that during the entire breathing cycle,  $p_{alv}$  lags behind the changing  $p_{in}$ . In other words,  $p_{alv}$  is shifted to the right along the x-axis compared to  $p_{in}$  by a specific time constant in a pressure over time plot, schematically shown in Figure 7.

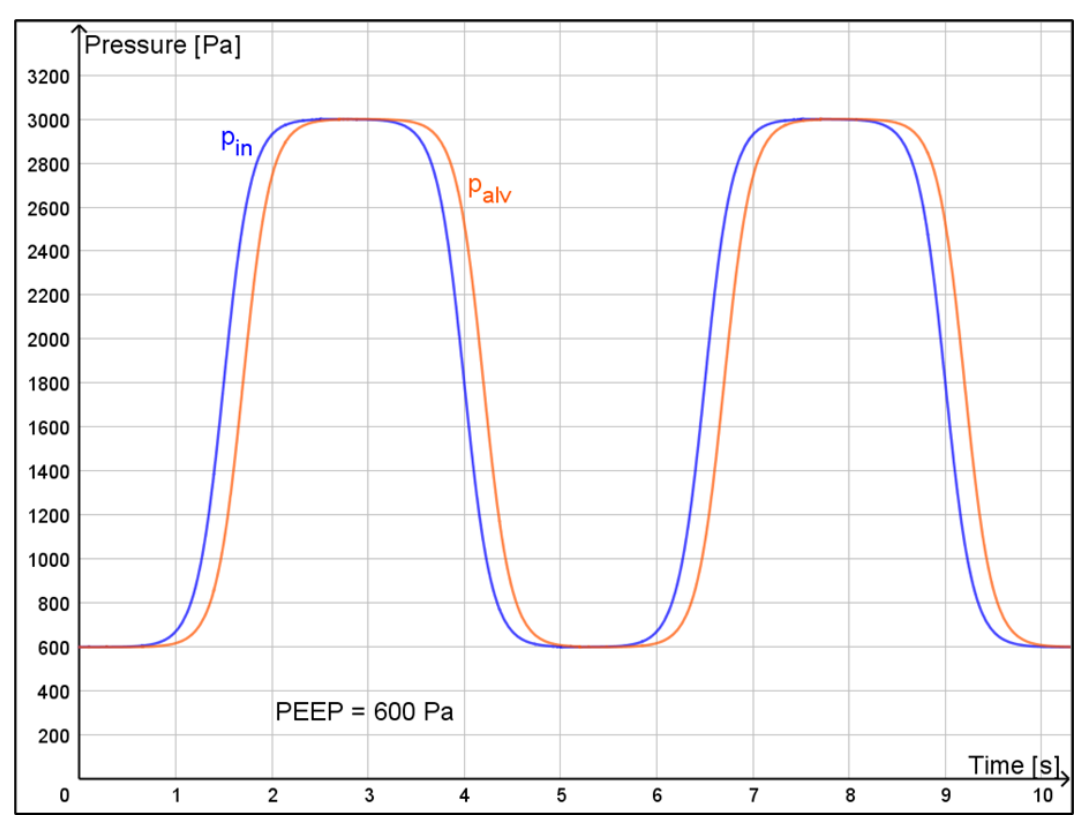


Figure 7: Schematic drawing of the alveolar pressure response without SHFJV. A pressure  $p_{in}$  is applied to the system from the outside. The static, alveolar pressure  $p_{alv}$  lags behind the changing  $p_{in}$ . When no volume flow is present,  $p_{in}$  equals  $p_{alv}$ .

While Figure 7 illustrates the principles of mechanical lung modeling well, the time- and pressure relations are not accurate. A more realistic depiction of  $p_{in}$  and  $p_{alv}$  for the case of SHFJV is described by the functions in Table 1 and depicted in Figure 8. Here, pressure changes  $p_{in}$  resulting from LFJV and HFJV have been considered. The delay of  $p_{alv}$ amounts to 0.002 seconds. This has been shown to be a plausible value for the time it takes until the alveoli react to an applied pressure and corresponds to a reasonable tidal volume.

Time [s]	Inlet- & alveolar pressure [Pa]		
t < 2.5	$p_{in} = 1800 + 1200 \tanh(3.5 (t - 1.5)) + 100 \times \sin(20 \pi t)$		
<i>t</i> < 2.5	$p_{alv} = 1800 + 1200 \times \tanh(3.5 \times (t - 1.502)) + 100 \times \sin(20 \times \pi \times (t - 0.002))$		
$2.5 \le t < 5$	$p_{in} = 1800 - 1200 \tanh(3.5 (t - 4)) + 100 \times \sin(20 \pi t)$		
	$p_{alv} = 1800 - 1200 \times \tanh(3.5 \times (t - 4.002)) + 100 \times \sin(20 \times \pi \times (t - 0.002))$		
$5 \le t < 7.5$	$p_{in} = 1800 + 1200 \tanh(3.5 (t - 6.5)) + 100 \times \sin(20 \pi t)$		
	$p_{alv} = 1800 + 1200 \times \tanh(3.5 \times (t - 6.502)) + 100 \times \sin(20 \times \pi \times (t - 0.002))$		
7.5 ≤ t	$p_{in} = 1800 - 1200 \tanh(3.5 (t - 9)) + 100 \times \sin(20 \pi t)$		
	$p_{alv} = 1800 - 1200 \times \tanh(3.5 \times (t - 9.002)) + 100 \times \sin(20 \times \pi \times (t - 0.002))$		

Table 1: Time-dependent functions mimicking the pressure profile from the TwinStream jet ventilator and the according alveolar pressure response.

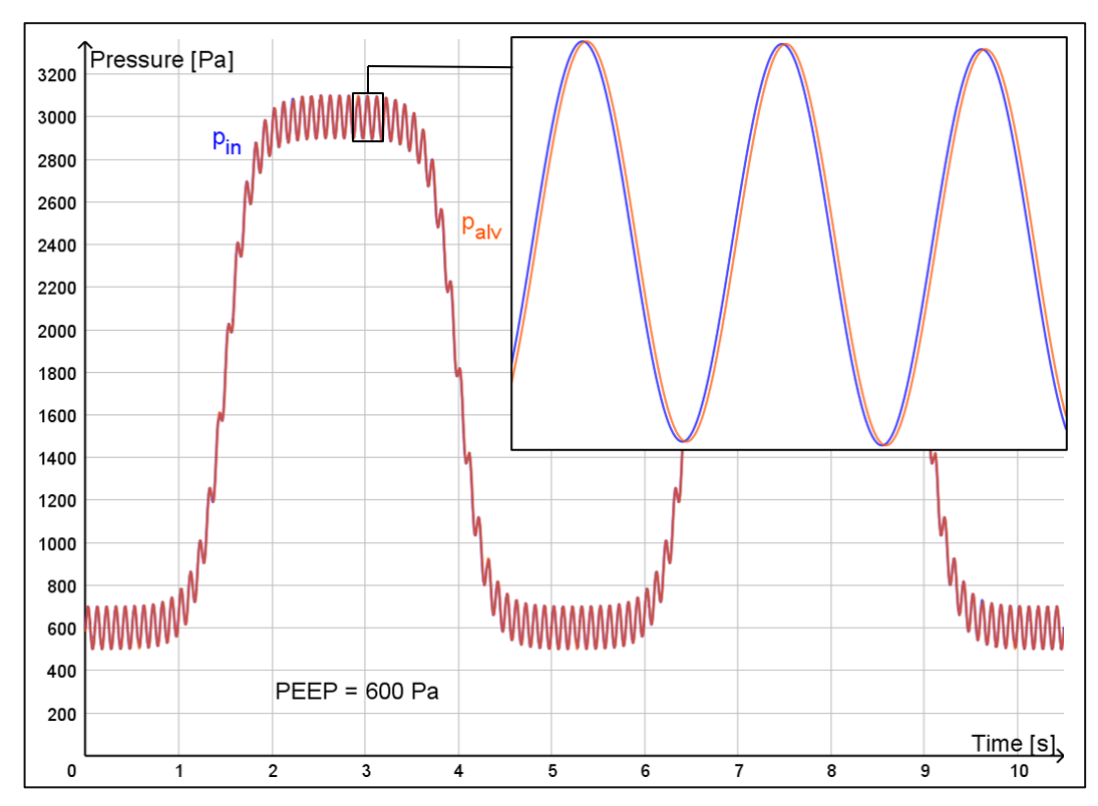


Figure 8: Graphical representation of the pressure profiles  $p_{in}$  and  $p_{alv}$  for SHFJV. Although it might look like  $p_{in}$  and  $p_{alv}$  are identical,  $p_{alv}$  is shifted to the right along the x-axis by 0.002 seconds, creating a delayed pressure response. In a more detailed view, this shift is visible.

However, it should be mentioned that equations (2) and (3) are only suitable for uniform whole-lung models. In reality, different lung sections show different resistance and compliance values. This causes asynchronous alveolar pressure responses and therefore asynchronous filling and emptying of lung areas during inspiration and expiration [3].

## 2.2 CFD for respiratory airflow simulations

Simulation tools are nowadays a valuable asset to assist in predicting the behavior of airflow in the human lungs. CFD can provide essential insights by simulating the entire respiratory airflow, from the conductive airways and down into the acinar system [4]. In this chapter, the general CFD workflow is explained. Moreover, governing equations for laminar and turbulent biomedical airflow simulations, turbulence models, as well as practical considerations regarding meshing and solver settings are presented.

#### 2.2.1 The CFD workflow

Fluid dynamics is essentially the study of fluids in motion. The physical characteristics of fluid movement can be described with mathematical expressions, specifically partial differential equations. These equations govern the motion in CFD simulations and are hence called governing equations. The prefix "computational" means that the equations are solved through numerical simulations, which involves using computers and software to obtain the numerical solutions. Next to experimental fluid dynamics and analytical fluid dynamics, numerical CFD approaches have become one of the three basic methods to solve fluid dynamics problems. A typical CFD solution procedure generally involves three main elements: Preprocessing, solving, and postprocessing (Figure 9) [4].

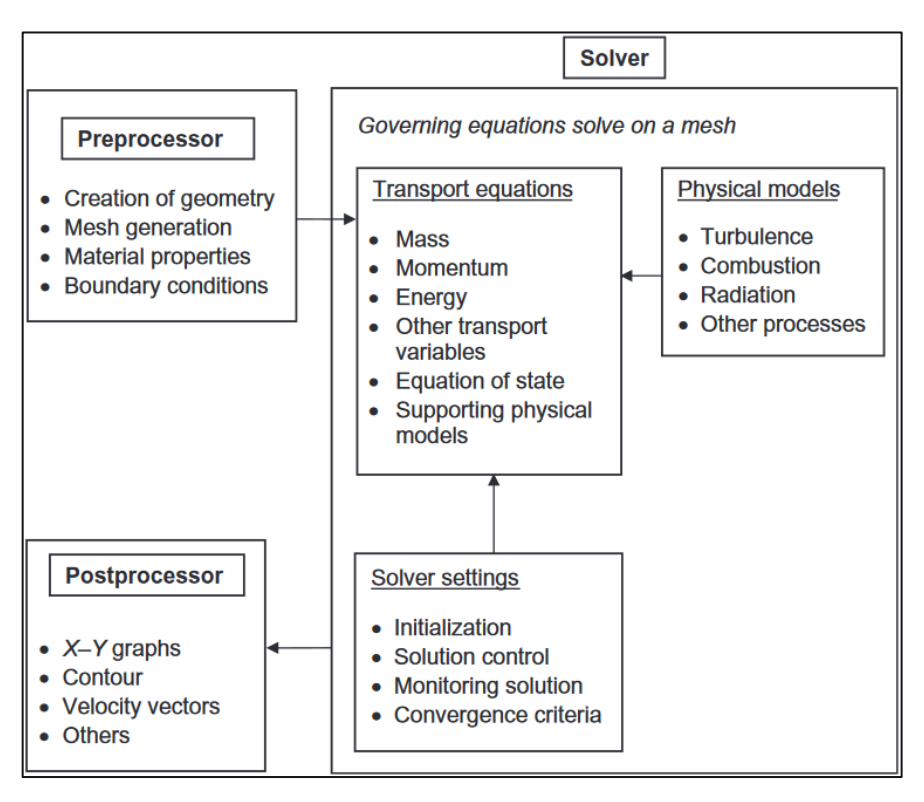


Figure 9: Framework of the three main elements and tasks handled within a CFD analysis [4].

In preprocessing, usually the following steps are worked off in the listed order:

- Geometry: The first step in any CFD analysis is the definition and creation of a geometry of the flow region. Software for computationally aided design (CAD) may be used to construct such a structure. The designed geometric model is the computational domain for the fluid flow during CFD calculations [4, 14].
- Meshing: To solve the governing equations within the created geometry, CFD requires the subdivision of the geometry into smaller domains. This results in the generation of a fine, non-overlapping grid, also known as mesh, consisting of cells, also known as elements or control volumes, for the entire domain. Depending on their shape, different types of mesh elements can be distinguished (Figure 10). The fluid flow in each of these cells is later solved numerically, which yields the approximate solution to the flow problem [4].

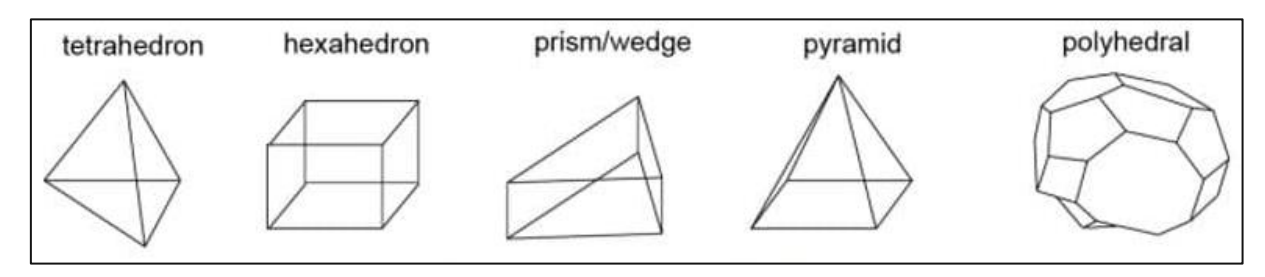


Figure 10: Different types of mesh elements, which can be seamlessly combined to fill up the fluid flow domain. Modified after [15].

- Physics and fluid properties: Underlying flow physics are unique to every fluid flow system. It must be initially declared whether simulations are for transient, meaning unsteady, or steady solutions. Subsequently, definitions about the type of the fluid motion must be made. For instance, the flow can be inviscid or viscous, compressible or incompressible, and laminar or turbulent. Also, the transport of heat as a form of energy may contribute to the flow [4, 16].
- Boundary conditions: Due to the complex nature of fluid dynamics, chosen boundary conditions have major implications on the flow development. By setting appropriate conditions mimicking the real physical boundaries of the fluid flow, a solvable CFD problem is generated. There need to be inflow and outflow boundaries within the flow domain. They are required to determine the fluid behavior entering and leaving the flow domain. Additionally, to ensure accurate modeling of fluid flow, it is necessary to specify suitable boundary conditions for both solid walls that enclose the flow geometry and any internal obstacles within the flow domain [4, 14].



The second major element of a CFD process is solving the defined problem. Due to the inherent complexity and non-linearity of physical phenomena in fluid flows, an iterative solution approach is typically necessary to resolve the key phenomena [16]. This solution process includes two essential actions within the CFD solver:

- Initialization: The iterative procedure generally needs all the discrete values of the flow properties, such as velocity or pressure, to be initialized before calculating a solution [4].
- Solution control: The most common way to control the solving process is by monitoring convergence. Convergence can be checked by progressively tracking the imbalances of the algebraic equations through each iteration step. These imbalances, represented by residuals, measure the overall conservation of the flow properties. Downward tendencies in the residuals suggest the removal of any imbalances, thereby causing the iterative process to converge. A converged solution is achieved when the residuals fall below some preset convergence criteria [4].

Besides examining residuals, other possibilities to assure the convergence of the numerical computations exist. For example, the selection of an appropriate solver algorithm or of underrelaxation factors can significantly facilitate the progress towards a converged solution. Underrelaxation means limiting the amount by which a variable changes from the previous iteration to the next one. Another option helping towards faster convergence is choosing a suitable timestep size for transient simulations [4].

Postprocessing, as the third and final major element, describes reporting and visualizing the resulting data. Some essential computer-graphical techniques frequently encountered in the presentation of CFD results include two-axis plots, vector plots, contour plots, the depiction of streamlines, or even animations. Reporting alphanumerical data is also possible, but impractical on a mesh that may consist of millions of grid points. A more reasonable approach is to check data only on a few predefined regions of interest [4, 14].

# 2.2.2 Governing equations for respiratory airflow simulations

Now that the major elements of a typical CFD solution procedure are clarified, it is valuable to take a closer look at the governing equations of fluid dynamics. For the thesis at hand, it would be out of scope to derive the entirety of the governing equations. However, it is

suitable to express them and the balance principles that they result from. Understanding these mathematical statements is useful, because CFD is fundamentally based on them [4].

The governing equations of fluid flow, namely the continuity equation, the momentum equations, and the energy equation, represent the conservation laws of physics. Additional terms and transport equations for describing turbulent flows can also be added to the set of governing equations [14]. The energy equation only needs to be invoked in CFD simulations, if heat transfer considerations are essential, whereas the continuity and momentum equations are generally necessary to guide the flow [17]. Since heat energy transfer is not important for the thesis at hand, the energy equation will not be further discussed.

The concept of mass conservation states that matter may neither be created nor destroyed. Consequently, the rate of change of mass in a control volume equals the net rate at which mass enters and leaves the control volume [4]. In other words, the mass flow through a volume element equals the difference between inflow and outflow. Assuming incompressible fluid flow, and taking into account that incompressible flows are characterized by a constant density, further considerations yield the partial differential continuity equation [18]:

$$\nabla \cdot \underline{u} = \mathbf{0} \tag{4}$$

where at any point in the flow field the velocity vector **u** consists of the local velocity components u, v, w, which are dependent on location x, y, z and time t [4].

Regarding the momentum equations of fluid flow, principles of force balance are applied. According to Newton's second law of motion, the sum of forces acting on the fluid element equals the product between mass and acceleration of the element [4]. Equations derived from this fundamental law describe the conservation of momentum in fluid flow problems and are also known as the Navier-Stokes equations. For a constant property fluid flow, which implies that the density  $\rho$  and dynamic viscosity  $\mu$  are constants, and in the absence of body forces including gravity, the partial differential Navier-Stokes equations for an incompressible flow can be reduced to [16]:

$$\rho \left( \frac{\partial \underline{u}}{\partial t} + \underline{u} \cdot \nabla \underline{u} \right) = -\nabla p + \mu \nabla^2 \underline{u}$$
 (5)

As aforementioned, flows in the laminar regime are completely described by the continuity

equation (4) and momentum equations (5). For some research purposes regarding airflow through the lungs, like [19, 20], a laminar description is sufficient. However, most flows examined in biomedical engineering are inherently turbulent. The turbulent flow regime presents, therefore, not only theoretical interest but also practical challenges. Disturbances within a laminar flow can lead to random, chaotic motion, also known as turbulence [18]. Formation of turbulence depends on the Reynolds number **Re**, indicating the ratio of inertia force to viscosity [4]:

$$Re = \frac{Inertia\ Force}{Friction\ Force} = \frac{\rho uL}{\mu}$$
 (6)

where u is the scalar flow speed and L the characteristic linear dimension.

At low **Re**, disturbances are dissipated away, meaning the flow stays laminar. At high **Re**, inertia forces are large enough to intensify disturbances, meaning a switch to turbulence occurs. Here, all flow properties vary randomly and in a chaotic way [4].

Despite the current state-of-the-art computing power, the computational demands for a direct numerical solution of fully turbulent flows are still tremendous. Nevertheless, this limitation can be avoided by applying averaging operations [4].

A popular option to obtain mean quantities in turbulent problems is Reynolds-averaging, also known as time-averaging. This process can be applied on the governing equations for incompressible, turbulent flows, producing the Reynolds-averaged continuity equation and Reynolds-averaged Navier-Stokes (RANS) equations [18]:

$$\nabla \cdot \overline{\underline{u}} = \mathbf{0} \tag{7}$$

$$\rho \left( \frac{\partial \overline{\underline{u}}}{\partial t} + \underline{\overline{u}} \cdot \nabla \underline{\overline{u}} \right) = -\nabla \overline{p} + \mu \nabla^2 \underline{\overline{u}} + \nabla \underline{\underline{\tau}}$$
(8)

in which the crossbar above symbols represents mean quantities and  $\underline{\boldsymbol{\tau}}$  is the symmetrical second-rank Reynolds stress tensor, emerging from the time-averaging operations. The RANS equations are similar to those formulated for laminar flows (4, 5), except for the presence of  $\underline{\underline{\tau}}$ . As a result, nine additional terms, called the Reynolds stresses, arise in the momentum equations. Since  $\underline{\underline{\tau}}$  is symmetrical, they represent six unknowns. Due to the unknown Reynolds stresses, the system of equations is no longer closed. In order to get back to a mathematically solvable system, a turbulence model is required [14].



#### 2.2.3 RANS models for respiratory airflow simulations

The turbulence model provides additional model equations that trace the unknown Reynolds stresses back to known flow variables [14]. For instance, the stress created by turbulent motion of vortices can be viewed to be analogous to the viscous stress induced by the chaotic motion of molecules. This method of estimating Reynolds stresses is referred to as an eddy viscosity model [21]. Using this approach for modeling turbulence, one can write  $\underline{\boldsymbol{\tau}}$  in the RANS equations (8) as:

$$\underline{\underline{\tau}} = \mu_t \left( \nabla \underline{\underline{u}} + (\nabla \underline{\underline{u}})^T - \frac{1}{3} (\nabla \cdot \underline{\underline{u}}) \underline{\underline{I}} \right) - \frac{2}{3} \rho k \underline{\underline{I}}$$
(9)

In this equation,  $\underline{\underline{I}}$  is the second-rank identity tensor,  $\underline{k}$  the turbulence kinetic energy, and  $\mu_t$  is the turbulent eddy viscosity. Now that the Reynolds stresses are remodeled,  $\mu_t$  must be described to simulate flow problems. Depending on the specific model choice,  $\mu_t$  can be expressed as an algebraic term combining model-specific variables and several additional constants [21].

Within modeling turbulent eddy viscosity  $\mu_t$ , it is possible to accommodate the turbulence kinetic energy k and the rate of dissipation of turbulence kinetic energy  $\varepsilon$  [21]. This socalled standard  $k-\varepsilon$  model [22] is commonly used in many turbulent fluid engineering problems. k and  $\varepsilon$  are determined by solving two additional partial differential equations, consisting of known variables and adjustable constants [4]:

$$\rho \left( \frac{\partial k}{\partial t} + \nabla \cdot \left( \underline{\overline{u}} k \right) \right) = \nabla \cdot \left( \left( \mu + \frac{\mu_t}{\sigma_k} \right) \nabla k \right) + P_k - \rho \varepsilon$$
 (10)

$$\rho\left(\frac{\partial \varepsilon}{\partial t} + \nabla \cdot \left(\underline{\overline{u}}\varepsilon\right)\right) = \nabla \cdot \left(\left(\mu + \frac{\mu_t}{\sigma_{\varepsilon}}\right)\nabla \varepsilon\right) + C_{1\varepsilon}P_k\frac{\varepsilon}{k} - C_{2\varepsilon}\rho\frac{\varepsilon^2}{k}$$
(11)

In the equations above,  $P_k$  represents the production of turbulence kinetic energy k.  $C_{1\varepsilon}$ ,  $C_{2\varepsilon}$ ,  $\sigma_k$  and  $\sigma_{\varepsilon}$  are adjustable model constants, whose values are empirically determined and usually do not need to be changed. The turbulent viscosity  $\mu_t$  in the k- $\varepsilon$  model is then given by [4]:

$$\mu_t = \rho C_\mu \frac{k^2}{\varepsilon} \tag{12}$$



where  $C_{\mu}$  is also an adjustable, empirical constant.

Another popular approach to model eddy viscosity is the  $k-\omega$  model [23, 24], which uses the specific rate of dissipation of turbulence kinetic energy  $\omega$ , which can also be thought of as the ratio of  $\varepsilon$  to k. Again, the two eponymous variables can be calculated through two additional partial differential equations [18]:

$$\rho\left(\frac{\partial k}{\partial t} + \nabla \cdot \left(\underline{\underline{u}}k\right)\right) = \nabla \cdot \left((\mu + \sigma_k \mu_t)\nabla k\right) + P_k - \rho \beta^* k \omega \tag{13}$$

$$\rho\left(\frac{\partial\omega}{\partial t} + \nabla\cdot\left(\underline{\overline{u}}\omega\right)\right) = \nabla\cdot\left((\mu + \sigma_{\omega}\mu_{t})\nabla\omega\right) + \gamma\frac{\omega}{k}P_{k} - \rho\beta\omega^{2}$$
(14)

Here,  $\sigma_k$ ,  $\sigma_\omega$ ,  $\boldsymbol{\beta}^*$ ,  $\boldsymbol{\beta}$ , and  $\boldsymbol{\gamma}$  are once again empirical, adjustable model constants. For the k- $\omega$ model,  $\mu_t$  is then calculated as [18]:

$$\mu_t = \rho \frac{k}{\omega} \tag{15}$$

Through further mathematical refinements, one can improve the standard  $k-\varepsilon$  and  $k-\omega$ models to suit a given problem adequately. There is an abundance of such eddy viscosity models developed through mathematical improvements [21]. In the following, however, only the models used in fluid dynamics simulations of the lungs are presented.

For instance, the  $k-\varepsilon$  and  $k-\omega$  approaches can be combined to represent realistic flows even better. A sophisticated version of an eddy viscosity model is the shear stress transport (SST) **k-\omega** model [25]. The SST **k-\omega** model implements a gradual change from the **k-\omega** model in the inner boundary layers to a high Reynolds number version of the  $k-\varepsilon$  model in the outer boundary layers. This is done by using a transition function  $F_1$ , which blends the modelspecific partial differential equations and respective empirical constants together. Also, a modified  $\mu_t$  is used in the SST k- $\omega$  model to include transport effects of turbulent shear stress [21]:

$$\mu_t = \alpha \rho \frac{k}{max(\alpha \omega, SF_2)} \tag{16}$$

In this formulation of  $\mu_t$ ,  $\alpha$  is another constant, S is the modulus of the mean strain-rate tensor, and  $F_2$  is a second blending function. Multiple works, such as [6, 26-30], apply the SST k- $\omega$  model to study fluid dynamics of the human respiratory tract.

Another example for a considerable eddy viscosity model is the renormalization group (RNG)  $k-\varepsilon$  model [31]. It is similar to the standard model,  $k-\varepsilon$  model, but has an extra term in its  $\varepsilon$ -equation. Swirl effects are included, enhancing accuracy. The RNG theory provides an effective  $\mu_t$  that accounts for low Re effects. Nevertheless, reasonable usage depends on an suitable treatment of the near-wall region [21]. Scientific reports such as [26, 28] use the RNG  $k-\varepsilon$  model to investigate airflow patterns in the human lungs.

Furthermore, the realizable  $k-\varepsilon$  model [32] may be suitable. It is intended to address deficiencies by adopting a new formula for  $\mu_t$ , and a new model equation for  $\varepsilon$ . Publications using the realizable  $k-\varepsilon$  model to characterize lung airflow include [33, 34].

Moreover, the low Reynolds number (LRN)  $k-\omega$  model [24], within which damping of  $\mu_t$ causes a flow correction at low **Re** very close to the wall should be mentioned [21]. The LRN  $k-\omega$  model is also commonly used for human lungs CFD simulations [33, 35].

### 2.2.4 LES models for respiratory airflow simulations

Advanced approaches for solving turbulent flows do not entirely rely on modeling  $\underline{\tau}$ . For instance, in a large eddy simulation (LES), the Reynolds stresses for large vortices are directly numerically resolved and only small vortices are incorporated through an eddy viscosity model. In LES, large-scale vortices typically have sizes larger than the grid resolution. The spatial filtering operation in LES is therefore called grid-averaging, as opposed to temporal Reynolds-averaging [18]. Grid-averaging is done by low pass filtering the governing equations for incompressible, turbulent flows. Through this operation, the smallest length scales are ignored by effectively removing small-scale information from the solution. However, to obey conservation laws this lost information has to be modeled again, using eddy viscosity  $\mu_t$  [14].

Scales that are directly solved are called grid-scales or the resolvable scales. Small scales, which are not captured by the grid are referred to as subgrid-scales or residual scales (Figure 11) [18, 21]. While the grid-scale Reynolds stresses are directly resolved, the unknown subgrid-scale stresses resulting from filtering require modeling. Consequently, in order to obtain a reasonable solution, LES requires very fine meshes, drastically increasing the computational resources needed [21]. As a rule of thumb, for a good solution, at least 80 percent of the total turbulence kinetic energy should be directly resolved, while maximally 20 percent should be incorporated through an eddy viscosity model [36].

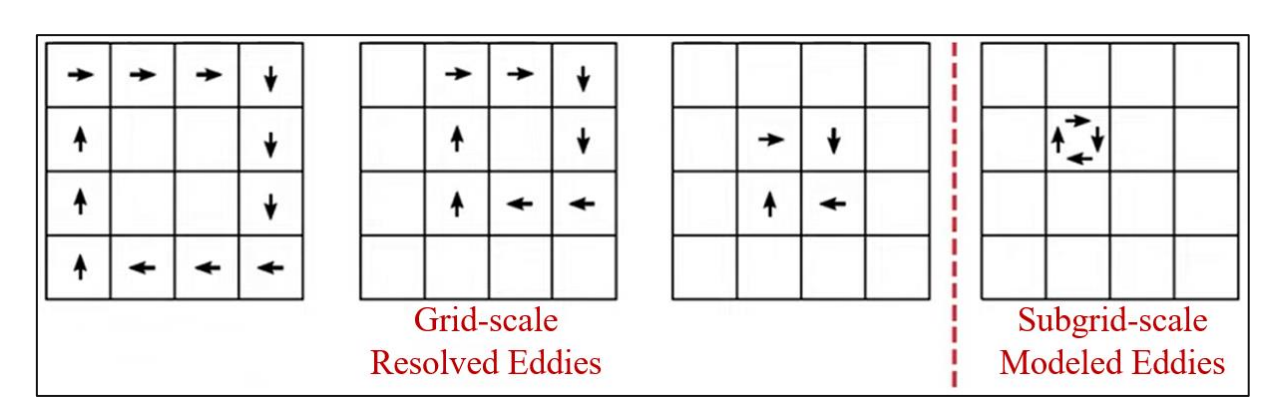


Figure 11: Comparison between differently sized vortices, represented by closed arrow loops. While those spanning over four or more mesh cells are directly resolved, smaller ones must be modeled. Modified after [36].

The most widely used subgrid-scale model is the Smagorinsky model [37]. Since it builds upon the eddy viscosity idea, it shares similarities to RANS models. The difference lies in the evaluation of  $\mu_t$ . While LES determines  $\mu_t$  directly from the filtered velocity field, RANS calculates  $\mu_t$  through additionally derived variables, namely k and  $\varepsilon$  or  $\omega$  [4].

An advancement of the Smagorinsky model is the wall adapting local eddy viscosity (WALE) model [38]. As opposed to the Smagorinsky model, the WALE model returns a zero-valued  $\mu_t$  for laminar flows, allowing correct treatment of laminar zones. Hence, the WALE model is advantageous for problems with both laminar and turbulent zones [21].

Summarizing, a synopsis of applicable models for respiratory airflow simulations is shown in Table 2. The RANS and LES model approaches are schematically outlined in Figure 12. In today's research, advances in computational power are establishing LES as a reasonable modeling approach for many turbulent CFD problems. Obtaining high-quality and highaccuracy solutions is possible, hence, this technique might gradually replace traditional two-equation RANS models [4]. Nonetheless, while widely used in academics, LES has a limited area of use in industrial simulations. The reason is the high-resolution requirement for wall boundary layers, resulting in vast computation times [21]. Modern studies applying LES for research of respiratory airflow include [39-43], for instance.

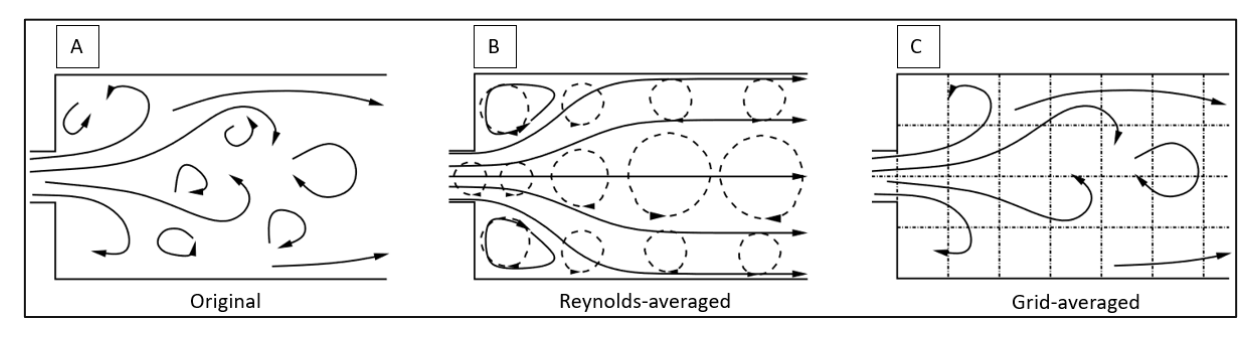


Figure 12: Schematic comparison of turbulence mode types. A: An original flow field, B: Its RANS model via Reynolds-averaging, C: Its LES model via grid-averaging. Modified after [14].

Model type	Specific model	Overview	Used for respiratory fluid dynamics by
Laminar	-	<ul><li>Laminar flow model</li><li>Fluid following smooth paths in layers</li></ul>	Tsega 2018 [19] Koullapis et al. 2020 [20]
RANS	RNG <b>k-ε</b>	<ul> <li>k-ε two equation turbulence model</li> <li>Extra term in ε-equation</li> <li>Swirl effects included</li> <li>Reasonable for low Re flows</li> </ul>	Phuong, Kazuhide 2015 [26] Xu et al. 2020 [28]
	Realizable <b>k-ε</b>	<ul> <li>k-ε two equation turbulence model</li> <li>Alternative formulations for μ<sub>t</sub> and ε</li> <li>Substantial improvements over standard k-ε model</li> </ul>	Srivastav et al. 2019 [33] Rahman et al. 2022 [34]
	LRN <b>k-ω</b>	<ul> <li>k-ω two equation turbulence model</li> <li>Damping of μ<sub>t</sub> causes flow correction at low Re close to the wall</li> </ul>	Srivastav et al. 2019 [33] Kim, Ramana 2021 [35]
	SST k-ω	<ul> <li>Combination of standard k-ε and k-ω two equation turbulence models</li> <li>Changes from k-ω in inner boundary layers to k-ε in outer boundary layers</li> <li>Includes shear stress transport in μ<sub>t</sub></li> </ul>	Phuong, Kazuhide 2015 [26]  Sul et al. 2018 [27]  Xu et al. 2020 [28]  Gemci et al. 2022 [29]  Wedel et al. 2022 [30]
LES	-	<ul> <li>Large eddy simulation turbulence model</li> <li>Directly resolves large vortices</li> <li>Models small vortices using eddy viscosity</li> </ul>	Gemci et al. 2008 [39] Radhakrishnan, Kassinos 2009 [40] Alzahrany et al. [41] Calmet et al. 2016 [42] Cui et al. 2021 [43]

Table 2: Outline of applicable fluid flow models for respiratory CFD simulations.

### 2.2.5 Meshing considerations for turbulent CFD simulations

To obtain meaningful results from CFD simulations, several practical considerations next to the turbulence model must be taken into account. Most importantly, well thought-out mesh generation is crucial for solution convergence and good results. In practice, this means minding element types, quality, and size, as well as ensuring mesh independence.

Mesh quality can be assessed using different criteria, such as skewness, aspect ratio, or orthogonal quality. Skewness determines how close to an ideal equilateral and equiangular building block a cell is. Aspect ratio describes the ratio of the longest edge of an element to its shortest edge. Orthogonal quality of elements is computed using multiple vectors between a cell's centroid, its faces, and neighboring cell's faces. The angles between those vectors are calculated. The closer they come to a right angle, the better the orthogonal quality of the element [44].

Generally, by reducing element size, mesh quality can be increased. However, a large number of cells drastically increases computation time [44]. A reasonable compromise could therefore be to locally refine the mesh in areas where high velocity gradients or strong vortices are expected. Furthermore, when sizing the mesh for a time-transient simulation, the Courant-Friedrichs-Lewy (CFL) convergence condition [45] must be taken into consideration. For the 3D case, the CFL condition states:

$$c = u \frac{\Delta t}{\Delta x} + v \frac{\Delta t}{\Delta y} + w \frac{\Delta t}{\Delta z} \le c_{max}$$
 (17)

where c is known as the Courant number or CFL number. Basically, this equation states that for given velocity components u, v, w in a transient problem, the discrete distances  $\Delta x$ ,  $\Delta y$ ,  $\Delta z$  covered by the fluid, and the discrete timestep  $\Delta t$  must not exceed certain values to achieve a converged solution [4]. In other words, assuming known velocity, smaller meshes require smaller timesteps for a stable transient solution, while coarser meshes can be handled with larger timesteps. The specific value of  $c_{max}$  depends on the employed algebraic solver method. For explicit solving algorithms,  $c_{max}$  equals 1. Implicit matrix solvers are more robust towards numerical instability, hence larger values of  $c_{max}$  up to 20 may be acceptable [4, 14].

Also, adequate boundary layer resolution of the mesh is critical. Near walls, turbulent flow is guided by the law of the wall [46]. It states the relation between the dimensionless velocity  $u^+$  at a certain point and the dimensionless distance  $y^+$  from that point to the wall. For values of  $y^+ < 5$  dimensionless wall units, one speaks of the viscous sublayer, where  $u^+$  and  $y^+$  scale linearly. Meanwhile, values of  $30 < y^+$  designate the log-law region, where  $u^+$  scales proportionally to the logarithm of  $v^+$  [14, 18]:

$$u^{+} = \begin{cases} y^{+}, & y^{+} < 5\\ \frac{1}{\kappa} \ln(y^{+}) + B, & 30 < y^{+} \end{cases}$$
 (18)

In the formulation of the log-law region,  $\kappa$  and B are both constants. The region in between,  $5 < y^+ < 30$ , is known as the buffer layer. Here, neither approximation holds [14]. A schematic representation of the law of the wall is depicted in Figure 13.

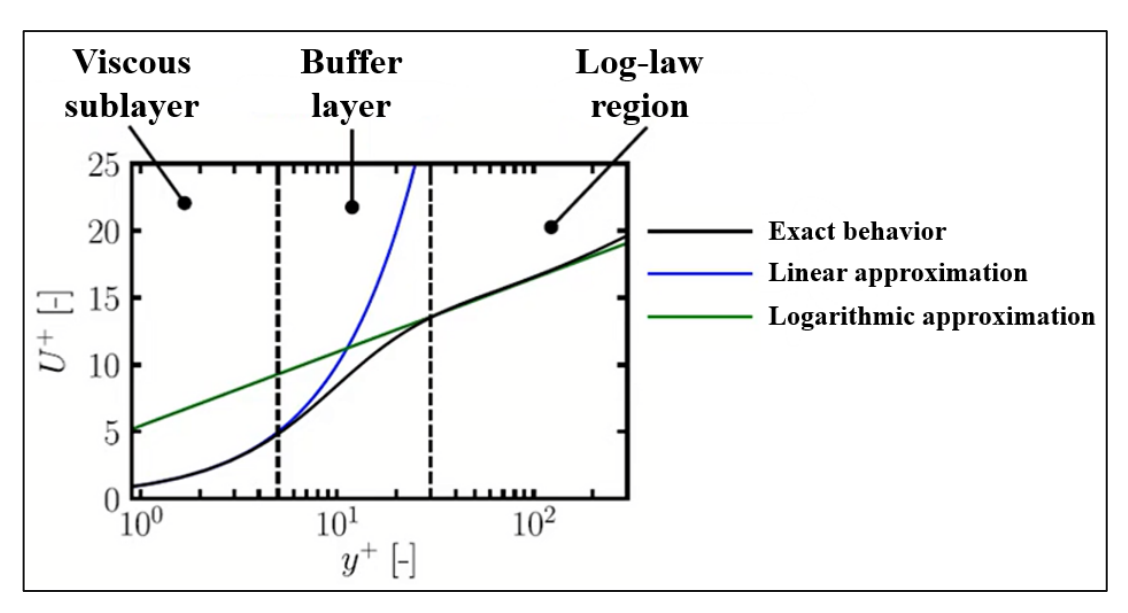


Figure 13: The law of the wall. The exact behavior of the dimensionless velocity can be approximated by a linear function in the viscous sublayer, and a logarithmic function in the log-law region. Modified after [47].

There are two approaches to incorporate the law of the wall into a CFD simulation. Firstly, there is the option to use empirically derived wall functions, which model the flow in the entire near-wall region. The center of the cell closest to the wall must be placed in the loglaw region,  $30 < y^+$ , to ensure correct functionality and accurate results [14].

Secondly, on can subdivide the near-wall region with mesh cells, thereby resolving the viscous sublayer. For this tactic, the center of the cell closest to the wall must be placed in the viscous sublayer, preferably around  $y^+ = 1$  [14]. The use of mesh inflation techniques can help optimizing the near-wall region for this approach. Mesh inflation means filling the geometry with small cells close to the wall and layer-wise progressively increasing cell sizes as the core of the geometry is approached [44]. A graphical representation of the two wall treatment methods can be seen in Figure 14.

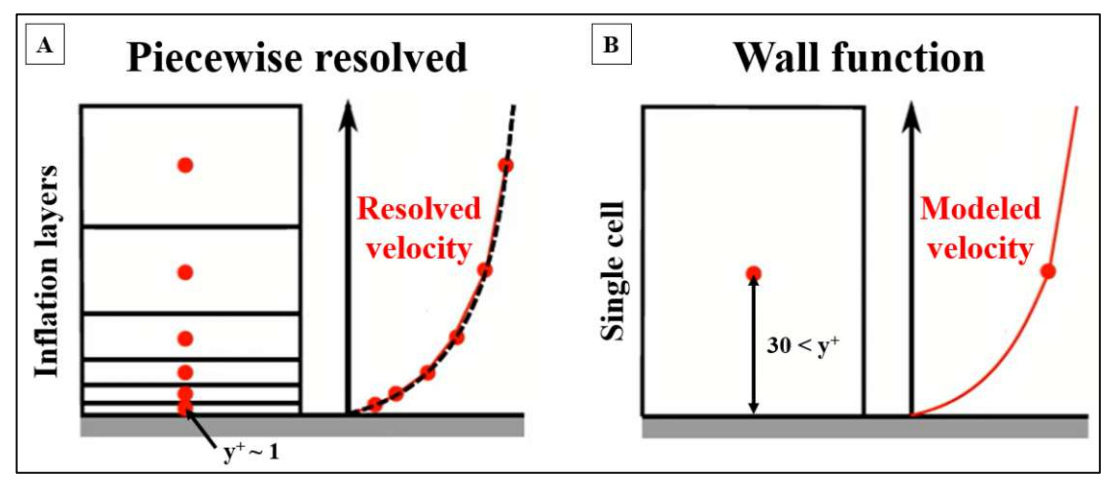


Figure 14: Schematic representation wall treatment approaches. A: Resolved through multiple inflation layers,  $y^+ \approx 1$ . B: Modeled through a wall function for a single cell,  $y^+ > 30$ . Modified after [47].



Finally, it is necessary to conduct a mesh independence study in order to estimate the numerical errors in the simulation. Ideally, at least three different, successively size-refined grids should be created and compared. The mesh independence study is then done by obtaining steady solutions on these grids and checking that, with successive refinements, the accuracy of the solution is not changing significantly. Mesh independence tests assume that the approximate solutions obtained from finite grids will converge to the exact, analytical solution as the finite quantities vanish. This is known as grid convergence. To assess the performance of coarser grids, the approximate solution on the finest grid can be used in place of the exact solution. A grid constituting a reasonable compromise between high solution accuracy and low element count, avoiding big computational expenses, should be chosen [4].

#### 2.2.6 Solver considerations for turbulent CFD simulations

So far, physical fundamentals and preprocessing aspects to set up a basic flow simulation have been discussed in detail. However, one should not assume that any accurate answer obtained from such a simulation is necessarily the correct answer [4]. By thoughtful modifications of the solver settings, both the accuracy of the computed result and the convergence rate of the simulation can be increased [17].

The most important decision is the choice of a suitable solver. The two common types of solvers used are pressure-based and density-based solver. The pressure-based approach was mainly used for low-speed incompressible flows, while the density-based approach was developed for high-speed compressible flows. Therefore, a pressure-based solver is reasonable to use for respiratory airflow simulations [21].

Pressure-based solvers take momentum and pressure as their initial variables and solve all other transport equations from there. Well accepted solver algorithms are the semi-implicit method for pressure-linked equations (SIMPLE), or the pressure-implicit method with splitting of operators (PISO) [21]. SIMPLE is a numerically robust algorithm useful for LES or steady simulations [4]. PISO has advantages in unsteady, transient flow problems or for meshes with highly skewed cells [21].

In most CFD software, solution information is only stored for the center of a cell. Hence, to calculate flow, variables of interest must be interpolated to the faces of elements [21]. A sophisticated interpolation scheme for this purpose is the second-order upwind discretization method. In this approach, second-order accuracy is achieved at the faces

through a Taylor series expansion of the cell-center solution. Convergence may be slower than with simpler discretization schemes, but it is essential to use such an advanced method with tetrahedral meshes [18]. Nevertheless, sometimes working with second-order accuracy can be computationally expensive. This is for example the case in an LES, where the cell count is typically high. For these cases, linear first-order discretization approaches, like the first-order upwind method can be used. A first-order scheme is easier to converge but less accurate than the second-order scheme [21].

Every CFD solver works by iterating a temporary solution towards a better one. So, before the first iteration, a value for every quantity must exist. Setting it is called initialization. The more realistic the value, the better and quicker the convergence will be [21].

The solver should be given sufficient iterations such that the problem is converged. At convergence, the calculated solution no longer changes significantly with subsequent iterations. Overall balance is achieved in all cells to a specified tolerance, represented by the respective residual [4]. Generally, a decrease in residuals by three orders of magnitude indicates sufficient convergence. At this stage of convergence, major flow features should be correctly established [21].

# 2.3 PIV for respiratory airflow experiments

In the following, features and working principles of PIV will be described briefly. The application of PIV and its advantages in quality and obtainability of data are set out. Also, relevant PIV experiments regarding respiratory airflow research are discussed.

# 2.3.1 Functional concept of PIV

The setup of a PIV-experiment system typically consists of multiple subsystems [5]:

- Seeding: Tracer particles are typically introduced into the flow in most applications, serving the purpose of monitoring the fluid's progression. These particles aid in tracing and observing the development of the fluid.
- Illumination: A minimum of two illuminations, often laser pulses, within a short and predetermined time interval is required to effectively visualize these particles in a plane or volume of the flow.
- Recording: The scattered light emitted by the tracer particles must be captured and

recorded by a camera, either on two distinct frames or within a sequence of frames captured.

- Calibration: To establish the correlation between the displacement of particle images in the image plane and the actual movement of tracer particles in the flow, a calibration process is necessary.
- Evaluation: The displacement of the particle images between the laser pulses must be determined through evaluation of the PIV recordings.
- Processing: Sophisticated processing techniques are essential to detect and eliminate invalid measurements, as well as to extract complex flow quantities of interest.

A typical setup for a two-dimensional (2D) PIV recording of a flow field is shown in Figure 15.

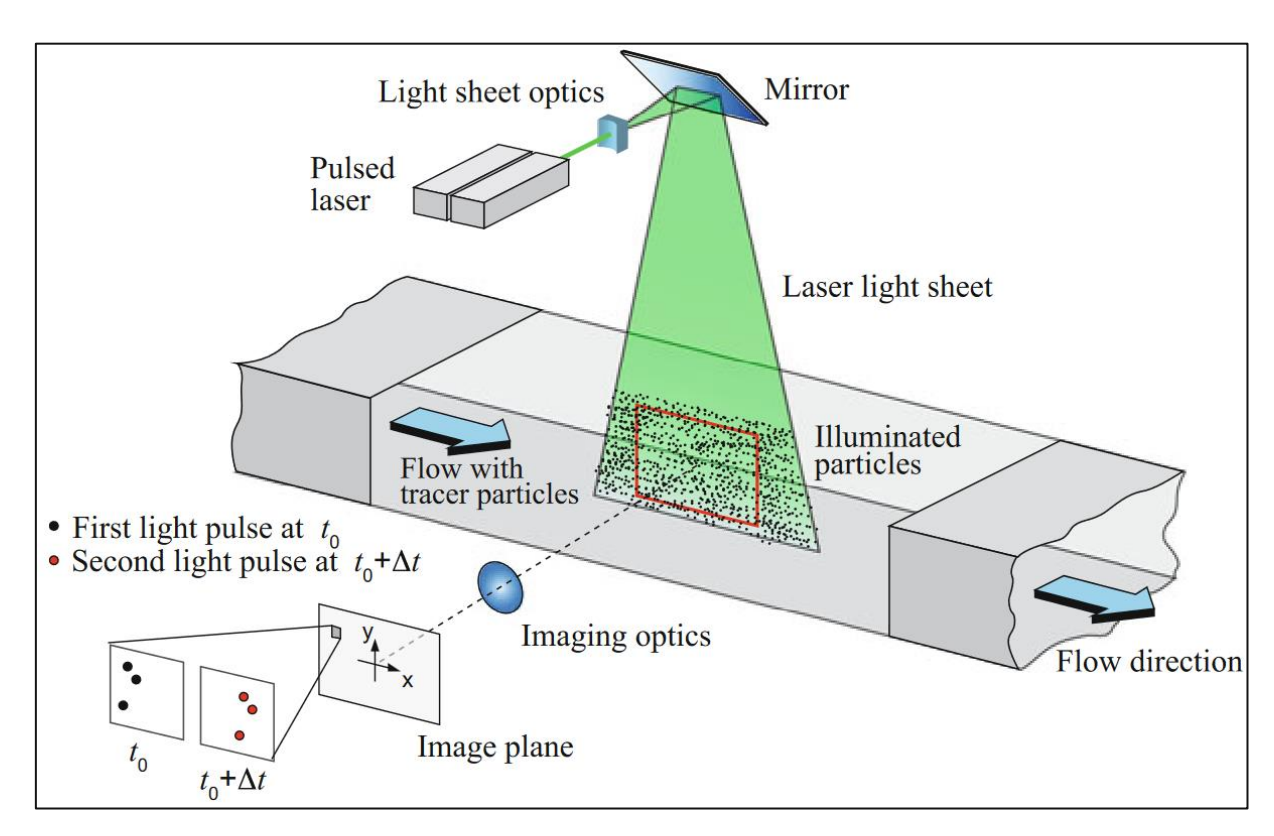


Figure 15: Illustration of a typical 2D PIV experiment setup [5].

During seeding, small tracer particles are added to the flow. The plane of interest of the flow is illuminated multiple times by a laser light sheet. The selection of the time delay  $\Delta t$ between light pulses must be done in consideration of both the expected flow velocity and the magnification during imaging. The light scattered by the tracer particles is recorded via a high-quality digital camera for all separate pulses. For every pair of light pulses and every



tracked particle, a local displacement vector  $\Delta \underline{s}$  can be calculated. This is done by means of cross-correlation, which is a statistical method [5]. From the local displacement vectors  $\Delta \underline{s}$ , taking into account the time delay  $\Delta t$  between the two laser pulses and the calibration of the imaging system, the velocity of the flow field can be computed [48]:

$$\underline{u} = \frac{\Delta \underline{s}}{\Delta t} \tag{19}$$

For evaluation, the digital PIV recording is divided in small subareas, also known as interrogation areas. Investigations using the PIV technique usually result in a large number of images for each region of interest, which must be further processed. Extracting valuable information from the raw data resulting in velocity vector maps is known as processing of PIV data [5].

#### 2.3.2 Tomographic 3D PIV

The tomographic 3D PIV technique allows the measurement domain to be a volume rather than a plane. For obtaining volumetric information from planar projections, the principles of tomography are needed. A diagram showing all steps involved in tomographic PIV is given in Figure 16 [5].

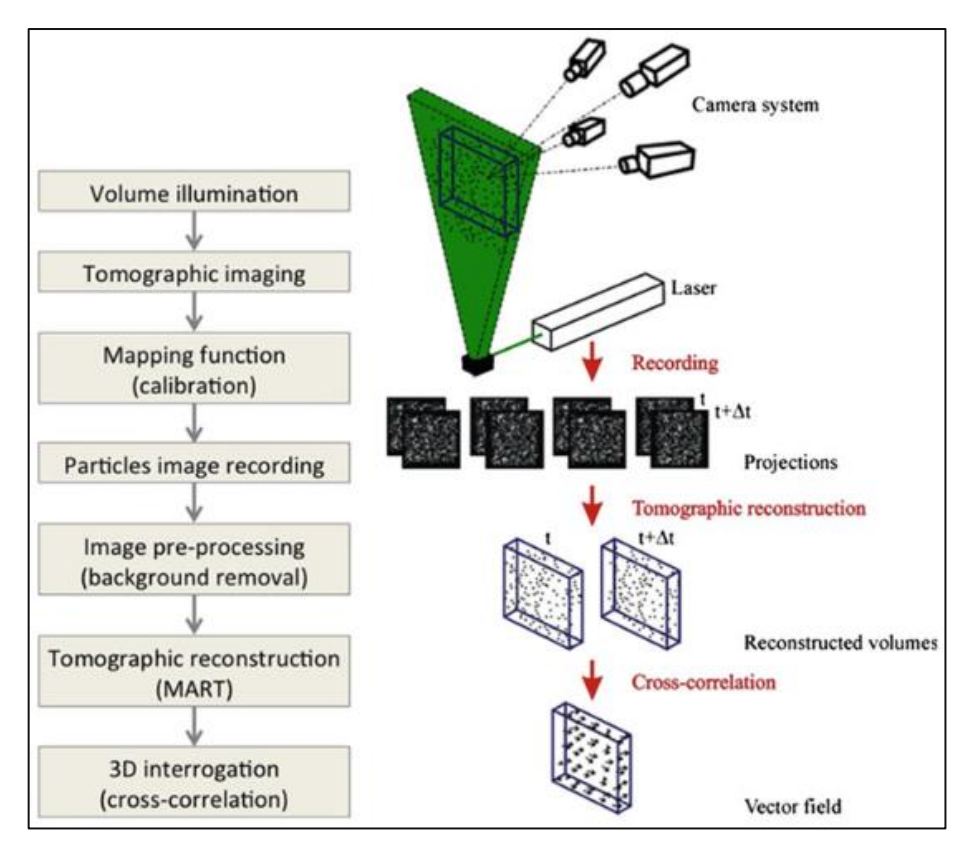


Figure 16: Flow chart and illustration of the steps involved in tomographic 3D PIV [5].



The volume is illuminated by expanding or reducing the thickness of the laser light sheet to the desired depth. Between three and six cameras are placed at an angle to observe the illuminated volume from different directions. Through a calibration procedure, it is possible to know the relation between the position of a tracer particle in 3D space and its projections onto the image planes. The set of time-synchronized images from all cameras serves as the input to a tomographic reconstruction algorithm. This is commonly done by the multiplicative algebraic reconstruction technique (MART). The generation of velocity vector fields within the volume is again performed by means of a cross-correlation algorithm [5].

#### 2.3.3 PIV for microfluid investigations

Operating principles of PIV presented so far relate to macroscopic orders of magnitude. However, in many areas of science and engineering, evaluation of flows in a macroscopic domain is not expedient. Depending on the given problem, it may be important to determine the flow field at the micrometer scale. The study of flow in these areas is usually called microfluidics. A state-of-the-art microfluid velocity measurement technique is 2D μPIV [48].

The measurement principles of  $\mu$ PIV are mostly based on PIV for large scales (Figure 17). Additionally, µPIV uses microscopy and digital imaging methods for the determination of velocity data [48]. To prevent interactions between the laser and the camera, a dichroic mirror that separates different wavelengths may be used, so that only the light reflected from the tracer particles reaches the camera, excluding the light from the laser and surroundings [49]. Depending on the choice of microscope objectives, regions of interest can range from millimeter to micrometer scale [5].

When performing µPIV experiments, fluid velocity measurements are normally done in so-called microchannels or flow chambers. The design of these microchannels is crucial to the experiment since the channel geometry influences the fluid flow. Channel layouts therefore must be carefully chosen and should match the real-world fluid domain of interest as closely as possible [5]. A syringe pump can be used to steadily drive the tracer particles through the flow chamber [49].

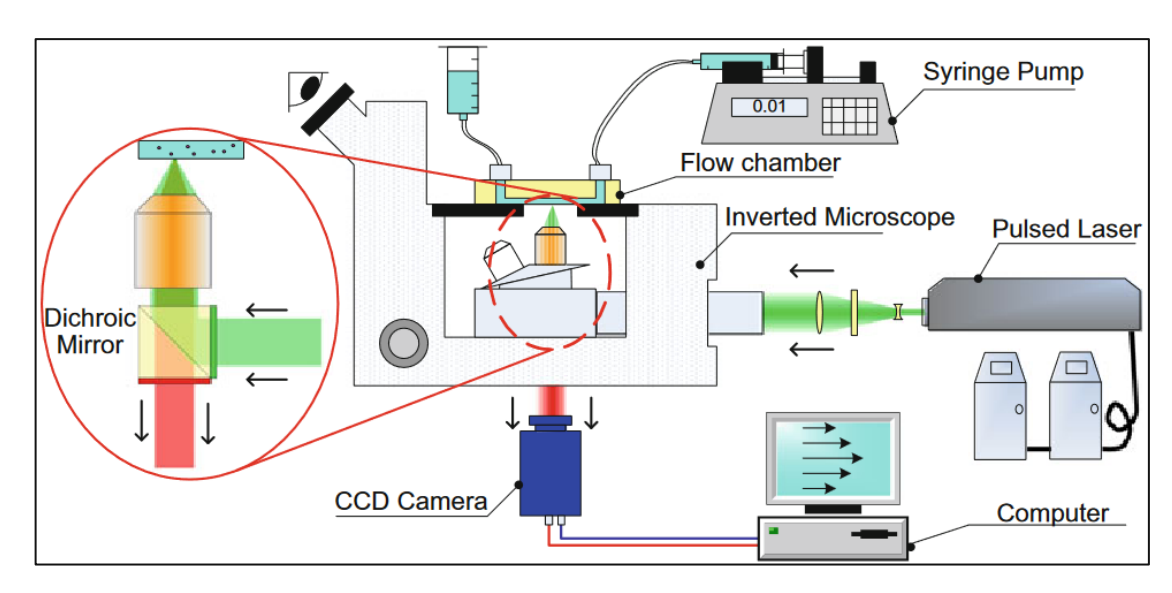


Figure 17: Illustration of a typical 2D μPIV experiment setup [5].

### 2.3.4 Use cases of PIV in respiratory research

The spatial and temporal development of a flow field in a realistic human lungs model can be investigated on several scales using PIV [50]. Generally, PIV studies can be assigned to one of three groups, depending on the examined area and its respective order of magnitude: Upper airway-, lower airway-, or alveoli research (Figure 18).

Regarding investigations of the upper airways, multiple studies using PIV [26-28, 50-54] have been conducted. Generally, in these types of experiments, macroscopic multi-plane 2D or 3D PIV measurements are performed. The examined fluid domain is either a 3D realistic human lungs replica, obtained from computed tomography data [26-28, 50, 52, 53], or an idealized 3D model [51, 53, 54]. Airway generations examined with this approach reach maximally from generation 0 (trachea) to generation 7 (middle-sized bronchioles) [50]. Usually, the walls of the fluid domain are made of transparent silicone [50, 52], glass [55], or transparent polymers suitable for additive manufacturing [26-28, 53, 54]. Depending on the chosen solid, the material-specific refractive index changes, bending the laser light sheet at the transition between wall and fluid. This effect must be considered when choosing the composition of the seeded fluid and can be counteracted through refractive index matching [49]. Mostly, a seeded mixture of water and glycerol, matching the refractive index of the wall is chosen as the fluid to be assessed [27, 50, 52]. However, air with added tracer particles can be used as well, which is common practice in experimental particle deposition studies for example [28]. Although obviously air is transported in the real human respiratory tract, the water/glycerol mixture may be used as the examined fluid in order to match the refractive index and improve visibility of the tracers.

A large part of microfluidic applications of PIV is connected with respiratory research as well. Many examples can already be found, such as the microflow of fluid in the lower airway generations [56-58] or alveoli [59-62]. Concerning lower airway µPIV investigations, generations 10 (middle-sized bronchioles) to 21 (alveolar ducts) can be assessed [56, 58]. Alveolar µPIV studies concern themselves mostly with generations 20 to 23 (alveolar ducts and sacs) [59, 61], or a single mimicked alveolus [62]. Since computed tomography data for the given size ranges is not commonly available, idealized models of lower airway bifurcations and alveoli are used. Well established carriers for the microchannels are engraved aluminium alloy plates [56, 58] or polymer plates made via additive manufacturing [59]. Again, it is reasonable to use a water/glycerol mix as the seeded fluid, but also air with added tracer particles can be used [61].

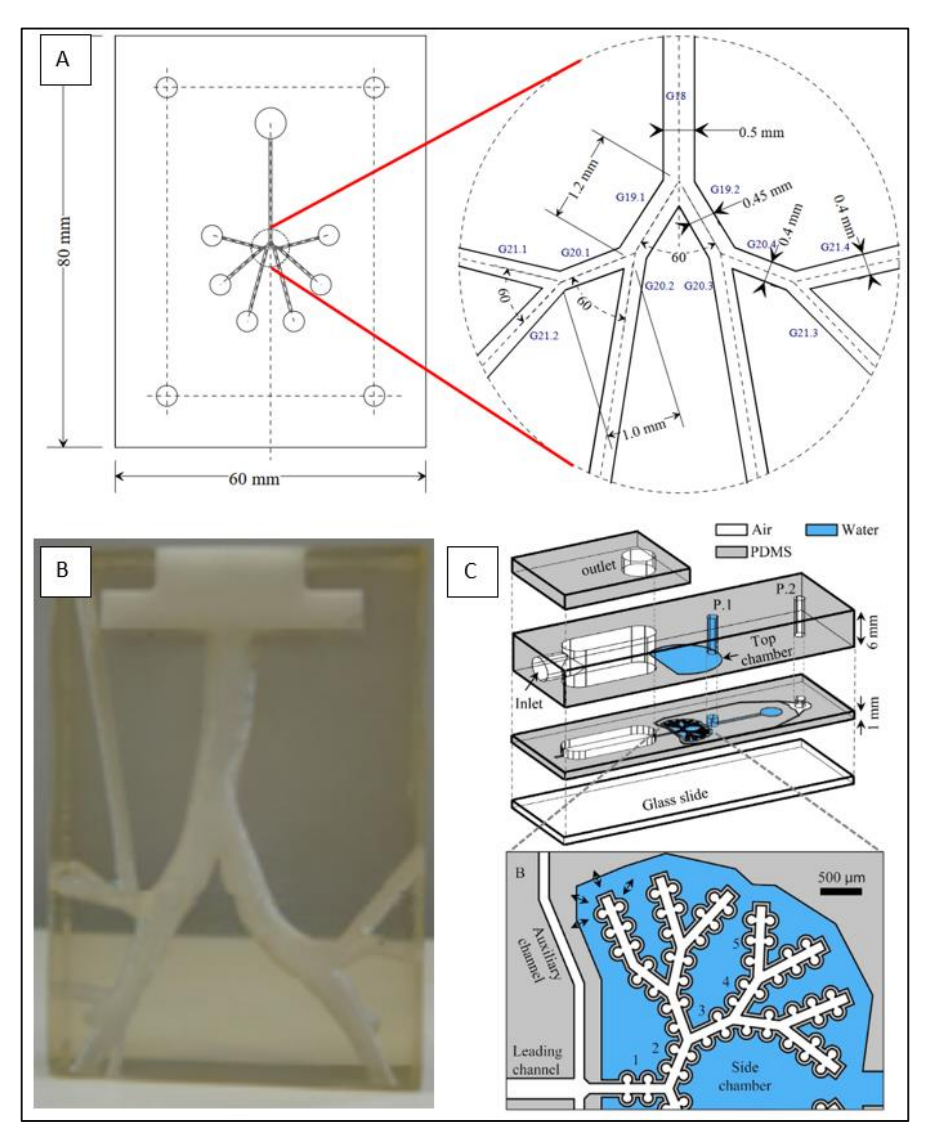


Figure 18: Different PIV-compatible channels for fluid guidance. A: Sketch of a microchannel consisting of idealized airway generations 18-21. Modified after [56]. B: Computed tomography-based silicone model representing airway generations 0-2. Modified after [52]. C: Schematics of a microchannel for researching alveoli. Modified after [61].

# 3 Methods

The methodology described and applied in this thesis is strongly oriented towards common workflows in the field of modeling and simulation. After working through the theoretical, medical-technical fundamentals specified in the introductory chapters, a suitable geometric model was created. Using this model, fluid mechanics simulations were carried out via CFD. Furthermore, experimental fluid mechanics tests were performed by means of μPIV. This was done in order to evaluate the simulation results in later steps.

# 3.1 Design: Idealized lung model for respiratory airflow studies

At the beginning of the design step, a geometry representing the fluid domain for the CFD simulations was created with the help of the CAD software SolidWorks R2022 (Dassault Systèmes SE, Vélizy-Villacoublay, France). The goal was to come up with a design that resembles the volume space of the human airways but is also simplified enough to perform reasonable CFD simulations. Because of these requirements, the choice was made to completely model the first 4 generations of the human bronchial tree (from here on designated as the upper airways), but afterwards only model a single continuing branch of the lung down to generation 22 (designated as the lower airway branch).

For many considerations of the overall behavior of the lung system, it is sufficient to disregard its irregularities and to concentrate on its regular features. The geometry of the model was therefore designed after a modified version of "Weibel's model A" [63]. In this model, uniform airway generations branch 23 times, multiplying by regular dichotomy. This means all ducts in a given generation  $\zeta$  have identical dimensions and split into two subsequent generations  $\zeta + 1$  on their distal end. The dichotomous branching angle is assumed to be 70 degrees consistently over all generations. Diameter and length of the the airway ducts are given by empirical data [63]. Detailed information on the dimensions of the created human airway model is listed in Table 3.

In foresight that different turbulence models may be necessary to describe airflow in the upper airways and the lower airway branch, they were completely separated into two distinct parts by splitting them at their transition at generation 3. However, this choice also implied that for the following CFD simulations, boundary conditions had to be set in a, considerate way to ensure the integrity of the airflow through the model. Generation 23, representing the alveolar sacs, is missing on purpose in the current lung model. This choice was made in order to set boundary conditions at the end of generation 22 and thereby ensure correct airflow behavior in the following CFD simulations.

Lung generation 7	Duct length [cm]	Proximal duct diameter [cm]	Distal duct diameter [cm]	Surface alveolated [%]	Anatomical description	Technical description
0	12.00	1.800	1.800	[/0]	Trachea	
1	4.760	1.220	0.830	-		Upper
2	1.900	0.830	0.560	1	Bronchi	airways
3	0.760	0.560	0.450	1		
4	1.270	0.450	0.350	1		
5	1.070	0.350	0.280			
6	0.900	0.280	0.230			
7	0.760	0.230	0.186			
8	0.640	0.186	0.154	0.00	Conductive	
9	0.540	0.154	0.130	]		
10	0.460	0.130	0.109	]	bronchioles	
11	0.300	0.109	0.095	]		
12	0.330	0.095	0.082			Lower
13	0.270	0.082	0.074			
14	0.230	0.074	0.066			airways
15	0.200	0.066	0.060			
16	0.165	0.060	0.062			
17	0.141	0.062	0.062	0.12	Dagnington	
18	0.116	0.062	0.062	0.25	Respiratory bronchioles	
19	0.100	0.062	0.062	0.50	biolicilioles	
20	0.083	0.039	0.039	1.00		
21	0.071	0.039	0.039	1.00	Alveolar ducts	
22	0.058	0.039	0.039	1.00		

Table 3: Dimensions, as well as anatomical and physiological equivalents of Weibel's human airway model.

One flaw of Weibel's proposed model is that, while precise information about the ducts is given, there is no note about the geometrical properties of the alveoli. Therefore, the alveoli have been modeled in agreement with other studies that describe the alveolus as a truncated octahedron [7, 64, 65]. Since the alveoli of different lung branches press against each other and form a 3D honeycomb-like structure, the truncated octahedron represents the alveolus better than a spheroid (Figure 19). Multiple truncated octahedra stacked together without gaps represent this mentioned 3D honeycomb-like structure well [7].

However, it must be mentioned that in the acinar regions of the single lung branch modeled, since it represents the fluid domain, a small space representing the walls dividing the alveoli was left between adjacent truncated octahedra. All alveoli were modeled with a uniform height of 150 micrometers and cover the surface area of the ducts specified in Table 3. A view of the created geometry is given in Figure 20. For the following CFD simulations, the created CAD geometry was saved in the STEP format.

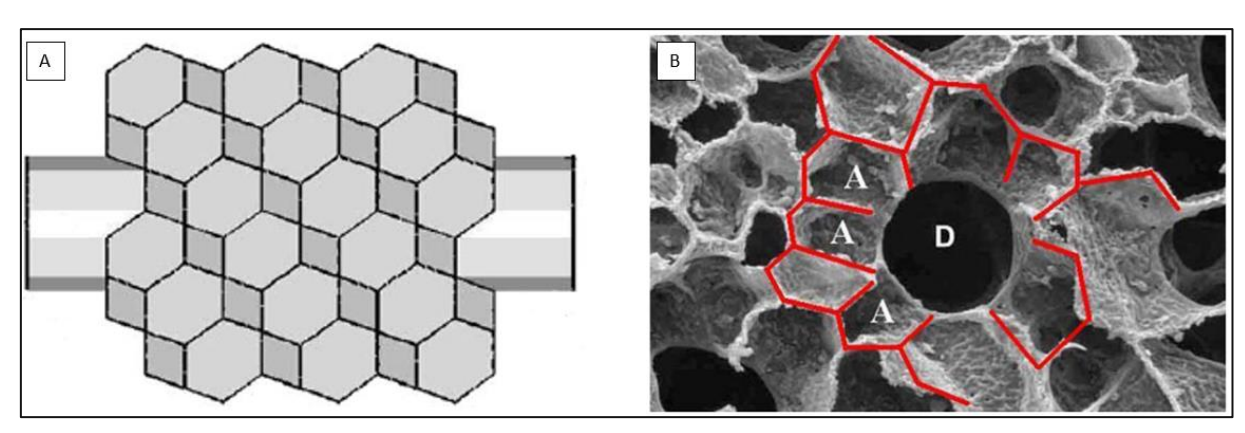


Figure 19: A: Model of a respiratory bronchiole using truncated octahedra. Modified after [65]. B: Microscopic image showing a cross-section of an alveolar duct. Alveoli (A) can be seen surrounding the duct (D). Modified

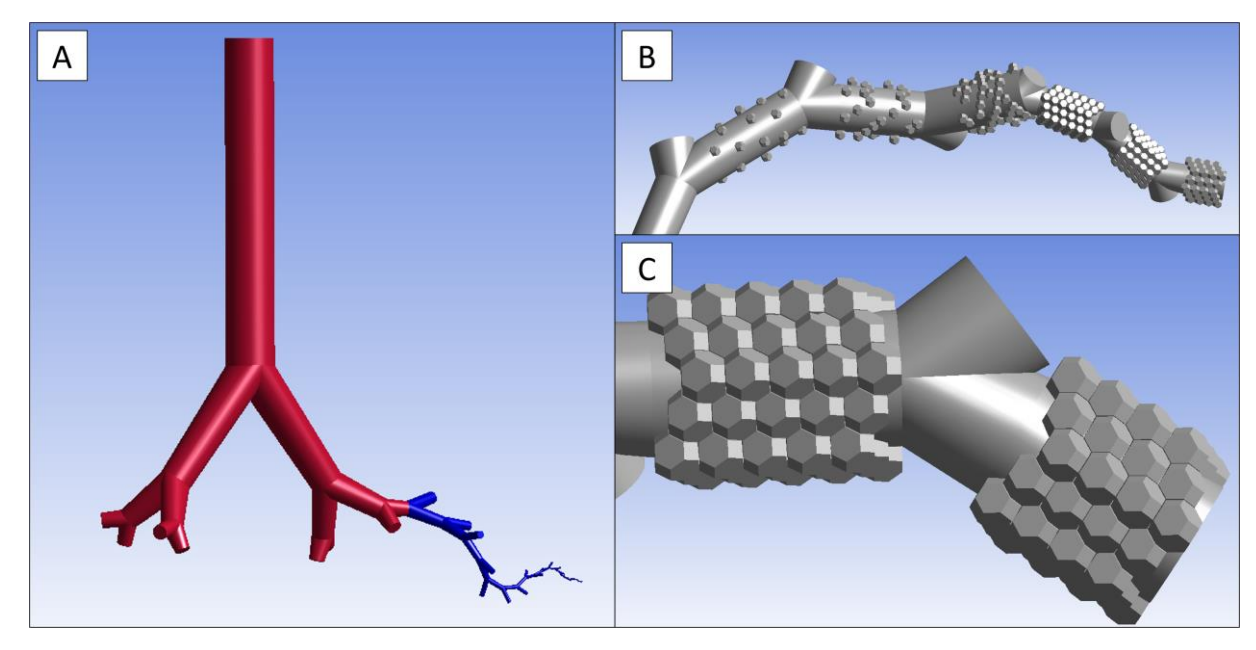


Figure 20: Overview of the created human lung geometry. A: Complete the upper airways (red) and single lung branch from the lower airways (blue). B: Generations 17 to 22 with increasingly alveolated surfaces. C: Detailed view of generation 21 and 22. Small spaces between the alveoli can be distinguished.

# 3.2 Implementation: Fluid dynamics simulations

For both upper airways and lower airway branch, a mesh independence study was done. Afterwards, laminar-, RANS-, and LES-type simulations were performed using a suitable mesh. In the following, an outline of the applied methodology is given. Furthermore, the implementation of the specific simulations conducted will be explained in greater detail.

# 3.2.1 Outline of the performed simulations

Building upon the presented literature and theoretical background regarding respiratory fluid dynamics, the following simulations were done:



- Mesh independence studies: For each the upper- and lower airway geometry, four meshes ranging from coarse to very fine were created. Their differences in a steady simulation were evaluated and a satisfactory mesh for both parts was chosen for the following simulations.
- Entirely laminar simulations: Three time-transient simulations mimicking different phases of SHFJV were set up. Throughout the entire airways, the airflow was handled to be laminar. This was the simplest case of airflow assumed.
- Combined SST  $k-\omega$  and laminar simulations: Three time-transient simulations mimicking different phases of SHFJV were set up. In the upper airways, the possibility of turbulent airflow was assumed. An SST  $k-\omega$  turbulence model was chosen to describe the flow in these generations. Going down the lower airway branch, a transition towards fully laminar flow was assumed.
- Combined LES and laminar simulations: Three time-transient simulations mimicking different phases of SHFJV were set up. In the upper airways, the possibility of turbulent airflow was assumed. An LES turbulence model was chosen to describe the flow in these generations. Going down the lower airway branch, a transition towards fully laminar flow was assumed.

Representing the three most prominent approaches in respiratory research, one laminar-, one RANS-, and one LES-model were chosen to describe the airflow in the upper airways. Since all the mentioned model types can be seen as suitable to describe airflow in the lungs, it is reasonable to compare possible differences in their results regarding the task at hand.

For running the simulations, a Lenovo ThinkPad T14 Gen1 computer (Lenovo Group Ltd, Hongkong, China) with an AMD Ryzen 7 PRO 4750U central processing unit (Advanced Micro Devices Inc, Santa Clara, USA) and 32 gigabytes of random-access memory was used. The entire workflow of all simulations was done within the Ansys 2023 R1 (Ansys Inc, Canonsburg, USA) software environment.

Firstly, a "Fluid Flow (Fluent)" workflow was set up in Ansys Workbench. Since the upper and lower lung geometry parts were already made in SolidWorks, they just had to be imported, instead of creating new ones with Ansys DesignModeler or Ansys SpaceClaim. However, these tools have been used to check if the chosen part could be imported correctly and to prepare it for meshing. Secondly, the imported geometry was meshed in Ansys Meshing. In a third step, after the mesh was generated, it was loaded into Ansys Fluent.

Ansys Fluent is a general-purpose CFD software used to model fluid flow. Finally, after the simulation results were calculated, they were postprocessed using Ansys CFD-Post.

Specifics of individual simulations will be explained in more detail in the respective subchapters. However, a few general remarks about the workflow should be mentioned before.

All time-transient CFD simulations were performed with a changing velocity input at the top of the trachea according to a velocity profile, which was already derived in a previous project and is shown in Figure 21. This profile symbolizes the ventilation velocity at the beginning of the trachea during one breathing cycle of SHFJV and corresponds to the pressure functions given in Table 1 and Figure 8, therefore being in accordance with mechanical modeling theory of the human lungs.

However, in order to save computation time, not the entire velocity profile was used for a transient simulation with every turbulence model. Rather, three distinct parts of the profile were used for separate simulations. They were designated as "Baseline" symbolizing the airflow changes due to continuous HFJV, "Inhalation" symbolizing breathing in due to LFJV overlaying HFJV, and "Exhalation" symbolizing breathing out due to the end of the LFJV cycle.

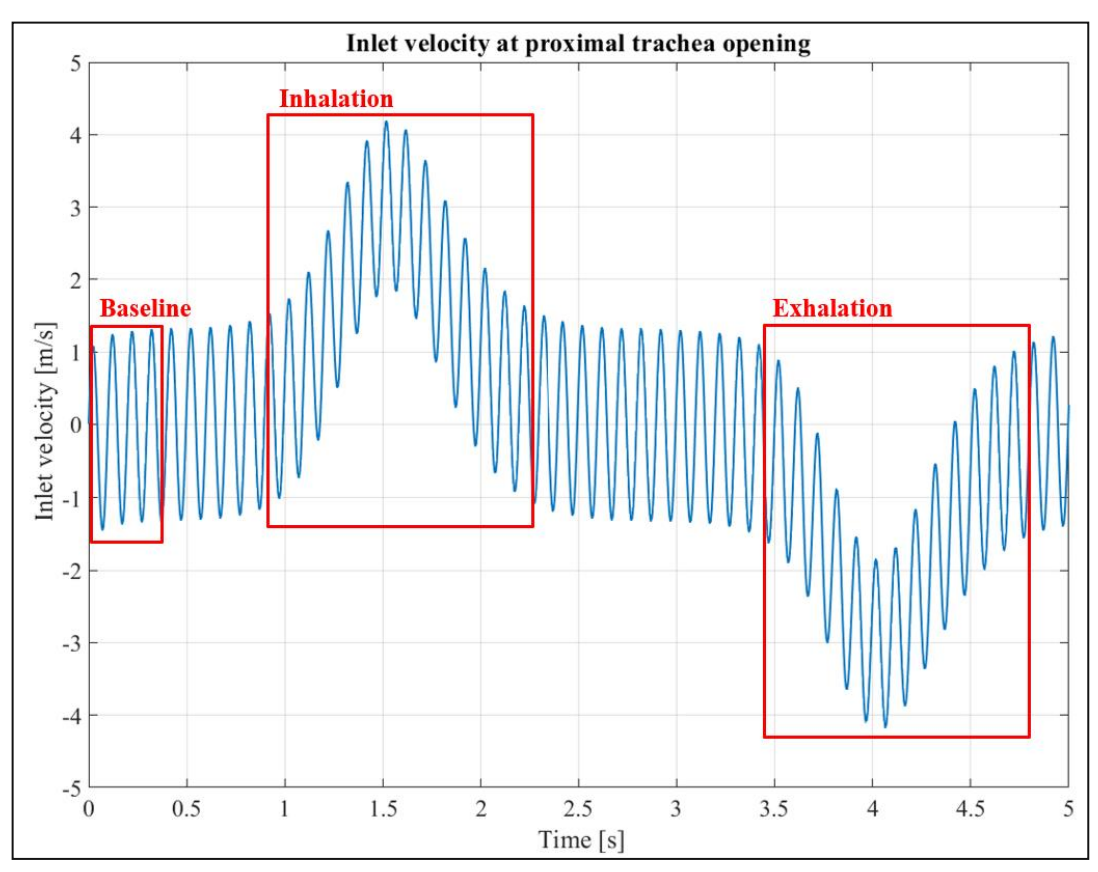


Figure 21: Velocity-time graph of the derived inlet velocity profile. The three simulated regions, "Baseline", "Inhalation", and "Exhalation" are marked with their respective red box.

At all 27 open ends of airway bifurcations, outflow boundary conditions were set. When modeling ventilation of healthy lungs, roughly half of the inhaled volume should go into the left lung and the other half into the right lung. Therefore, the flow rate weighting (FRW) at each duct of the first generation is 0.5. At the next division, the volume flowing down each bifurcation halves again, yielding a FRW of 0.25. Generally, the FRW for every outflow condition is given as:

$$FRW = \frac{1}{2^{\zeta}} \tag{20}$$

A connection between the upper and the lower airway parts was established using a tracked velocity profile, which is different from the velocity profile used as the inlet boundary condition for the upper airways. Velocity components u, v, w resulting from the flow through the upper airways were registered every timestep at the outflow where the lower airway branch is supposed to connect. These tracked components were then used as the inlet velocity for the lower airway branch simulations. Once again, the outflow boundary conditions were set using the FRW.

Regarding convergence of the solution, not only the residuals given by default were examined. Also, the area-weighted average of wall shear stress, global mass imbalance, and velocity magnitudes at selected outlets were monitored for every timestep. As absolute convergence criteria, a decrease in all relevant residuals, depending on the chosen turbulence model, below 10<sup>-3</sup> was chosen.

An exception from this rule was the continuity residual. It is a normalized residual and therefore calculated differently compared to all other residuals, which are scaled residuals [21]. Since this mattered for the performed simulations, the absolute convergence criterion for continuity was reduced. Sensitivity analyses were conducted to assess the impact of this adjustment, confirming the validity and reliability despite the decreased threshold.

In postprocessing, flow field properties were visualized through contour-, vector-, and streamline plots, using variables such as velocity, pressure, turbulence kinetic energy, or turbulence intensity. Additionally, quantitative data of the same characteristics was evaluated. In some cases, data visualization was not only achieved using Ansys CFD-Post, but also MATLAB R2023a (The MathWorks Inc, Natick, USA).



#### 3.2.2 Mesh independence studies

Two mesh independence studies were performed, one for the upper airways and one for the lower airway branch. For each of those, four different, successively size-refined grids, ranging from coarse to very fine, were created. Meshing was guided by dividing the geometry of the upper- or lower airways into multiple bodies with shared topologies. These bodies were then meshed via cell type and sizing specifications. Quality was assessed using orthogonal quality, skewness, and aspect ratio criteria as given by [21] in Table 4.

Mesh metric	undesirable	bad	adequate	good
Orthogonal quality	< 0.1	0.1 - 0.5	0.5 - 0.75	> 0.75
Skewness	> 0.9	0.9 - 0.5	0.5 - 0.25	< 0.25
Aspect ratio	> 30	30 - 10	10 - 3	< 3

Table 4: Numerical mesh quality indicators given by Ansys Meshing and their appointed meaning [21].

Appropriate type- and size-conditions for every single body were inflicted. As the trachea is geometrically represented by a perfect cylinder, it could be meshed using hexahedral cells. All other bodies constituting the upper airways were managed using tetrahedral cells.

Moreover, for the upper airways, where turbulent flow might occur,  $\mathbf{v}^+$  numbers for generated meshes were estimated before running a simulation. Average numerical values of  $y^+ \approx 1$  were striven for, with a strict condition of  $v^+$  < 5 for every wall-adjacent cell throughout the entire simulation. These criteria were implemented by means of six prismatic inflation layers.

In other words, for all four meshes used in the grid independence study of the upper airways, the thickness of the near-wall cells towards the middle of the airway duct was roughly the same. Only the length and width of the inflation layer elements, but the length, depth, and with of the volume-filling elements changed with sizing refinements.

For the lower airway branch, where the flow was always assumed to be laminar,  $y^+$  values have not been considered. Still, attention was given to a sufficiently small cell size, especially in the region of the alveoli, so that the flow could be resolved properly. Unstructured, tetrahedral elements were used to fill the lower airway branch.

Specifications of the generated meshes for upper- and lower airway mesh independence studies are given in Table 5 and Table 6, respectively. For better orientation, Figure 23 and Figure 24 show some of the created grids as well.

	Coarse (0.45×10 <sup>6</sup> elements)			Medium (1.38×10 <sup>6</sup> elements)				
Mesh metric	Min	Max	Avg	Std	Min	Max	Avg	Std
Orthogonal quality	0.18	≈ 1	0.80	0.12	0.20	≈ 1	0.81	0.12
Skewness	≈ 0	0.81	0.20	0.11	≈ 0	0.80	0.20	0.11
Aspect ratio	1.17	28.06	4.42	4.05	1.02	15.81	2.82	2.01
	Fi	Fine (3.27×10 <sup>6</sup> elements)			Very Fine (4.58×10 <sup>6</sup> elements)			
Mesh metric	Min	Max	Avg	Std	Min	Max	Avg	Std
Orthogonal quality	0.18	≈ 1	0.80	0.12	0.22	≈ 1	0.81	0.11
Skewness	≈ 0	0.82	0.20	0.11	≈ 0	0.82	0.20	0.11
Aspect ratio	1.05	14.93	2.22	1.33	1.02	14.1	2.11	1.05

Table 5: Quality indicators of the meshes generated for the mesh independence study of the upper airways.

	Coarse (0.45×10 <sup>6</sup> elements)			Medium (1.03×10 <sup>6</sup> elements)			ents)	
Mesh metric	Min	Min Max Avg Std		Min	Max	Avg	Std	
Orthogonal quality	0.05	≈ 1	0.76	0.14	0.10	≈ 1	0.78	0.12
Skewness	≈ 0	0.95	0.24	0.15	≈ 0	0.90	0.22	0.13
Aspect ratio	1.16	27.29	1.95	1.22	1.16	17.29	1.86	0.71
	Fi	Fine (3.22×10 <sup>6</sup> elements)			Very Fine (5.86×10 <sup>6</sup> elements)			
Mesh metric	Min	Max	Avg	Std	Min	Max	Avg	Std
Orthogonal quality	0.11	≈ 1	0.79	0.12	0.13	≈ 1	0.79	0.11
Skewness	≈ 0	0.89	0.21	0.12	≈ 0	0.87	0.21	0.11
Aspect ratio	1.16	12.39	1.81	0.51	1.16	12.54	1.80	0.47

Table 6: Quality indicators of the meshes generated for the mesh independence study of the lower airway branch.

With the described meshes, simulations under identical boundary conditions within each mesh independence study were performed. Simulation conditions are summarized in Table 7. While for the upper airway mesh independence study, an SST  $k-\omega$  model was employed, the lower airway mesh independence study was performed assuming laminar flow. Inlet velocities were taken to be 4 meters per second for the upper airways and 6 meters per second for the lower airway branch. Outflow boundary conditions at open airway ducts were inflicted using the specified FRW for their respective generation. Air with properties predefined by Ansys Fluent was chosen as the fluid of interest. The solver was set to use the SIMPLE algorithm with a second-order upwind discretization method. As no transient time advancement was needed for the mesh independence simulations, steady-state solutions were calculated.

To assess grid convergence, different flow properties were monitored. Since wall shear stress influences pressure drop, which is a crucial variable for pressure-based solvers, the areaweighted average of wall shear stress over the entire domain was compared. Furthermore, the average area-weighted velocity magnitude at multiple virtual sections through the domain was captured as well (Figure 22). This procedure was the same for both mesh independence studies. To ensure the correct level of  $y^+$  in the turbulent regions, average and maximum  $y^+$  values were captured for the upper airways as well.

	$\zeta = 0$ to $\zeta = 3$	$\zeta = 4$ to $\zeta = 22$		
	Coarse: 0.45 Medium: 1.38	Coarse: 0.45 Medium: 1.03		
Mesh elements [×10 <sup>6</sup> ]	Fine: 3.27 Very Fine: 4.58	Fine: 3.22 Very Fine: 5.86		
Mesh design	Interior: Hexahedral/tetrahedral grid Boundary: 6-layered prism grid	Tetrahedral grid		
Turbulence model	SST k-ω	Laminar		
Inflow boundary	1 velocity inlet: 4 m/s	1 velocity inlet: 6 m/s		
Outflow boundaries	8 outflows: Flow rate weighting	20 outflows: Flow rate weighting		
Wall treatment	No slip velocity condition			
Fluid	Air ( $\rho = 1.225 \text{ kg/m}^3$ , $\mu = 1.7894 \times 10^{-5}$	kg/m×s)		
Algorithm	SIMPLE			
Discretization scheme	Second-order upwind			
Time advancement	None (steady)			

Table 7: Settings and boundary conditions for the mesh independence studies.



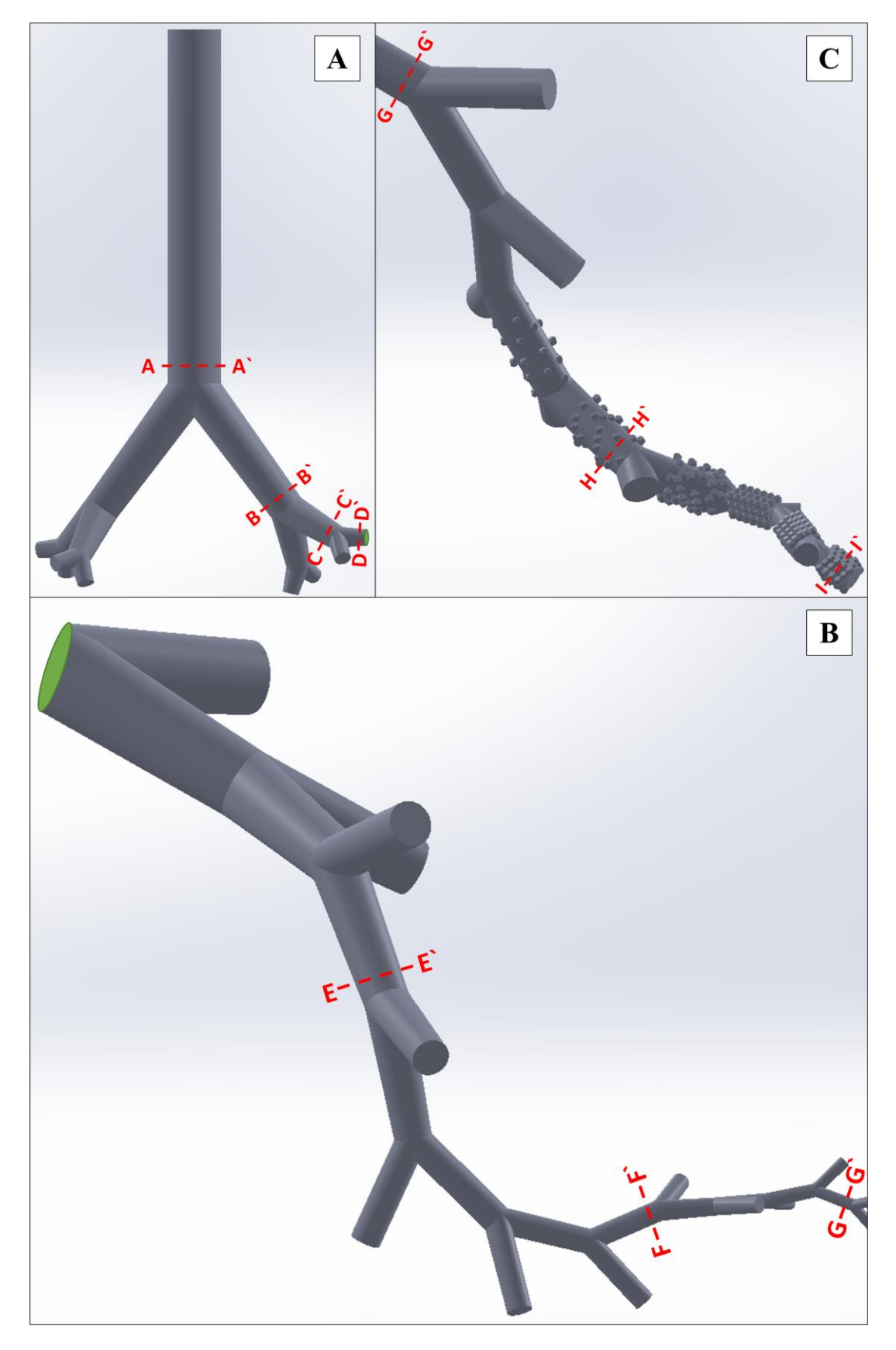


Figure 22: Virtual sections of the airway to compute the average area-weighted velocity magnitude. A: Sections A-A' to D-D' of the upper airways. The green outflow boundary marks where the lung parts are theoretically connected. B: Sections E-E' to G-G' of the lower airway branch. The green inlet boundary marks where the lung parts are theoretically connected. C: Sections G-G' to I-I' of the lower airway branch. G-G' is given again for better orientation.

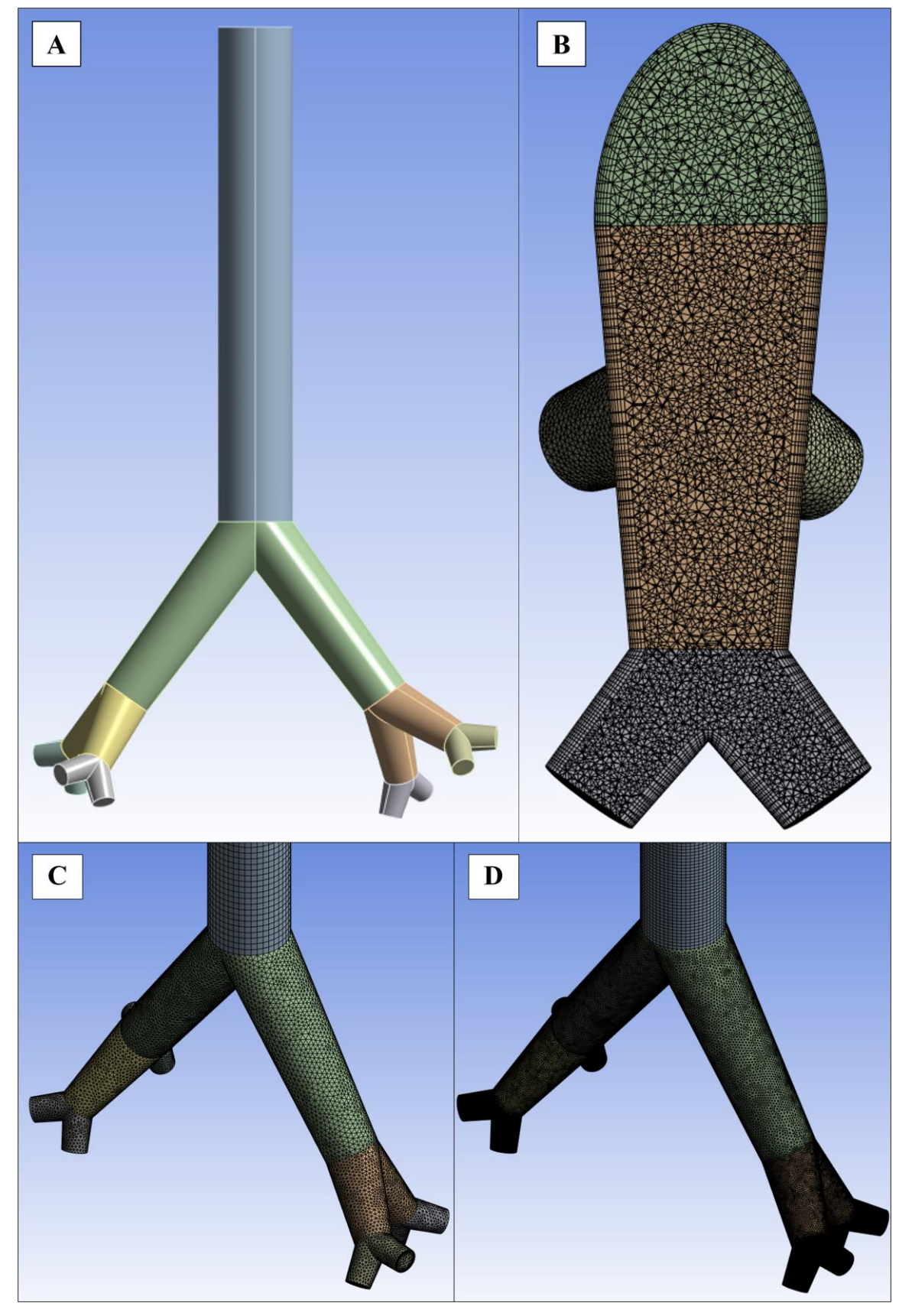


Figure 23: Meshing of the upper airways. A: Upper airways cut into separate bodies with shared topologies, marked by color. B: Section cut through generations 1 to 3 of the medium-sized mesh. Prismatic inflation layers near the walls and volume-filling tetrahedral elements can be distinguished. C: Overview of the coarse mesh. Hexagonal elements filling generation 0 can be seen. D: Overview of the very fine mesh. For lower generations, single elements cannot be distinguished in this figure.

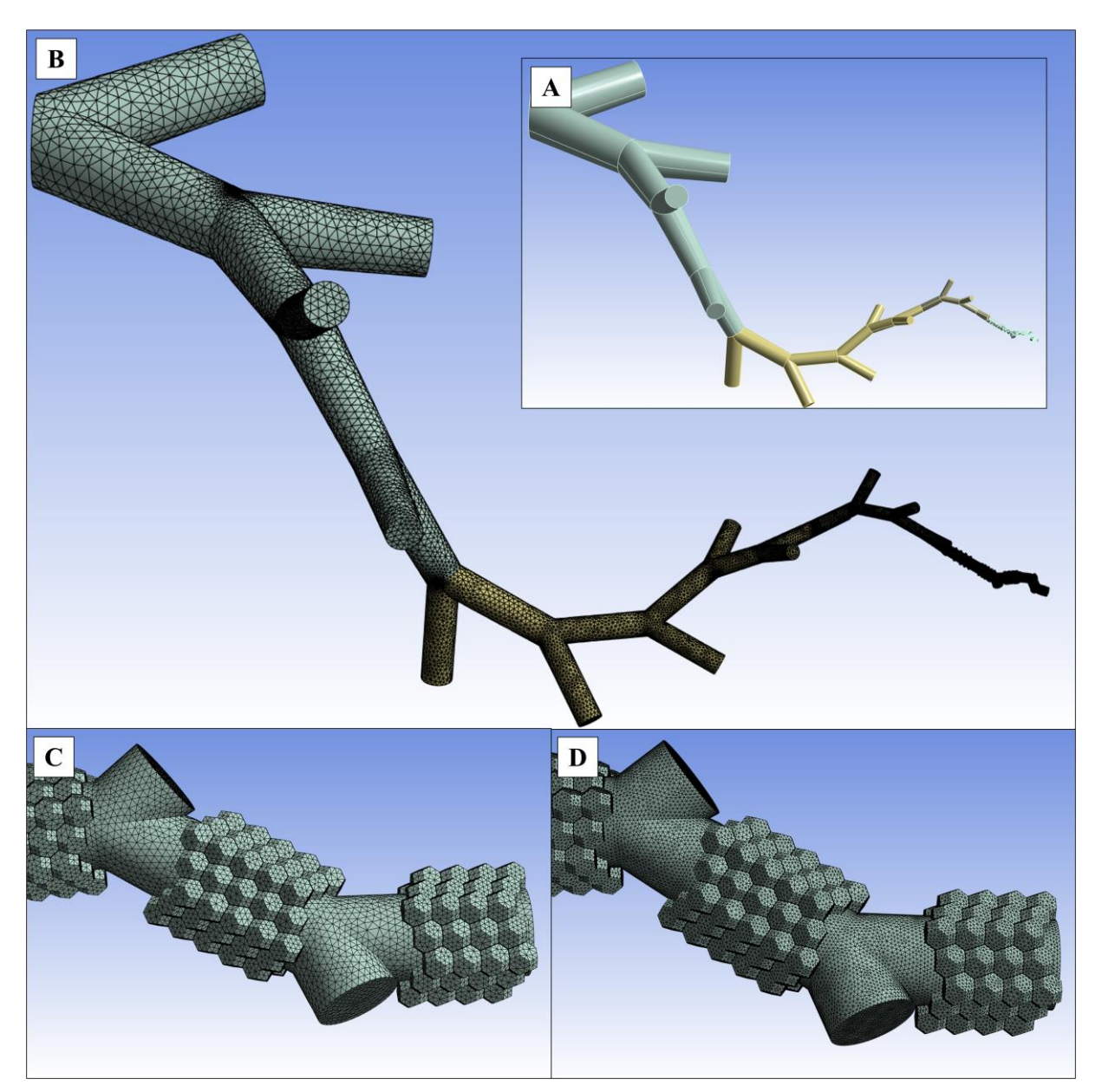


Figure 24: Meshing of the lower airway branch. A: Lower airway branch cut into separate bodies with shared topologies, marked by color. B: Overview of the medium mesh. For lower generations, single elements cannot be distinguished in this figure. C: Detailed view of alveoli of the coarse mesh. D: Detailed view of alveoli of the very fine mesh.

## 3.2.3 Entirely laminar simulations

Three laminar, time-transient simulations as initially described were run with the coarse mesh. At this point it should be mentioned that for the entirely laminar simulation, the complete upper and lower lung geometry could have been used as a single connected part, since the turbulence model does not change anywhere. However, in order to keep the workflow for all simulation types consistent and the results comparable, the geometry was still treated equally to the trials with changing turbulence models.

Furthermore, the inflation layers present in the used mesh for the upper airways are not



necessarily needed for laminar simulations. Nevertheless, it is also not a mistake to implement them since element quality is still appropriate and less meshes need to be generated and tested.

Simulation conditions are summarized in Table 8. The coarse upper airways mesh, and the medium-refined lower airway branch mesh were used. Boundary conditions were applied as specified in the outline. Air with predefined properties provided by Ansys Fluent was taken as the simulated fluid. The PISO solving algorithm with second-order upwind discretization was applied. Timestep size for the transient simulations was chosen to satisfy the CFL condition. For this purpose, an average Courant number of c < 5 throughout the entire simulation was set as the criterion to be met.

Overall computation time for the entirely laminar "Baseline", "Inhalation", and "Exhalation" simulations amounted to approximately 330 hours, corresponding to almost 14 days.

	$\zeta = 0$ to $\zeta = 3$	$\zeta = 4$ to $\zeta = 22$		
Mesh elements [×10 <sup>6</sup> ]	0.45	1.03		
Mesh design	Interior: Hexahedral/tetrahedral grid Boundary: 6-layered prism grid	Tetrahedral grid		
Turbulence model	Laminar	Laminar		
Inflow boundary	1 inlet: Given velocity profile	1 inlet: Tracked velocity profile		
Outflow boundaries	8 outflows: Flow rate weighting	20 outflows: Flow rate weighting		
Wall treatment	No slip velocity condition			
Fluid	Air ( $\rho = 1.225 \text{ kg/m}^3$ , $\mu = 1.7894 \times 10^{-5}$	kg/m×s)		
Algorithm	PISO			
Discretization scheme	Second-order upwind			
Time advancement	Baseline: 4000 timesteps at 0.0001 s step size $\triangleq$ 0.4 s Inhalation: 14000 timesteps at 0.0001 s step size $\triangleq$ 1.4 s Exhalation: 14000 timesteps at 0.0001 s step size $\triangleq$ 1.4 s			

Table 8: Settings and boundary conditions for the entirely laminar simulations.

#### 3.2.4 Combined SST $k-\omega$ and laminar simulations

Constituting the next highest level of complexity, combined SST  $k-\omega$  and laminar simulations were done. Again, the "Baseline", "Inhalation", and "Exhalation" simulations were conducted.

Simulation conditions are given in Table 9. Except for the turbulence model of the upper airways, chosen settings are equal to the entirely laminar simulations. This also included the CFL condition. Computation of the combined SST  $k-\omega$  and laminar simulations altogether took around 400 hours, or 17 days.

	$\zeta = 0$ to $\zeta = 3$	$\zeta = 4$ to $\zeta = 22$		
Mesh elements [×10 <sup>6</sup> ]	0.45	1.03		
Mesh design	Interior: Hexahedral/tetrahedral grid Boundary: 6-layered prism grid	Tetrahedral grid		
Turbulence model	SST <b>k-ω</b>	Laminar		
Inflow boundary	1 inlet: Given velocity profile	1 inlet: Tracked velocity profile		
Outflow boundaries	8 outflows: Flow rate weighting	20 outflows: Flow rate weighting		
Wall treatment	No slip velocity condition			
Fluid	Air ( $\rho = 1.225 \text{ kg/m}^3$ , $\mu = 1.7894 \times 10^{-5} \text{ kg/m} \times \text{s}$ )			
Algorithm	PISO			
Discretization scheme	Second-order upwind			
Transient time advancement	Baseline: 4000 timesteps at $0.0001$ s step size $\triangleq 0.4$ s Inhalation: 14000 timesteps at $0.0001$ s step size $\triangleq 1.4$ s Exhalation: 14000 timesteps at $0.0001$ s step size $\triangleq 1.4$ s			

Table 9: Settings and boundary conditions for the combined SST  $k-\omega$  and laminar simulations.

#### 3.2.5 Combined LES and laminar simulations

Eventually, combined LES and laminar simulations were set up. This setup represented the highest level of simulation complexity included in the methodology of this thesis. Once more, the three specified time frames "Baseline", "Inhalation", and "Exhalation" were examined.

Table 10 shows a synopsis of the simulation conditions. This time, for the upper airways, where an LES turbulence model was applied, a finer mesh was chosen. The reasoning behind this decision is that, as described in the theoretical fundamentals, LES directly resolves eddies larger than the grid resolution. So, in order to directly resolve a clear majority of the turbulence kinetic energy, a finer mesh was chosen. The turbulence model applied to the subgrid-scales was decided to be the WALE model.

While boundary conditions, fluid properties, and transient time advancement were left unchanged compared to the other turbulence models, modifications have been made in the solving algorithm and interpolation method for the large eddy simulations. Here, a SIMPLE algorithm with bounded central differencing discretization was used in order to save expenses in calculation.

Computation time for the combined LES and laminar "Baseline", "Inhalation", and "Exhalation" simulations added up to 370 hours, corresponding to circa 16 days. Controversially, the LES could be performed faster than the SST  $k-\omega$  simulations.

	$\zeta = 0$ to $\zeta = 3$	$\zeta = 4$ to $\zeta = 22$			
Mesh elements [×10 <sup>6</sup> ]	1.38	1.03			
Turbulence model	LES with WALE	Laminar			
Mesh design	Interior: Hexagonal/tetrahedral grid Boundary: 6-layered prism grid	Tetrahedral grid			
Inflow boundary	1 inlet: Given velocity profile	1 inlet: Tracked velocity profile			
Outflow boundaries	8 outflows: Flow rate weighting	20 outflows: Flow rate weighting			
Wall treatment	No slip velocity condition				
Fluid	Air ( $\rho = 1.225 \text{ kg/m}^3$ , $\mu = 1.7894 \times 10^{-5} \text{ kg/m} \times \text{s}$ )				
Algorithm	SIMPLE	PISO			
Discretization scheme	Bounded central differencing	Second-order upwind			
	Baseline: 4000 timesteps at 0.0001 s step size				
Transient time advancement	Inhalation: 14000 timesteps at 0.0001 s step size				
	Exhalation: 14000 timesteps at 0.0001 s step size				

Table 10: Settings and boundary conditions for the combined SST  $k-\omega$  and laminar simulations.

### 3.3 Evaluation: Fluid dynamics experiments

Fluid dynamics experiments are indispensable for the evaluation of reliability and accuracy of CFD simulations. Experiments such as 3D PIV or µPIV measurements provide a benchmark against which a simulated result can be compared.

While both the 3D PIV and µPIV approaches towards experimental determination of respiratory airflow may be equally reasonable, the choice was made to only conduct µPIV experiments in the scope of this project. The decision not to employ 3D PIV in the thesis at hand was primarily driven by the limited extent of a typical diploma thesis research project. While 3D PIV is a powerful experimental technique, its implementation often demands extensive resources, time, and expertise. Considering this, the inclusion of 3D PIV would have significantly expanded the complexity of experiments and data analysis. Hence, only the μPIV approach has been made use of. The downside of solely using μPIV was, however, that only smaller airway bifurcations and alveoli could be assessed, where the airflow was already assumed to be laminar in every model.

In the succeeding subchapters, a general documentation of the experimental setup used for the µPIV measurements is given. Moreover, a summary of the designing and manufacturing processes for the produced microchannels is laid out. Also, the specific methodology applied for the lower airway and alveolar μPIV experiments is presented.

#### 3.3.1 Outline of the experimental µPIV setup

Before giving the specifics of the performed measurements for the thesis at hand, it is reasonable to give a general outline of the experimental setup used for µPIV at the TU BioFluids Lab. All experiments are carried out in a similar manner as already described in [49, 66]. A visual overview of the entire experimental µPIV setup is additionally provided in Figure 25.

The system used for the µPIV measurements uses a Bernoulli 200-15 Nd:YAG laser (Litron Lasers Ltd, Rugby, England), emitting light with a wavelength of 532 nanometers combined with an Olympus IX73 inverted microscope (Olympus K.K., Tokyo, Japan) and a Zyla 5.5 sCMOS USB 3.0 high-speed camera (Oxford Instruments Ltd, Tubney Woods, England). The camera is connected to the microscope via a SPOT 2.0X DE20TMT camera to microscope adapter (Diagnostic Instruments Inc, Sterling Heights, USA). This entire setup is further connected to a LaserPulse 610036 synchronizer (TSI Inc, Shoreview, USA), which synchronizes the camera shots and laser pulses. The output pictures of the camera are then sent to a conventional computer.

For each trial, a microchannel is mounted on the stage of the microscope. More details on the designing and manufacturing of the microchannels used in this work are presented in the following subchapter.

A Model LA110 syringe pump (Landgraf Laborsysteme GmbH, Langenhagen, Germany) is connected to the assessed channel. The syringe pump is used to ensure that a specified, continuous volume flow rate is applied throughout the entire trial of every measurement.

Examined microchannels are illuminated by laser light coming from below the microscope stage. The laser light is focused through either a 10-fold magnification lens with a numerical aperture of 0.3 or a 4-fold magnification lens with a numerical aperture of 0.13. The laser beam is pointed towards the microscope stage using a dichroic mirror. This special mirror reflects wavelengths up to 602 nanometers but lets all wavelengths above pass through. Therefore, with the camera placed behind the mirror, only light emitted from excited fluorescent tracer particles, emitting wavelengths higher than 602 nanometers, is captured.

Different types of fluorescent tracer particles can be used for fluid seeding. They can vary in size, excitation peak wavelength, or emitted light wavelength. Used particles for seeding at TU Wien Biofluids Lab are generally 2 micrometers, 3.2 micrometers, or 5 micrometers

in diameter and are applied in a solution of 95 percent distilled water and 5 percent tracer particles.

The computational controlling of the entire µPIV setup is managed using 4G Insight software (TSI Inc, Shoreview, USA). This software handles acquisition, processing, analysis, and also displaying of images. Regarding the image evaluation workflow, a procedure consisting of image preprocessing, processing, and under certain circumstances postprocessing needs to be done for every measurement [67].

After images are captured and saved, they can be digitally preprocessed. Image preprocessing improves the raw image quality. In the processing step, a region of interest in the image is defined and covered with a processing mask, in which the vector flow field is calculated by means of cross-correlation algorithms. Some applications also involve postprocessing steps like vector validation tests. The acquired vector fields are then further analyzed and interpreted using the software Tecplot 360 (Tecplot Inc, Bellevue, USA) as visualization software [67].

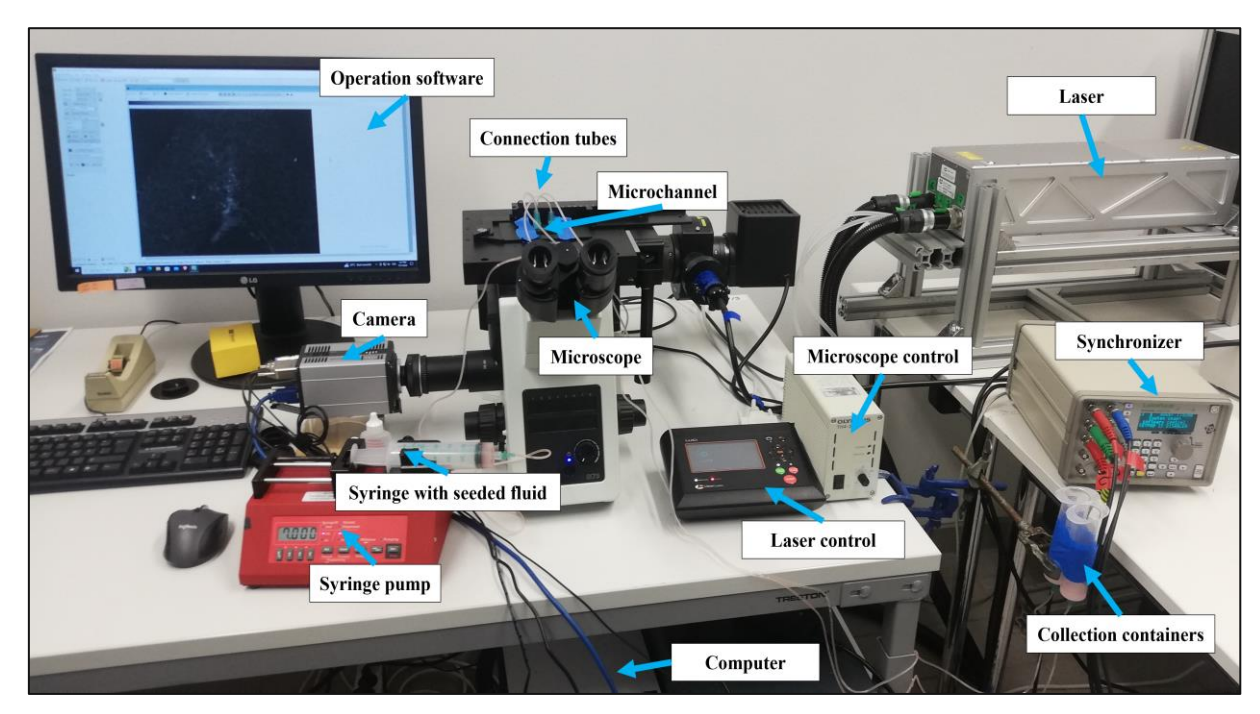


Figure 25: Overview of a typical μPIV setup as used in the TU Wien BioFluids Lab.

# 3.3.2 Design and manufacturing of the microchannels

The design and production of appropriate microchannels plays a crucial role in achieving accurate and reliable measurements in µPIV experiments. While for almost all µPIV measurements the workflow described in the outline stays similar, the microchannel must

be individually created to suit and solve the given problem. Therefore, the channel can be viewed as the heart of the μPIV setup and should be thoroughly described.

As already done for the geometry of the idealized lung model, the geometry of the microchannels was created in the CAD software SolidWorks R2022. The idea behind the channel design was to take selected bifurcations from the idealized lung model, copy their dimensions and properties as given in Table 3, cut them along their longitudinal direction and shape the channels accordingly. The cut in longitudinal direction was applied so that when measuring flow properties near the surface of the microchannel, a flow similar to the one in the midplane of a lung duct is captured. By this procedure, two channels representing the dichotomous branching at the transition from generation 10 to 11 and generation 15 to 16 were designed (Figure 26). These branching generations have been chosen to cover a range of different ducts and bifurcation dimensions.

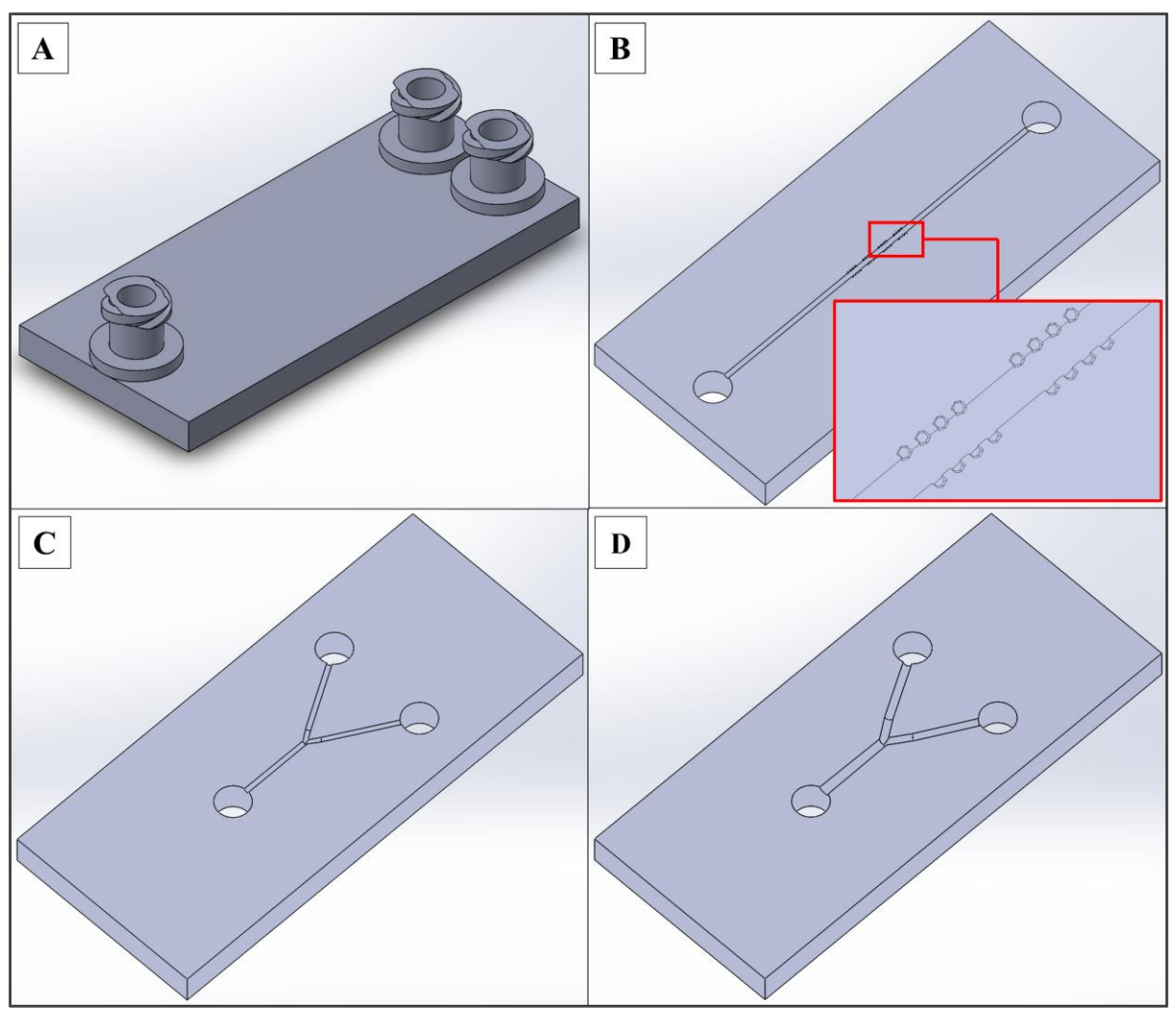


Figure 26: CAD design of the microchannels. A: Top of a microchannel with applied luer locks. B: Bottom of the alveolated microchannel. C: Bottom of the microchannel bifurcating from generation 15 to 16. D: Bottom of the microchannel bifurcating from generation 10 to 11.

Moreover, a third channel representing an alveolated duct of generation 17 was designed (Figure 26). The alveoli for this channel were once again modeled using truncated octahedra, although for the microchannels, the alveoli diameter was increased from 150 micrometers to 250 micrometers. This change to the alveolar geometry was made to avoid 3D printing resolution issues in the following manufacturing steps. The longitudinal cut method was applied for the alveolated channel as well.

What must be considered is that the syringe pump and the fluid collection containers of the μPIV setup are supposed to connect to the examined microchannel using connection tubes. The ports of these tubes are so-called luer locks. The luer lock system is a standardized screw connection used for making leak-free connections on medical and laboratory instruments. So, a luer lock part was designed and applied to the channels in SolidWorks as well, with the intent to glue the luer locks onto the in- and outlets of the µPIV channel in production (Figure 26).

The next step after the design of the channels was finalized was working out a reasonable manufacturing technique to precisely produce the microchannels. This was accomplished by following the methodology described in [49] for large parts. Hence, the decision was made to use additive manufacturing for the production of the channels, and all CAD designs were exported in STL format.

All channels were printed using an ELEGOO Mars 2 Pro 3D printer (ELEGOO Inc, Shenzen, China), which is a special 3D printer type capable of stereolithographic (SLA) printing (Figure 27). SLA 3D printing is a common photopolymerization 3D printing process known to produce high-accuracy parts. Using a light source, such as a laser or projector, liquid resin is layer-wise hardened into a solid polymer. Once the printing is completed, parts require postprocessing by washing them in an isopropyl bath. This is done to remove uncured resin remains. Additionally, some materials require postcuring with ultraviolet light to reach better strength and stability [68].

The resin used for the SLA prints was ELEGOO ABS-like clear resin (ELEGOO Inc, Shenzen, China). All plates and the luer locks were printed separately. In order to get straight plates that are only minimally warped, the tops of the microchannels were printed directly against the build platform of the SLA 3D printer. This also implied that only a minimal amount of support geometries was necessary.



Figure 27: ELEGOO Mars 2 Pro printer and Mercury Plus washing and curing station. Modified after [69, 70].

After the parts were printed, they were postprocessed using an ELEGOO Mercury Plus curing and washing station (ELEGOO Inc, Shenzen, China), also seen in Figure 27. Firstly, the printed parts were washed in isopropyl bath for 5 minutes. Secondly, they were left to dry in air so that the entire isopropyl could evaporate without any disturbance. In a third step, the channels and luer locks were cured with ultraviolet light for 7 minutes.

Resulting from the printing process, separate clear parts for all luer locks and microchannel plates were created. A luer lock was glued onto the top of every in- and outlet of the microchannels using ergo 5011 cyanoacrylate adhesive (Kisling AG, Weitzikon, Switzerland).

Finally, the bottom of the microchannel needed to be sealed. This was done with two distinct approaches. On the one hand, a 24 by 60 millimeter cover glass slip (Carl Roth GmbH, Karlsruhe, Germany), normally used for conventional microscopy, was glued on the bottom of each plate with the same cyanoacrylate adhesive already used for gluing on the luer locks.

On the other hand, the same type of cover slip was fixated by coating the bottom of each plate with another layer of resin, applying the cover slip, and curing it again with the cover slip in place. For both approaches tried out, this step required high attention and careful working, since applying the cover slip without clogging the microchannels with glue or resin proved to be very challenging. While both approaches could theoretically be used to seal the bottom of the microchannels, the resin method proved to be more reliable and precise. The manufactured microchannels can be seen in Figure 28.

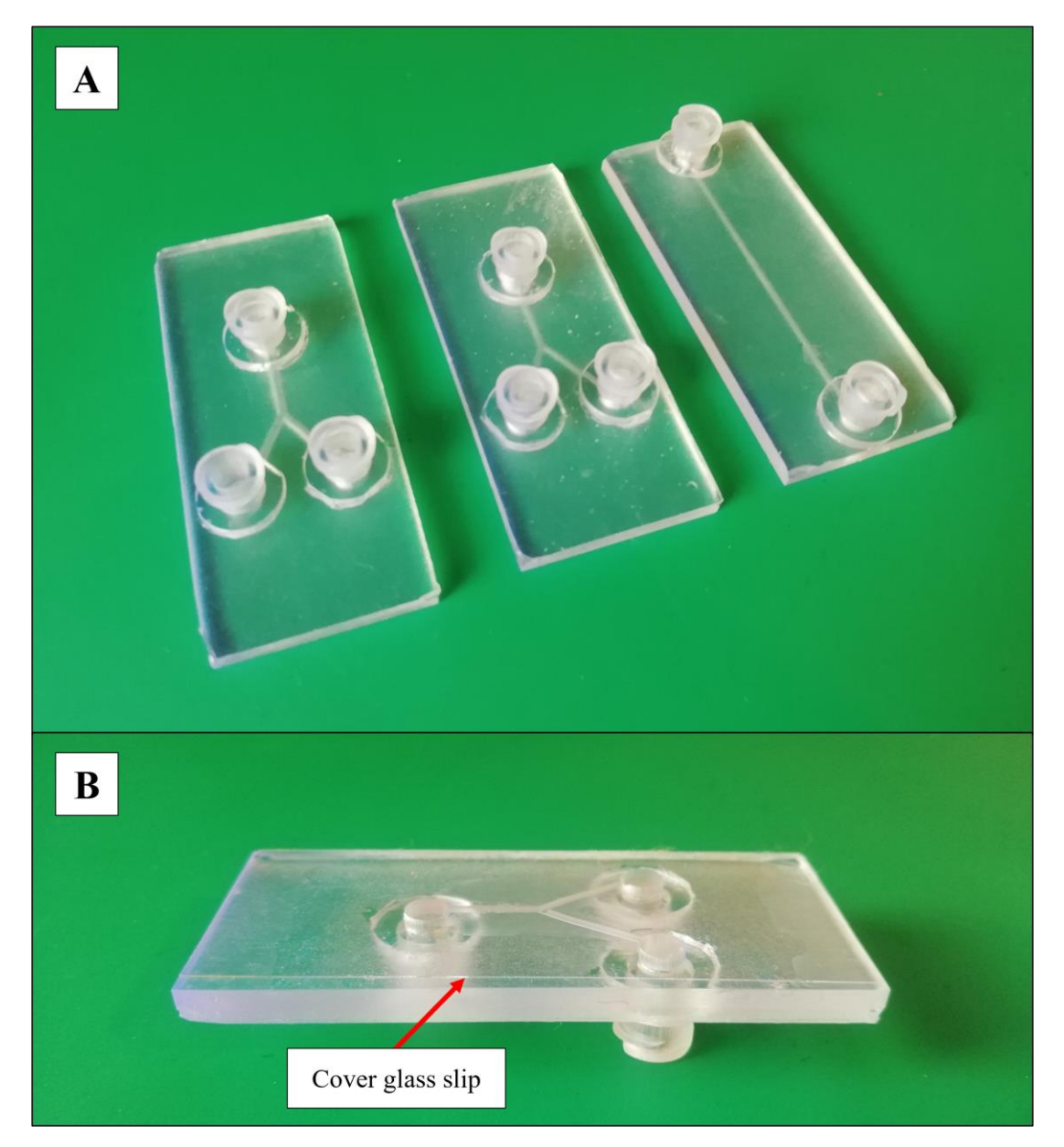


Figure 28: Produced parts for experimental μPIV investigations. A: Three plates incorporating flow channels. Outlines of the microchannels and luer locks glued to the top of the plates can be seen. B: Bottom of a plate. The red arrow indicates the edge of the cover slip glued to the bottom of the channel with additional resin.

#### 3.3.3 Lower airway and alveolar µPIV experiments

Once the channels were manufactured and useable, µPIV measurements could finally be performed with them. Since all channels represented different lung generations and therefore also had different geometric properties, settings for the measurements had to be calculated individually for each channel.



Especially the volume flow rate  $\dot{V}$  given off by the syringe pump had to be set so that the flow velocity inside the channel was in a reasonable order of magnitude. Also, the time delay  $\Delta t$  between two adjacent laser pulses had to be coordinated according to the chosen flow speeds. Moreover, the magnification of the microscope was switched between 4-fold and 10-fold depending on the examined region of interest. The microscope was focused on a plane near the bottom surface of the plate, thereby capturing sharp images of the particles in the midplane of the duct.

For all trials with 4-fold magnification, a solution of 95% distilled water and 5% FluoRot W4 fluorescent polystyrene seeding particles (microParticles GmbH, Berlin, Gemany) with a 5-micrometer diameter, an excitation peak at 530 nanometers wavelength, and light emission at 607 nanometers were used. For measurements with 10-fold magnification, FluoRot Fi320 fluorescent polystyrene seeding particles (microParticles GmbH, Berlin, Gemany) with a 2-micrometer diameter and the same properties were used instead. The particle concentration in the solution was kept identical as well. Due to the nature of the experimental setup, measurements could only be taken in phases where the fluid traveled down the bifurcations or the alveolated duct, imitaing inhalation. A summary of the chosen settings is given in Table 11.

Region of interest	Set volume flow rate V [ml/min]	Laser pulse time delay Δt [μs]	Magnification	Fluid
Bifurcation 10 → 11	7.00	10	4×	95% distilled water, 5% 5µm particles
Bifurcation 15 → 16	0.60	50	4×	95% distilled water, 5% 5μm particles
Alveolated duct of generation 17	0.12	400	4×	95% distilled water, 5% 5µm particles
Alveolus	0.12	400	10×	95% distilled water, 5% 2μm particles

Table 11: Used channels, their specified regions of interest, as well as chosen settings for the μPIV measurements.

After a series of 100 raw images was captured for every trial, additional steps were taken in computational image treatment. Spatial calibration of the images was done to assign a specific number of micrometers to every image pixel, depending on the used magnification. This step was necessary because computation of correct flow velocities is obviously dependent on the particle distance travelled between subsequent images.

In preprocessing, the raw images were treated with three modules. Firstly, a Gaussian filter was applied to the images. Secondly, an image calculator causing addition of subsequent

pairs of raw images into one picture was utilized. Thirdly, an image generator was used. It calculated the average intensity of the input images.

After preprocessing, a mask was applied. Only the image content inside the mask was considered in the following processing step. Preprocessing and masking were both used to improve performance of the cross-correlation algorithm responsible for processing. No image postprocessing methods were applied. For better understanding, a visual representation of the complete computational image treatment process is given in Figure 29.

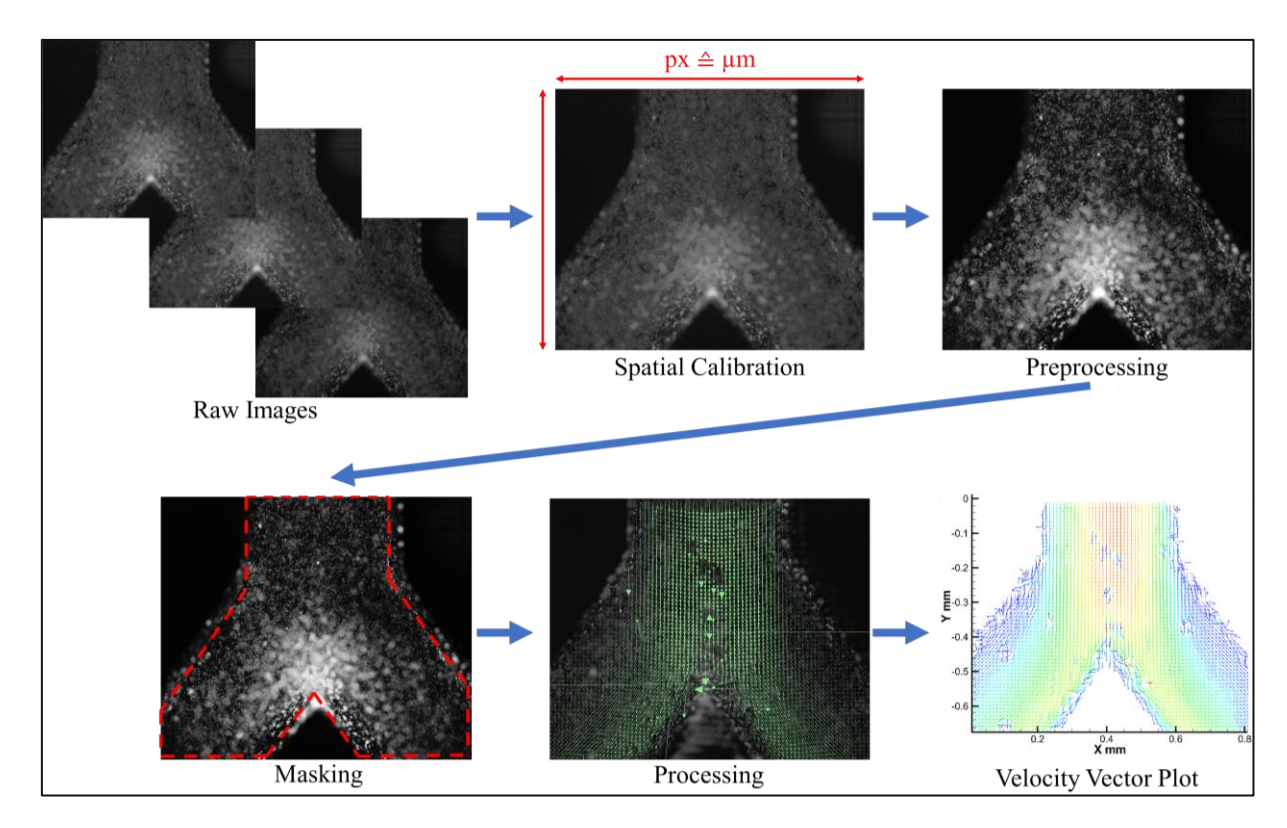


Figure 29: Image processing methodology. Raw images are taken and calibrated. After preprocessing and masking, the pictures can be algorithmically correlated and processed into a velocity vector plot.

# 4 Results and Discussion

Findings of the CFD simulations and μPIV experiments are described und discussed in the following subchapters. Firstly, results of the mesh independence studies are presented. Secondly, key findings, trends, and patterns of the turbulent and laminar simulations are shown. Thirdly, results stemming from experimental measurements are provided. At last, comparisons of simulated and experimental flow behaviors are gathered.

# 4.1 Mesh independence studies

Numerical values of the area-weighted average of wall shear stress over the entire upper airways and lower airway branch are given in Table 12 and are supported by a bar graph representation given in Figure 30. It can be seen that the mesh-specific wall shear stresses for both the upper airways and the lower airway branch are each in comparable ranges.

		Upper	airways	
	Coarse (0.45×10 <sup>6</sup> elements)	Medium (1.38×10 <sup>6</sup> elements)	Fine (3.27×10 <sup>6</sup> elements)	Very Fine (4.58×10 <sup>6</sup> elements)
Wall shear stress [Pa]	0.1909	0.1928	0.1968	0.1953
Average $y^+$ [-]	1.1011	1.1020	1.0356	1.0270
Maximum y <sup>+</sup> [-]	2.3008	2.3488	2.4969	2.4166
Average velocity A-A' [m/s]	4.0000	4.0000	4.0001	4.0001
Average velocity B-B' [m/s]	4.0663	4.0676	4.0709	4.0702
Average velocity C-C' [m/s]	3.9982	3.9933	3.9916	3.9920
Average velocity D-D' [m/s]	4.5660	4.5763	4.5797	4.5647
		Lower airs	way branch	
	Coarse (0.45×10 <sup>6</sup> elements)	Medium (1.03×10 <sup>6</sup> elements)	Fine (3.22×10 <sup>6</sup> elements)	Very Fine (5.86×10 <sup>6</sup> elements)
Wall shear stress [Pa]	0.3075	0.3278	0.3391	0.3161
Average velocity E-E' [m/s]	2.8612	2.9231	2.9664	2.9373
Average velocity F-F' [m/s]	1.5628	1.5407	1.5838	1.5497
Average velocity G-G' [m/s]	0.1665	0.1658	0.1685	0.1700
Average velocity H-H' [m/s]	0.0237	0.0150	0.0159	0.0171
Average velocity I-I' [m/s]	0.0033	0.0029	0.0022	0.0029

Table 12: Numerical values of tracked flow properties to assess mesh independence.



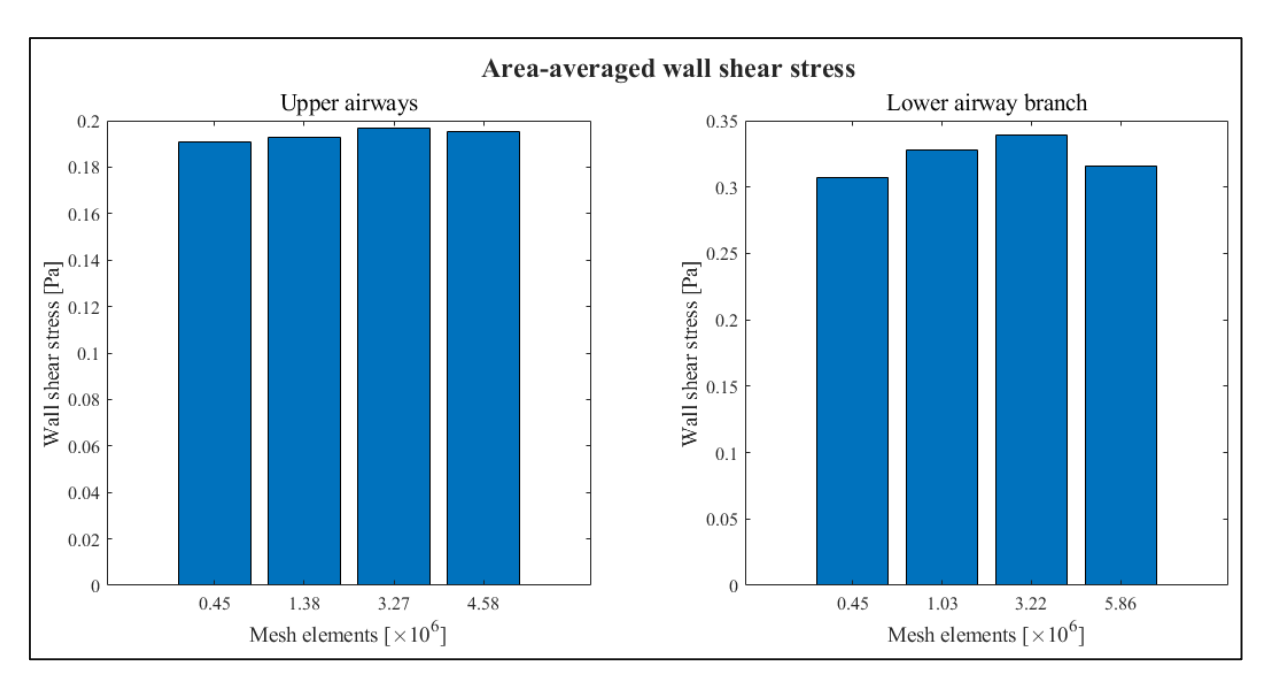


Figure 30: Wall shear stresses of the coarse, medium, fine, and very fine meshes of the upper and lower airways, resulting from the mesh independence simulations.

Furthermore, the average and maximum  $y^+$ -values of the wall-adjacent mesh cells of the upper airway meshes are written down in Table 12 and depicted in Figure 31 as well. It is visible that with the meshing strategy described in the methods, average  $y^+$ -values could be kept around 1, while maximum values change slightly from approximately 2.3 to 2.4 depending on the employed mesh.

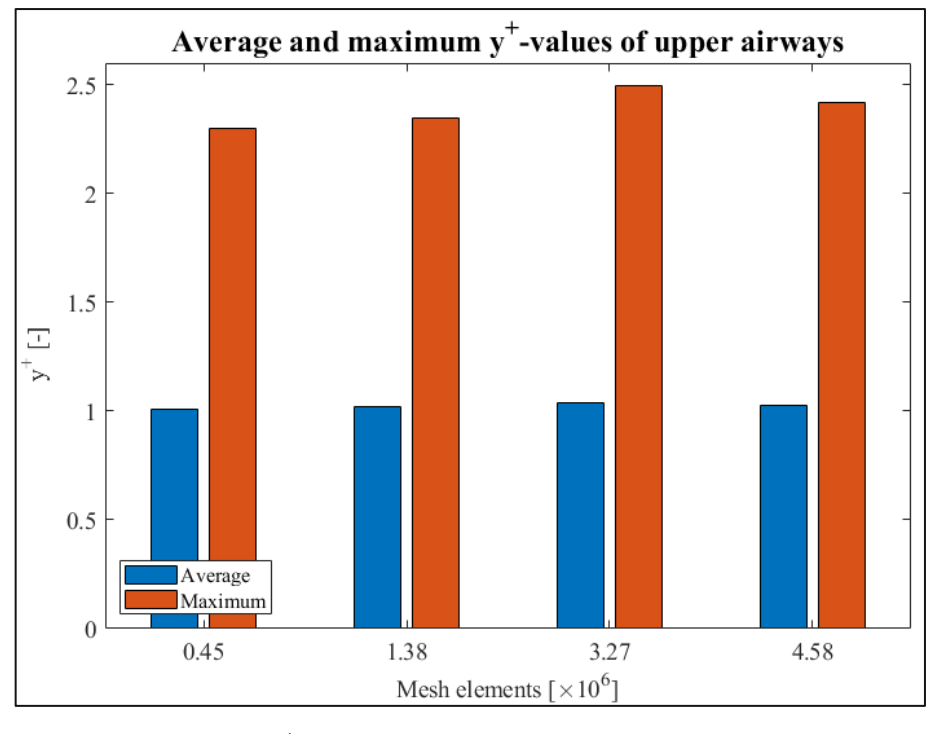


Figure 31: Average and maximum  $y^+$ -values of the coarse, medium, fine, and very fine meshes of the upper airways, resulting from the mesh independence simulations.



For the area-weighted average velocity of the lung sections, results produced by different meshes are similar as well. Just the coarse mesh of the lower airway branch produced slightly larger numerical deviations in its velocity predictions. This can be found in the data given in Table 12 and the respective visual representation Figure 32.

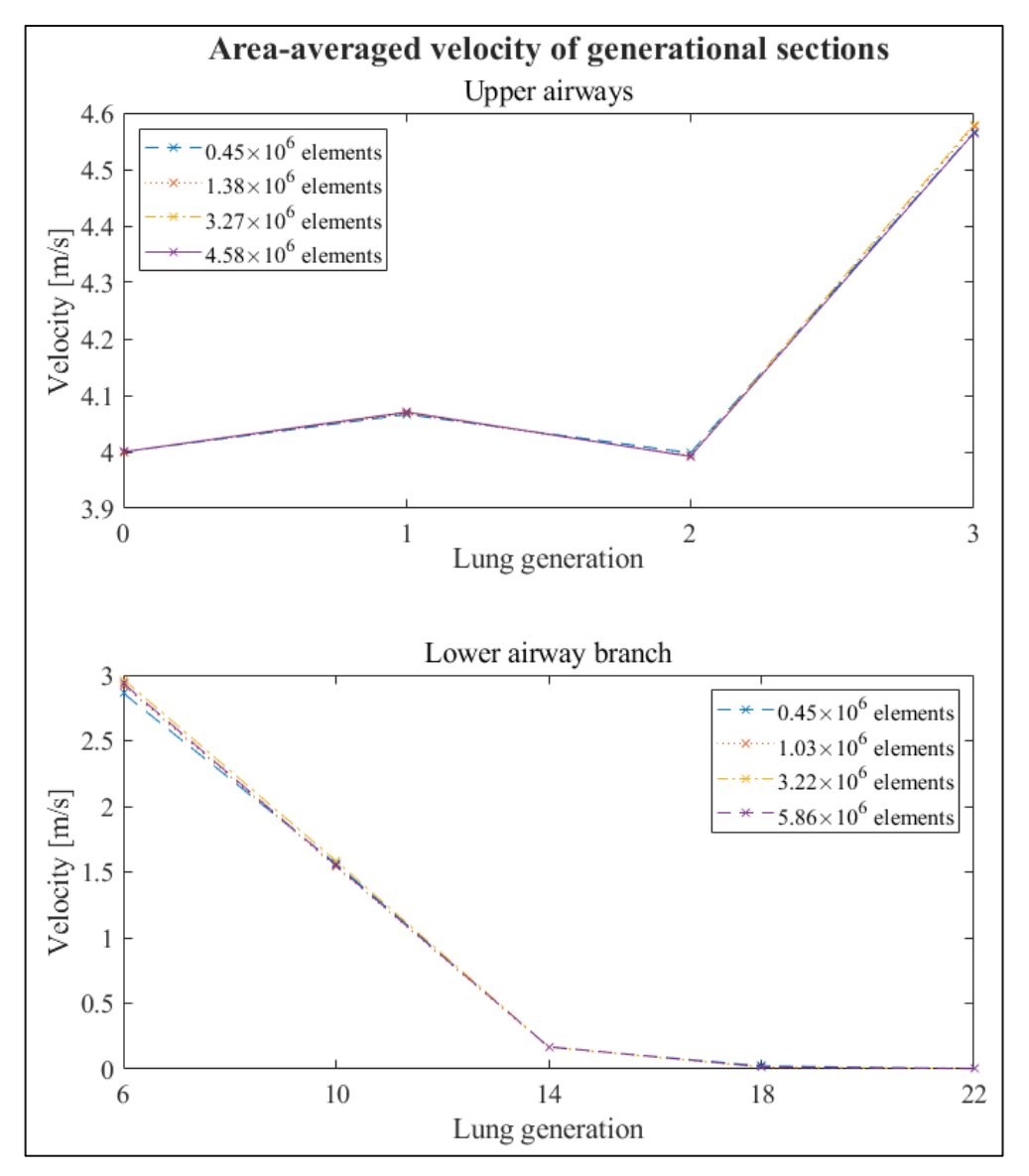


Figure 32: Area-averaged velocities of generational sections through the lung geometry, resulting from the mesh independence simulations. The coarse, medium, fine, and very fine meshes of the upper and lower airways are compared against each other.

Here, it should be noted that small numerical errors always appear when the meshes are compared against each other. However, the only grid where these differences appear to be substantial is the coarse mesh of the lower airway branch. Incidentally, this is also the only mesh with some elements whose quality was deemed "undesirable" according to Table 4. For all other meshes, the solutions might still not be truly mesh-independent, but the errors appear to be in an acceptable working range for engineering applications.

As a side note, it can already be found in the methods chapter, that for the main simulations the coarse and medium meshes were employed for the upper airways, as well as the medium mesh for the lower airway branch. Considering the results of the mesh independence studies presented here, this choice might be better understandable now.

#### 4.2 SHFJV simulations

Through reasonable utilization of CFD, valuable insights into the airflow phenomena during SHFJV and their impact on the lungs could be gained. Still, before showing findings, the challenge of effectively presenting the tremendous amounts of data generated by multiple transient simulations should be acknowledged.

Due to the extensive nature of lung fluid dynamics as a field of research and the limited space available in this thesis, it is not feasible to include all imaginable results. Therefore, representative flow properties, evaluated regions of interest, as well as examined time spans during SHFJV have been carefully selected, focusing on key findings.

Concretely, for every simulation type employed (entirely laminar, combined SST  $k-\omega$  and laminar, combined LES and laminar), relevant analysis has been provided on mean velocity distributions, turbulence quantities, and pressure distributions. All these properties have been evaluated for three subcycles of the overlying SHFJV-cycle (Figure 33):

- HFJV subcycle: An oscillation of isolated HFJV between 0.1 and 0.19 seconds.
- Inspiration SHFJV subcycle: An oscillation of HFJV superimposed with LFJV causing inhalation between 1.495 and 1.585 seconds.
- Expiration SHFJV subcycle: An oscillation of HFJV superimposed with LFJV causing exhalation between 3.995 and 4.085 seconds.

Additionally, it is noteworthy that several result tables, containing complete visual representations of midplane velocity contours and vectors, as well as wall pressure contours for several regions of interest have been intentionally moved to Appendix A and Appendix B. In these appendices, for each turbulence model and each cycle, the aforementioned flow variables are depicted for nine respective time points visible in Figure 33. This maintains readability of this work's main body, as including these comprehensive tables here would disrupt logical consistency. However, it is necessary to emphasize these complete sets of results, supporting the presented findings, as well as the conclusions drawn later.

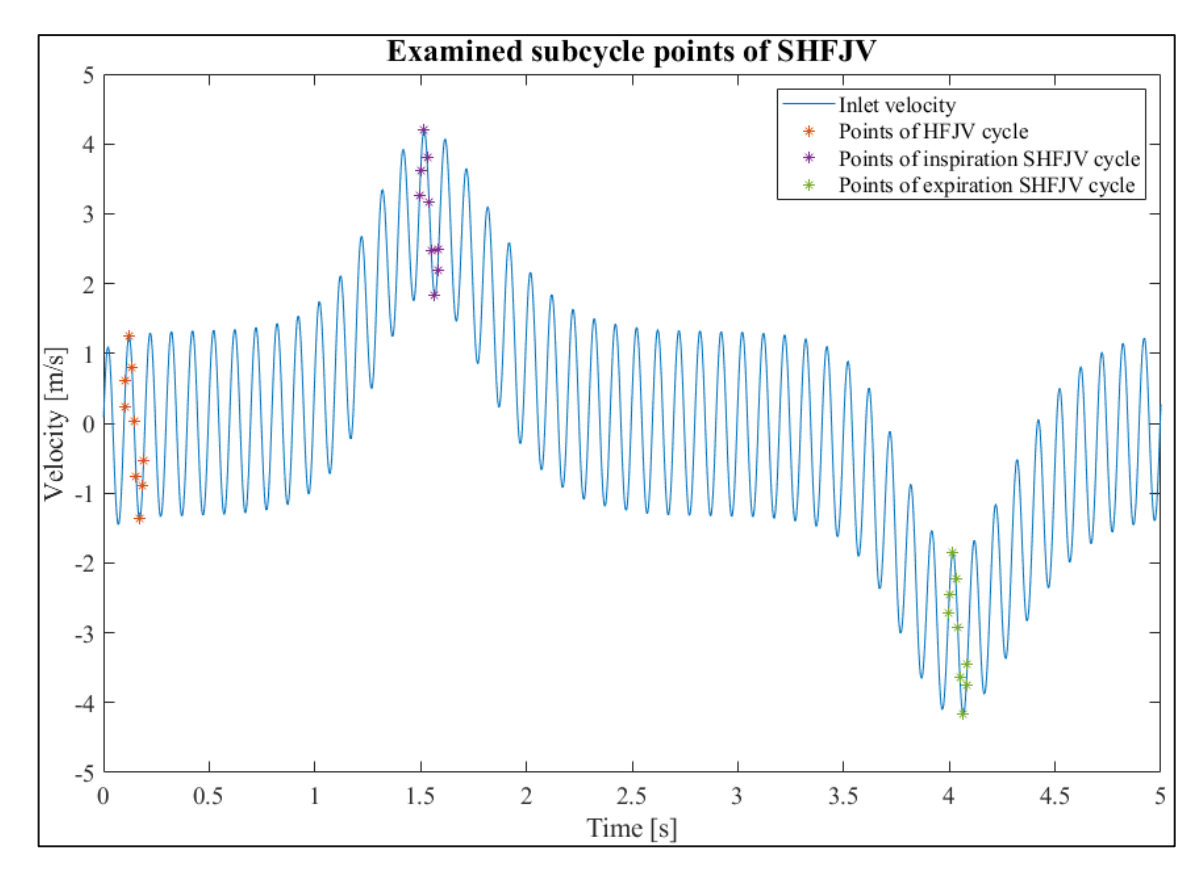


Figure 33: The SHFJV cycle, divided into three groups: HFJV cycle, inspiration SHFJV cycle, and expiration SHFJV cycle. The time points are plotted over the inlet velocity to gain sense of their position within the complete cycle.

## 4.2.1 Mean velocity distributions

In CFD lung research, the qualitative and quantitative characteristics of flow velocities hold great importance and serve as a cornerstone for understanding airflow dynamics in the lungs. Appendix A contains the airflow velocity contours and vectors on the symmetric midplanes of all chosen regions of interest for the mentioned subcycles. These regions of interest have been defined as the bifurcations from generation 0 to 1, 1 to 2, 2 to 3, 5 to 6, 10 to 11, and 15 to 16, as well as the duct of generation 17 and a single alveolus of generation 17.

Looking at the qualitative velocity patterns at the bifurcations, many influential phenomena can be described. For example, every time air flows down the airway geometry towards the alveoli, a stall with flow separations at the outer areas of the bifurcating ducts is visible. Flow separation behavior is caused by the viscosity and inertia of the air. The main characteristic of such a separation is the detachment of a boundary layer from a surface behind an edge. As the flow becomes detached from the surface, it takes the forms of eddies and vortices in a shear layer zone. Below the shear layer, the airflow follows into a region of recirculating flow. This behavior is schematically shown in Figure 34, but can also be distinguished in the results depicted in Figure 35. During the outflow of air out of the lungs, the separation of flow can also be observed at the joining bifurcations, but only to a lesser extent.

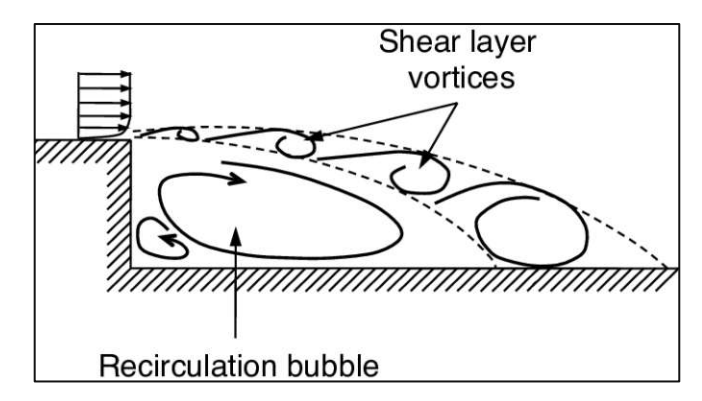


Figure 34: Illustrative depiction of flow separation at a backwards facing step. Behind the edge, the flow separates, creating a shear layer containing vortices, and a recirculation area. Modified after [71].

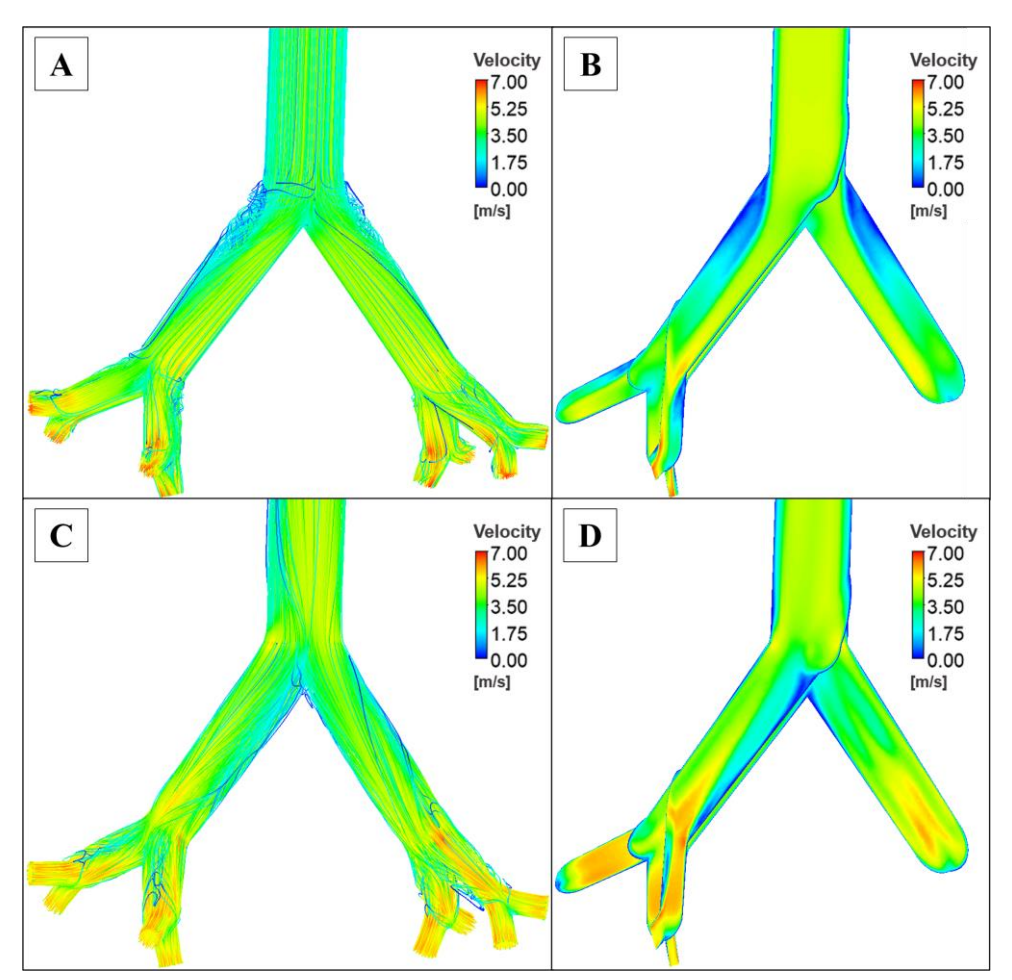


Figure 35: Maximal inhalation and exhalation velocities for the upper airways as predicted by the SST  $k-\omega$ simulation. A: Streamline plot during maximal inspiration. Circulating streamlines with low velocity can be seen. B: 3D assembly of midplane velocity contours during maximal inspiration. The flow stall at the left and right bifurcation edges is visible. C: Streamline plot during maximal expiration, indicating the presence of recirculation. D: 3D assembly of midplane velocity contours during maximal expiration. The flow separation phenomena can still be distinguished.



Naturally, the scope of the flow separations varies with the magnitude of the inlet velocity and the inspected generation. While the flow stall is still present during maximal inspiration at generation 5 to 6, it is not identifiable for lower generations or at lesser incoming velocities.

In the phases, where only HFJV is acting, there is another interesting result to be discussed. When the airflow direction switches from inspiration to expiration, the recirculating airflows behind the inspiratory flow stalls are also blown upwards along the airway ducts. This results in airflow regions with a slightly higher velocity magnitude in the middle of the next-highest airway duct (Figure 36). However, before the airflow direction switches to the inspiration phase of the next HFJV cycle, the velocity field has already homogenized again. This phenomenon of recirculating flows being carried upwards is especially visible at the two uppermost bifurcations of the lungs. For SHFJV inhalation or exhalation, this effect cannot be observed, because the direction of the superimposed, pulsating airflow does not change, but only its magnitude of inspiration or expiration.

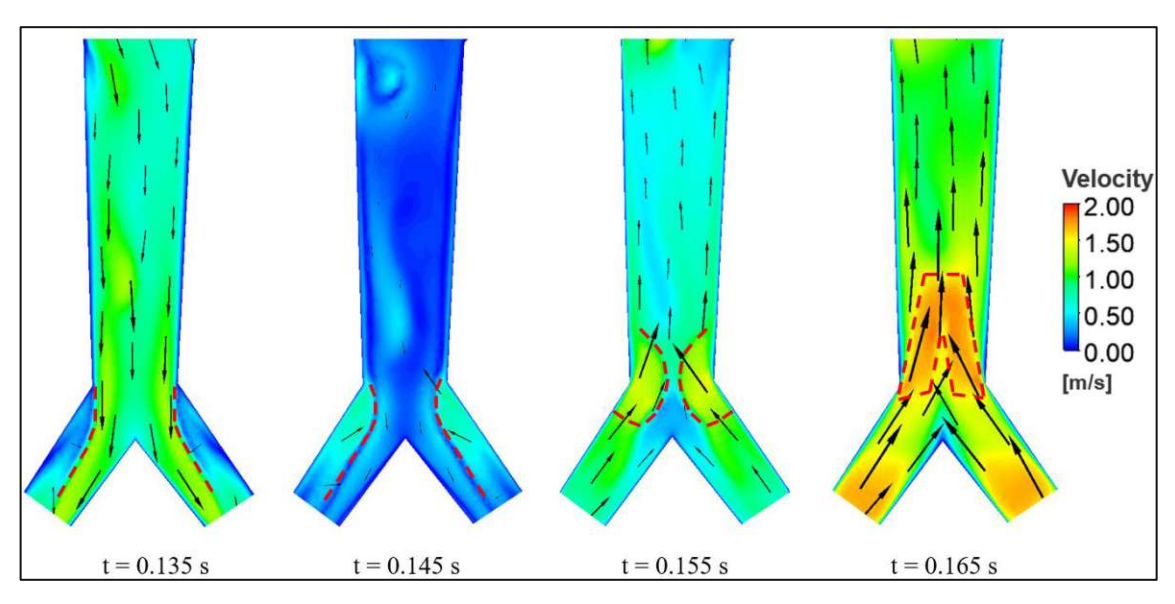


Figure 36: Midplane velocity contours and vectors of the bifurcation from generation 1 to 2. The recirculation bubbles are getting carried upwards from generation 2 to generation 1 with the main expiration stream during HFJV. Flow stalls transforming to higher speed regions during HFJV expiration are indicated through the red dashed lines. Results taken from the LES.

Furthermore, it is visible that the main velocity stream traveling downwards always hits the tip of the next bifurcation, thereby being split into two new mainstreams, each traveling down their own duct. Contrary, when air is traveling upwards, two airstreams fuse into one stream. Depending on the exact geometrical properties of the respective airway generation, these regular velocity distribution patterns are disorganized by the fact that the branches of the airway do not lie in the same plane but at an angle to each other.

During phases of SHFJV where only HFJV is acting, the inflow and outflow of air and all associated phenomena balance each other out. Intervals where the HFJV is superimposed with the inspiration LFJV stream are marked by periodical fluctuations in inhalation velocity. However, airflow is continuously guided into the lungs. Contrary, when the LFJV superimposed onto the HFJV ends, therein causing exhalation, a continuous outflow of air can be described. Again, the HFJV causes periodical fluctuations in the exhalation velocity, but does not overturn the airflow direction.

Concerning quantitative analysis of the velocity distributions, many regions of interest can possibly be examined. For the thesis at hand, the maximum area-weighted velocity magnitudes during the inspiration SHFJV and expiration SHFJV subcycles at the end of each generation have been reported. This constitutes a suitable representation of how the generation-wise magnitude of airflow velocity changes. Results are provided in Table 13 and visualized in Figure 37.

	Maxima	l inspiration velo	city [m/s]	Maxima	l expiration veloc	ity [m/s]
ζ	Entirely laminar	Combined SST <b>k</b> - <b>ω</b> and laminar	Combined LES and laminar	Entirely laminar	Combined SST <b>k-ω</b> and laminar	Combined LES and laminar
0	4.101	4.102	4.104	4.277	4.260	4.288
1	4.446	4.440	4.455	4.669	4.646	4.692
2	5.380	5.366	5.390	5.009	5.004	4.505
3	4.126	4.125	4.120	3.781	3.781	3.591
4	3.431	3.529	3.426	2.980	2.980	2.831
5	2.702	2.703	2.670	2.451	2.451	2.328
6	1.984	1.986	1.983	1.676	1.679	1.601
7	1.530	1.530	1.528	1.364	1.364	1.296
8	1.135	1.135	1.134	1.008	1.008	0.958
9	0.780	0.780	0.779	0.661	0.661	0.629
10	0.577	0.577	0.576	0.489	0.489	0.465
11	0.377	0.377	0.377	0.306	0.306	0.291
12	0.249	0.249	0.249	0.216	0.216	0.206
13	0.156	0.156	0.156	0.133	0.133	0.127
14	0.100	0.100	0.100	0.087	0.087	0.083
15	0.060	0.060	0.060	0.051	0.052	0.049
16	0.026	0.026	0.026	0.024	0.024	0.023
17	0.013	0.013	0.013	0.012	0.012	0.011
18	0.007	0.007	0.007	0.006	0.006	0.006
19	0.008	0.008	0.008	0.008	0.008	0.008
20	0.004	0.004	0.004	0.004	0.004	0.004
21	0.002	0.002	0.002	0.002	0.002	0.002
22	0.002	0.002	0.002	0.002	0.002	0.002

Table 13: Maximal area-averaged velocities at the end of each generation during inspiration SHFJV and expiration SHFJV subcycles for all simulation types.

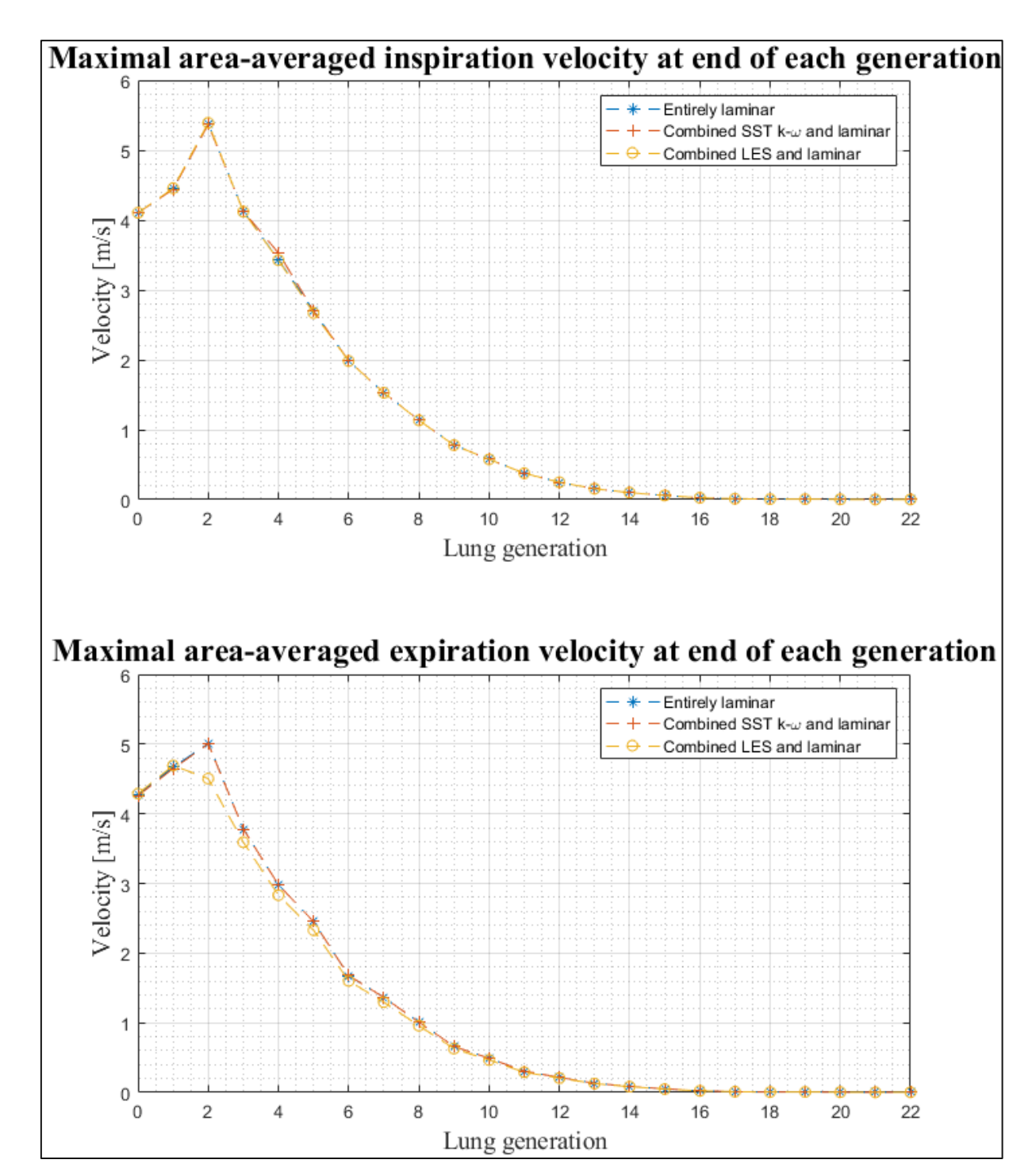


Figure 37: Maximal area-averaged velocities at the end of each generation during the inspiration SHFJV and expiration SHFJV subcycles for all simulation types.

Consequently, it can be deduced from the results presented here and in Appendix A, that the velocity distributions along the conductive airway system are very similar for all three performed simulation types. Only negligible numerical differences and a slight underprediction of exhalation flow speeds by the combined LES and laminar model can be detected, but the holistic properties and described phenomena of the airflow velocity field stay almost identical. Both for the upper airways and the lower airway branch, flow patterns



received by different simulation types seem almost indistinguishable. The described phenomena arising in the symmetrically branching airway model are in great accordance with [34]. Velocity magnitudes are in good agreement with publications such as [29] and show the generation-wise propagation described in [8].

Moving the discussion from the conductive system to assessment of airflow in the alveolated regions, interesting observations can be disclosed as well. Figure 38 depicts the time-dependent velocity changes in an alveolus of generation 17 by showing midplane contours and velocity vectors of selected time points during each of the designated subcycles.

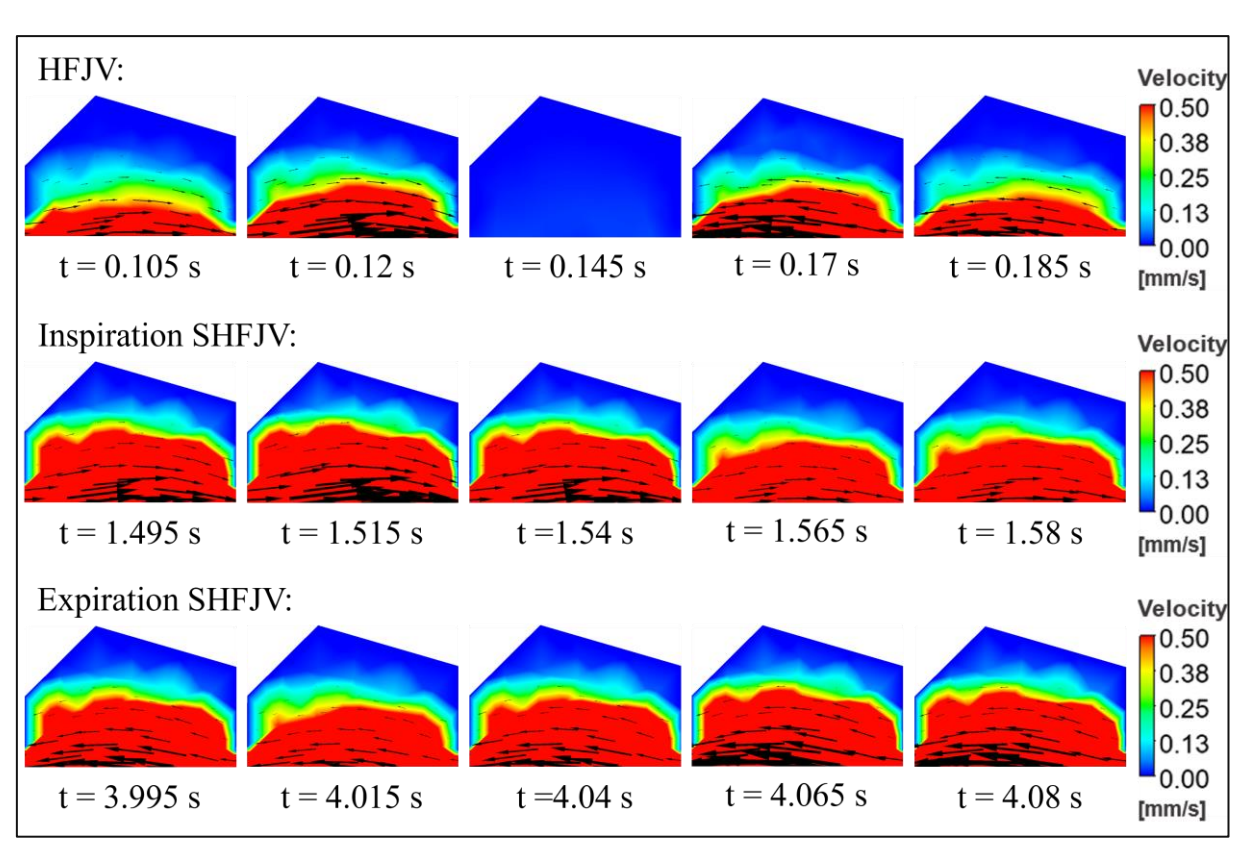


Figure 38: Velocity contours and vectors of an alveolus during the three subcycles of SHFJV. Results taken from the combined SST  $k-\omega$  and laminar simulations.

During the isolated HFJV oscillation, alternating inflow and outflow directions of air can be seen. First (t = 0.105 s), air is slightly drawn into the opening of the alveolus. While in the middle region airflow is still detectable, velocity in the most distant areas of the alveolus is close to zero. As the velocity in the adjacent duct gets bigger (t = 0.12 s), the influx of air into the alveolus increases as well. Still, the outermost regions of the alveolus are not reached through convective transport mechanisms. After the inlet velocity gets lower again, it reaches the point of exactly zero (t = 0.145 s). Here, no airflow in the alveolus is visible. This pattern is then repeated for expiration, as indicated by the velocity vectors now

pointing in the opposite direction (t = 0.17 s and t = 0.185 s).

However, at this point it is reasonable to mention that this in- and outflow near the alveolus does not necessarily coincide with the transport of fresh air for gas exchange. Rather, it is very likely that the isolated HFJV only causes dead space ventilation, meaning air that has already been used for gas exchange is rapidly transported back and forth through the lungs without ever leaving them. The idea of this so-called pendelluft is therefore not to contribute to respiration, but rather to cause mechanical effects in the lungs.

Nevertheless, for the inspiration and expiration SHFJV subcycles, the concept of alternating flow patterns still holds. The major difference is the LFJV airstream, causing a stronger underlying inhalation or exhalation. The idea that this superimposing principle is propagated into the alveoli is supported by the varying velocity magnitudes in the examined alveolus during the subcycles. Maximal airflow penetration of the alveolus emerges when HFJV and LFJV interfere constructively, while it is minimal when HFJV and LFJV interfere destructively. Picking the considerations of dead space ventilation and pendelluft up again, it is likely that the contribution to respiration and gas exchange of SHFJV lies within the air transport due to LFJV, as opposed to the already mentioned isolated HFJV subcycle.

Numerical values of velocity magnitude in the examined alveolus reach from 0 meters per second to about 0.0016 meters per second, corresponding to 1.6 millimeters per second. While the maximum velocities at any given time occur in the area where the main flow is drawn from the duct into the opening of the alveolus, the lowest detectable velocities are always predicted in the outermost areas of the alveolus. In these distal regions, specific recirculation patterns of the almost non-moving air can even be distinguished (Figure 39). With the alternation of airflow direction, the rotation of these circulating airflows changes as well. However, the role of recirculating flows inside the alveolus and their specific contribution to respiration, as opposed to diffusive gas exchange phenomena, it is still controversially discussed among researchers [7].

For alveoli located in lower generations of the airway, velocity decreases further in unison with the results presented in Table 13 and Figure 37. Despite the reduced velocities in the lowest generations, the explained patterns and phenomena still apply. Generally speaking, the predicted flow behavior in the alveoli is in line with physiological descriptions, such as given in [8] and findings of respiratory simulations and experiments like [7, 60, 61, 65].



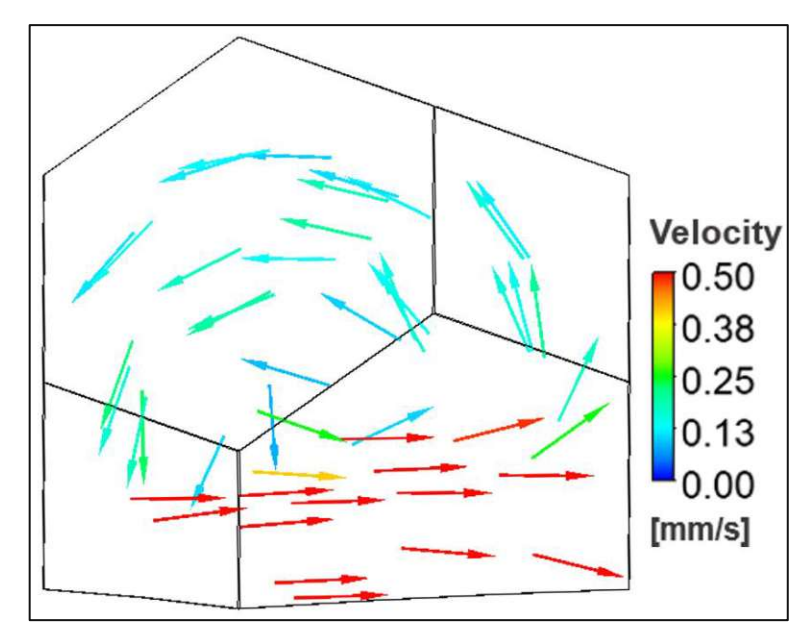


Figure 39: 3D velocity vector plot of a recirculating flow inside an alveolus of generation 17. Results taken from the entirely laminar simulations.

#### 4.2.2 Velocity fluctuations and turbulence properties

Having outlined flow features discernible from the mean flow field, it is a logical next step to turn to fluctuating turbulence properties. Naturally, since only the SST  $k-\omega$  and LES models incorporate turbulence, only the results for these two simulation types and the upper airway simulations will be mentioned in the following. As the laminar simulations do not include turbulence, they cannot be further discussed in this subchapter.

Generally speaking, qualitative indicators for turbulence are large and small eddy structures, vortices, and swirls, areas of flow unsteadiness and energy dissipation, as well as mixing flow zones. In the given problem, these properties must be specifically searched for, as laminar motion and coherent structures dominate the flow pattern in the airways. However, this does not mean that turbulence does not occur at all.

Large eddies are generally present in the aforementioned recirculation bubbles. However, they are rather slow-moving and of regular nature, and carry only little turbulence. As they are generated behind the flow stall at splitting ducts, they do not really interact with the main flow. This changes during expiration, when the recirculating eddies behind the descending airway bifurcations are mixed with exhaled air from lower generations and are blown up the lungs together. Through this mixing mechanism, turbulence is induced.

Another source of turbulence are the shear layer vortices caused by flow separation during high inhalation velocities. The shear layer vortices at the flow separation create relatively high turbulence. In these areas, unsteady motion of the separation boundary layers can be seen. The same effect can be described to a lesser extent for high exhalation speeds.

Furthermore, turbulence can be induced in the upper airways through the already discussed mixing of two main airstreams when air is traveling upwards during expiration. The airstreams join in a mixing zone where the two connecting lower airway ducts merge into the next higher airway duct. In these areas, turbulent effects can be described as well.

Nevertheless, it seems that conditions for a strong or even fully developed turbulent flow along the trachea or upper airway ducts are not given. Hence, the overall flow properties are still mostly propagated laminarly.

Figure 40 shows the turbulence kinetic energy k and the turbulence intensity at the duct midplanes during maximum inhalation and maximum exhalation, as predicted by the SST  $k-\omega$  model. Turbulence intensity is a dimensionless number defined as the ratio of fluctuating velocity components to the mean velocity components, and it represents the relative intensity of velocity fluctuation.

For the maximum inhalation velocity during the SHFJV cycle, it can be clearly seen that the highest turbulence kinetic energy accumulates in the shear layers where the flow separates. Also, at the point where the mainstream is split by the bifurcation of generation 2 to 3, large turbulence kinetic energy is present. The highest detected turbulence kinetic energy values for inhalation are just below 0.70 meters squared per second squared.

Regarding turbulence intensity, a similar picture presents itself. The highest values of around 0.62 can be distinguished for the shear layer vortices, while the mainstream seems to be mostly laminar. An increased turbulence intensity in the recirculation areas can be detected, as the mean airflow moves rather slowly there, and the fluctuating velocities are weighted more strongly.

For the maximum exhalation velocity during the SHFJV cycle, turbulence quantities present themselves in a different way. Turbulence kinetic energy reaches its maximum in the lower third of generation 1 with a value of approximately 0.84 meters squared per second squared. However, a clear distinction of a shear layer zone is not possible. Rather, multiple mixing phenomena seem to cause higher turbulence kinetic energy in the center of each airway duct.

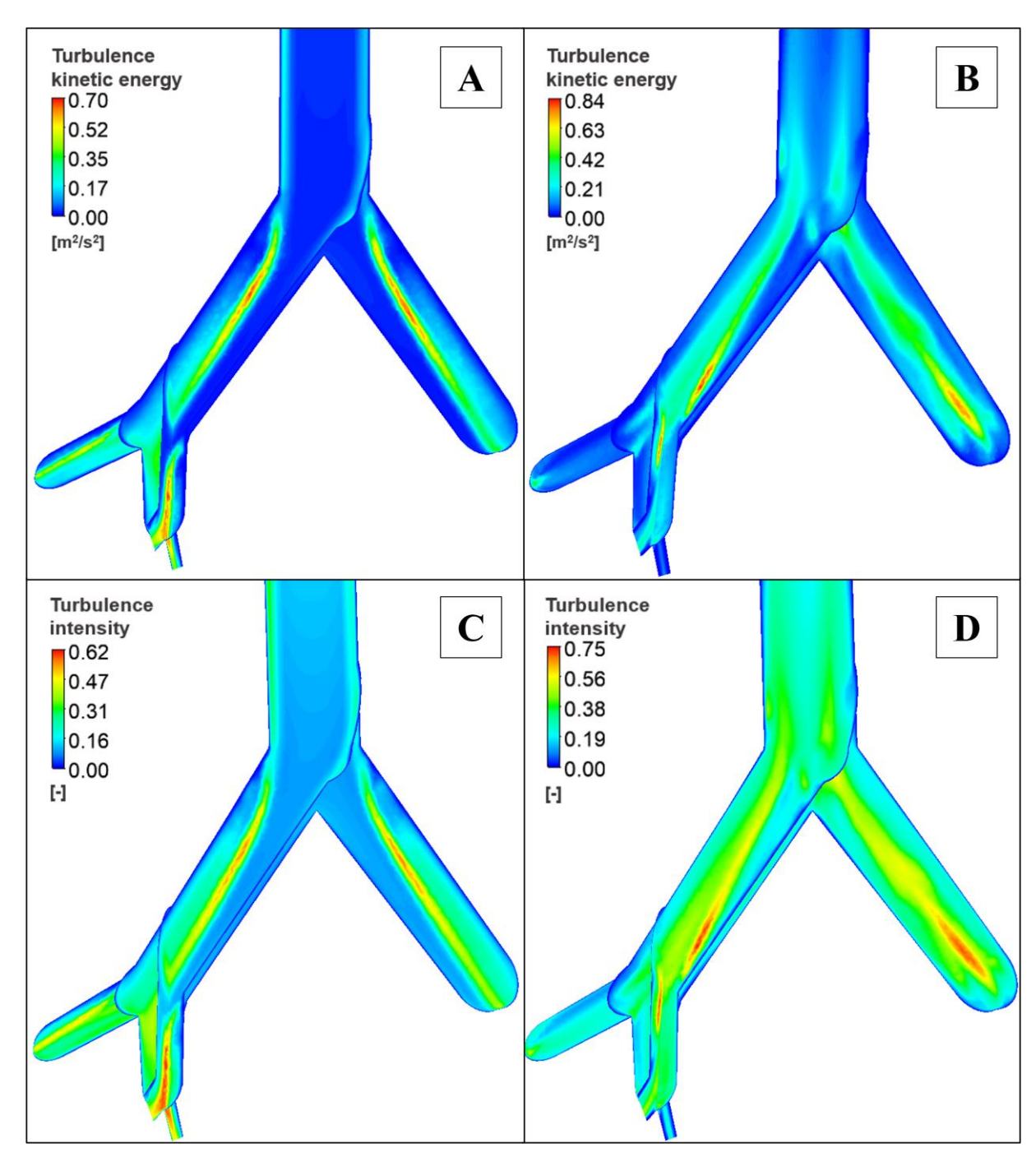


Figure 40: 3D assembly of midplane turbulence kinetic energy and turbulence intensity contours as representative turbulence quantities. Results taken from the SST  $k-\omega$  simulation. A: Turbulence kinetic energy during peak SHFJV inhalation. B: Turbulence kinetic energy during peak SHFJV exhalation. C: Turbulence intensity during peak SHFJV inhalation. D: Turbulence intensity during peak SHFJV exhalation.

Concerning the turbulence intensity, values of up to 0.75 and their visualization suggest that the airflow during maximal expiration is not fully laminar. While air flows out of the lungs coherently on a larger scale, there still are some underlying flow fluctuations and secondary flows. Similar ideas on turbulence to the ones presented can be found in [33, 39, 42, 43].



#### 4.2.3 Pressure distributions

Next to velocity flow patterns, pressure distributions along the fluid domain provide valuable insights into airflow behavior. For transient simulations, two distinct phenomena must be considered:

- Spatial pressure changes: The pressure difference between two spatial points at a certain time is usually referred to as a pressure drop. A fluid will always flow from a region of higher pressure to a region of lower pressure.
  - A pressure drop occurs when turbulences or viscous shear stresses like wall shear stresses lead to the dissipation of energy. Since pressure can be defined as energy per volume, pressure decreases with the dissipated energy. Compensating the dissipated energy, an airflow is initiated. A high pressure drop will usually lead to a high flow velocity.
- Temporal pressure changes: The presented results stem from a time-transient simulation, meaning that time-marching pressure- and velocity effects must be taken into account. Since the velocity and the pressure gradient are carried on between two distinct timesteps via the governing momentum equations, it cannot be assumed that the prevailing pressure conditions are purely due to spatial pressure losses, but that there are also time-dependent pressure changes influencing the result.

Further, it must be mentioned that since the airway geometry was divided into two parts, the pressure distributions of the upper and lower airways need to be viewed separately. Nevertheless, interesting phenomena are almost identical for both parts and can still be shown in a holistic context.

Considering spatial pressure drop, a common way to analyze results in lung CFD simulations is to report wall pressure contours of the airways [19, 29, 35, 39]. As already mentioned, the wall pressure contours for the examined subcycles are given in Appendix B. Table 14 and Figure 41 show the biggest drops in wall pressure that occurred for each simulation type and each examined subcycle.

Entirely laminar - Maximal wall pressure drop		
SHFJV subcycle	Upper airways [Pa]	Lower airway branch [Pa]
HFJV	21.62	63.59
Inspiration SHFJV	36.23	30.06
Expiration SHFJV	36.76	43.09
Combined SST k-ω and laminar - Maximal wall pressure drop		
SHFJV subcycle	Upper airways [Pa]	Lower airway branch [Pa]
HFJV	21.78	13.64
Inspiration SHFJV	36.88	30.27
Expiration SHFJV	36.92	43.15
Combined LES and laminar - Maximal wall pressure drop		
SHFJV subcycle	Upper airways [Pa]	Lower airway branch [Pa]
HFJV	21.59	9.59
Inspiration SHFJV	36.06	30.19
Expiration SHFJV	35.16	39.80

Table 14: Maximal wall pressure drops occurring in the examined cycles for each employed turbulence model.

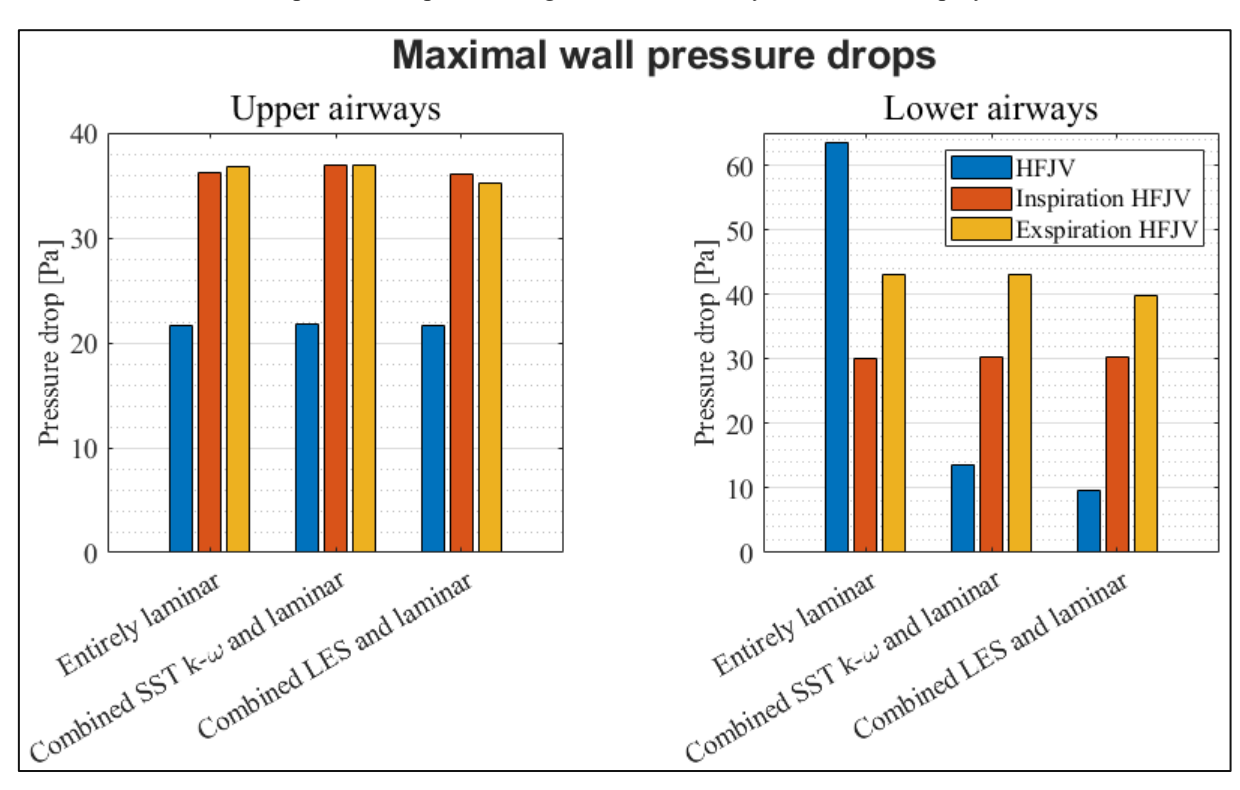


Figure 41: Maximal wall pressure drops occurring in the examined cycles for each employed turbulence model.

Generally, it can be deduced that the largest pressure drops arise when velocities are highest. When the maximum wall pressure drops of the upper airways and lower airway branch are combined, values in the approximate range of 60 to 80 Pascals can be ascertained for inspiration and expiration. For the HFJV only, combined maximal wall



pressure drops are lower and are located around 30 to 40 Pascals.

Compared to other scientific results, these values seem to be in a correct order of magnitude and comply with other publications. [72, 73] determined the wall pressure variation along Weibel's symmetric bronchial tree to be 60 Pascals. Lower values of 50 Pascals were reported by [29, 39], while [35] calculated pressure drops of about 100 Pascals. All of these results are furthermore in good agreement with the experiments from [74], producing a pressure difference of 75 Pascals across the entire respiratory tract.

Regarding temporal pressure changes, a connection between mean flow velocity and mean pressure over time can be drawn. Figure 42 depicts how the two variables act together, exemplary shown during one HFJV oscillation in the upper airways.

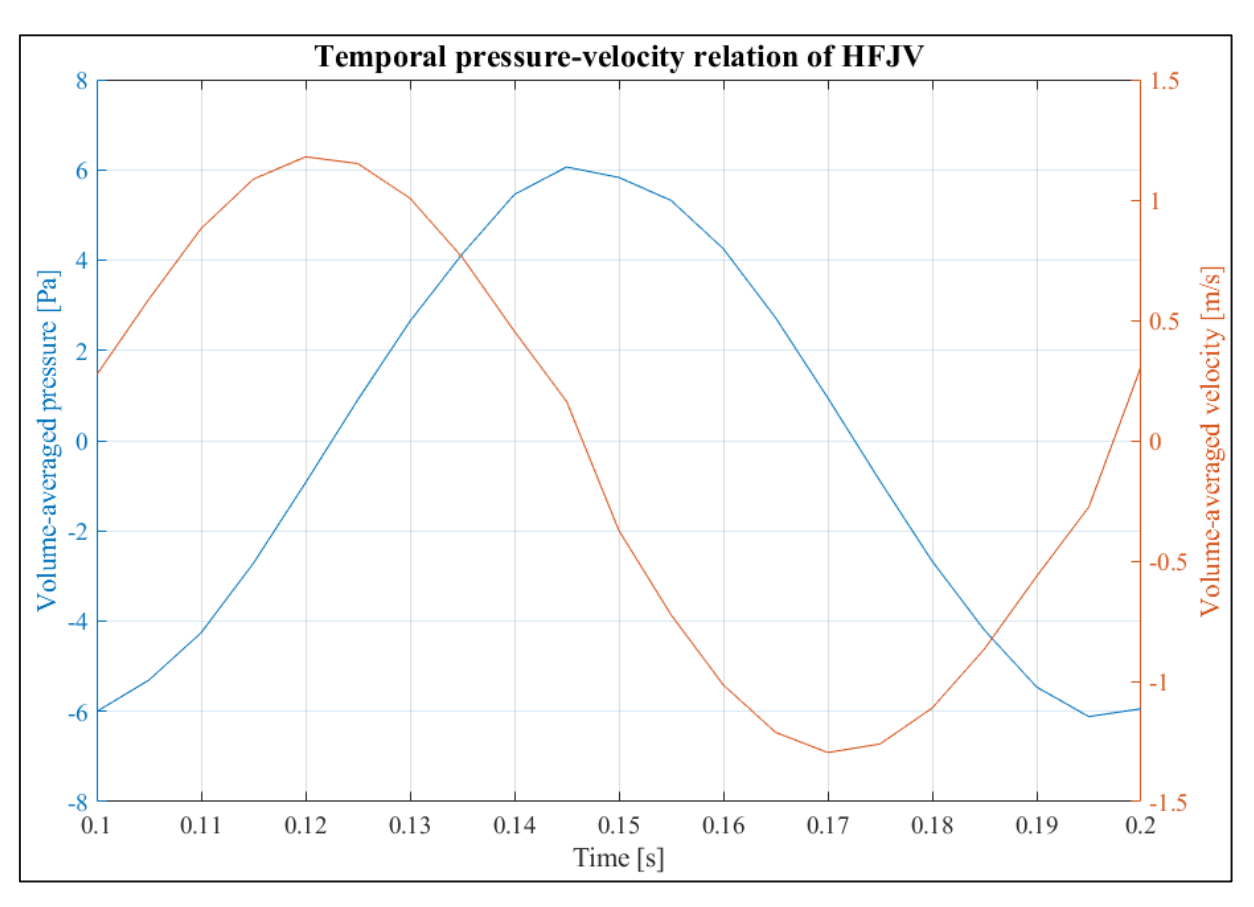


Figure 42: Time-dependent pressure-velocity relations during one HFJV subcycle. The pressure and velocity curves show a phase-shift, causing the oscillating behavior.

At the beginning, the volume-averaged pressure in the upper airways is negative. In other words, pressure inside the airways is slightly lower than the atmospheric pressure. This leads to an inflow of air, going along with a rising volume-averaged velocity. While the pressure increases and approaches zero, the velocity increases as well. When the airway pressure reaches zero, it is equal to the atmospheric pressure, meaning airflow needs to

stop. However, due to the inertia of the inflowing air, an overshooting reaction takes place: Air inflow continues, but the flow velocity starts decreasing, as airway pressure now increases into the positive range acting against the air's inertia. The airway pressure reaches its maximum when mean flow velocity approaches zero. Since now the pressure inside the airways is larger than the atmospheric pressure, the whole procedure is repeated, but this time causing an air outflow. Through this phase-shift principle, the oscillating HFJV is propagated. Similar considerations of this mechanism can be found in [41], for instance.

Phenomenologically, this resembles the propagation of electromagnetic waves, where the two alternating variables are the electric field strength and the magnetic field strength. Another example for such an overshooting reaction is the phase-shift between current and voltage in alternating electric current.

Moreover, this pressure-velocity relation was found to be identical for both the upper airways and the lower airway branch down to the alveoli for all performed simulation types. Only changes in numerical values of the temporal pressure-change are detectable. Also, this principle of the overshooting reactions can be applied throughout the entire SHFJV cycle since it does not interfere with the superimposed LFJV. This time-dependent effect caused by the HFJV might reveal some interesting implications on the mechanisms of action in the alveoli during SHFJV.

### 4.3 µPIV experiments

By performing µPIV experiments, results about real-world flow fields inside microchannels representing idealized lung bifurcations and alveoli could be yielded. Looking at the resulting midplane velocity vector plot for the bifurcation of generation 10 to 11 (Figure 43), it is noticeable that the flow field has a very uniform appearance regarding both velocity directions and magnitudes. Direction-wise nicely aligned maximal velocities of approximately 0.5 meters per second could be measured at the center of the duct in generation 10, while velocities steadily decrease towards the walls. Measured velocity magnitudes close to the walls are almost zero.

In the bifurcating zone, the velocity vectors distribute evenly between the two splitting ducts of generation 11. In both ducts, a faster-moving stream of about 0.2 to 0.4 meters per second flowing more towards the middle of the bifurcation is visible. The velocity magnitudes of the two splitting mainstreams in generation 11 are therefore clearly reduced

compared to the one in generation 10. On both the left and the right side in the transition zone between generation 10 and 11, a flow separation zone is visible, forming a region of slow fluid movement behind the edge.

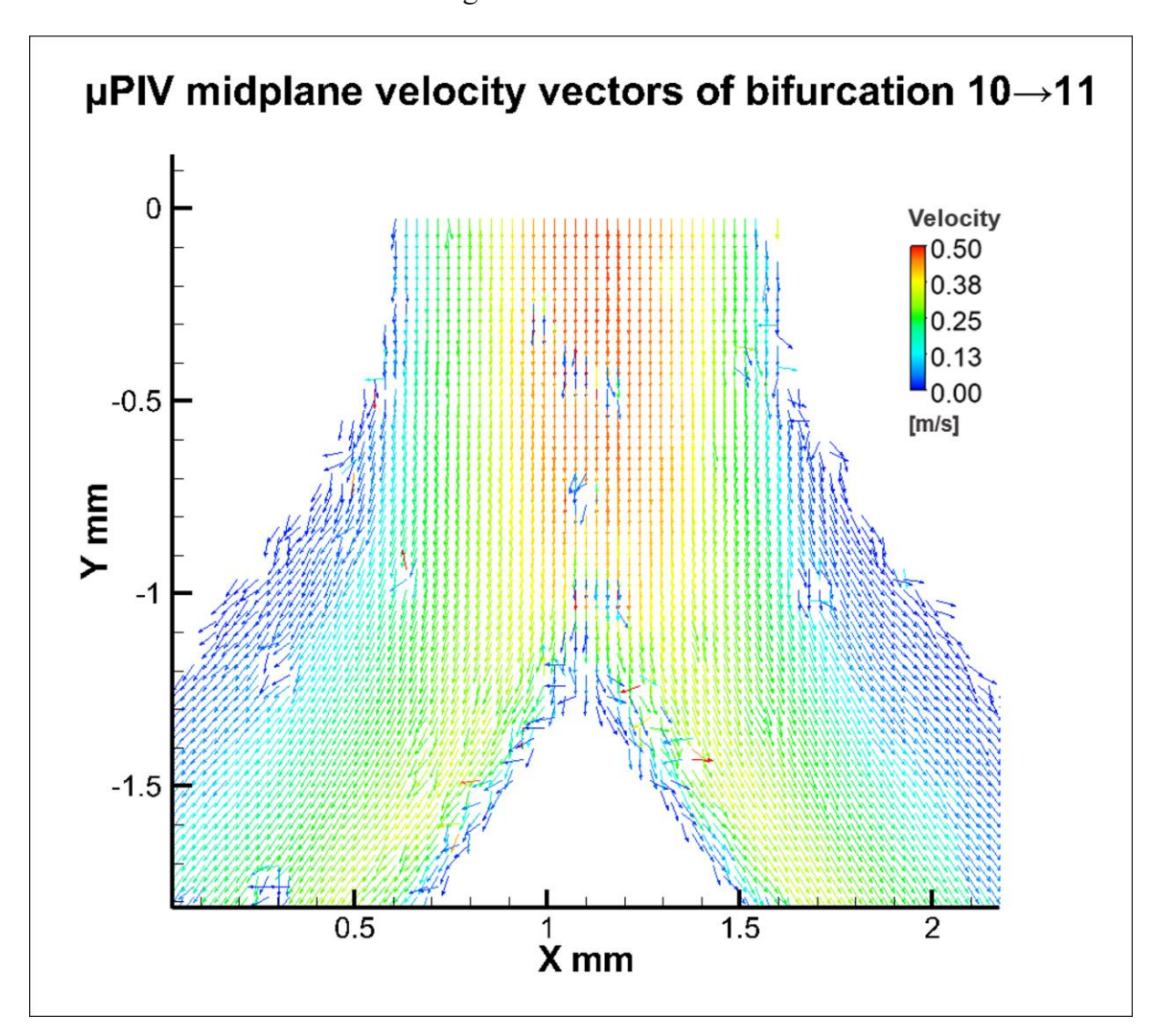


Figure 43: Midplane velocity vector field of splitting generations 10 to 11 resulting from μPIV experiments.

Throughout the entire area of interest, some counterintuitive spots consisting of blue vectors indicating low velocities, as well as and a few red vectors indicating fast velocities are distinguishable. In these spots, the computed velocity field was affected by impurities of the covering microscopy slip or non-removable clots of tracer particles stuck to the bottom of the channel. This debris caused the image processing algorithm to have difficulties calculating a more reasonable solution.

Regarding the microchannel for the bifurcation of generation 15 to 16 (Figure 44), the experimentally obtained information is slightly different, but also presents similarities to the previously discussed bifurcation. Once again, velocities are highest in the middle of the

upper generation, gradually getting lower towards the walls of the duct. Maximum velocities are a bit higher than 0.12 meters per second. However, the flow in the bifurcating area does not split completely evenly.

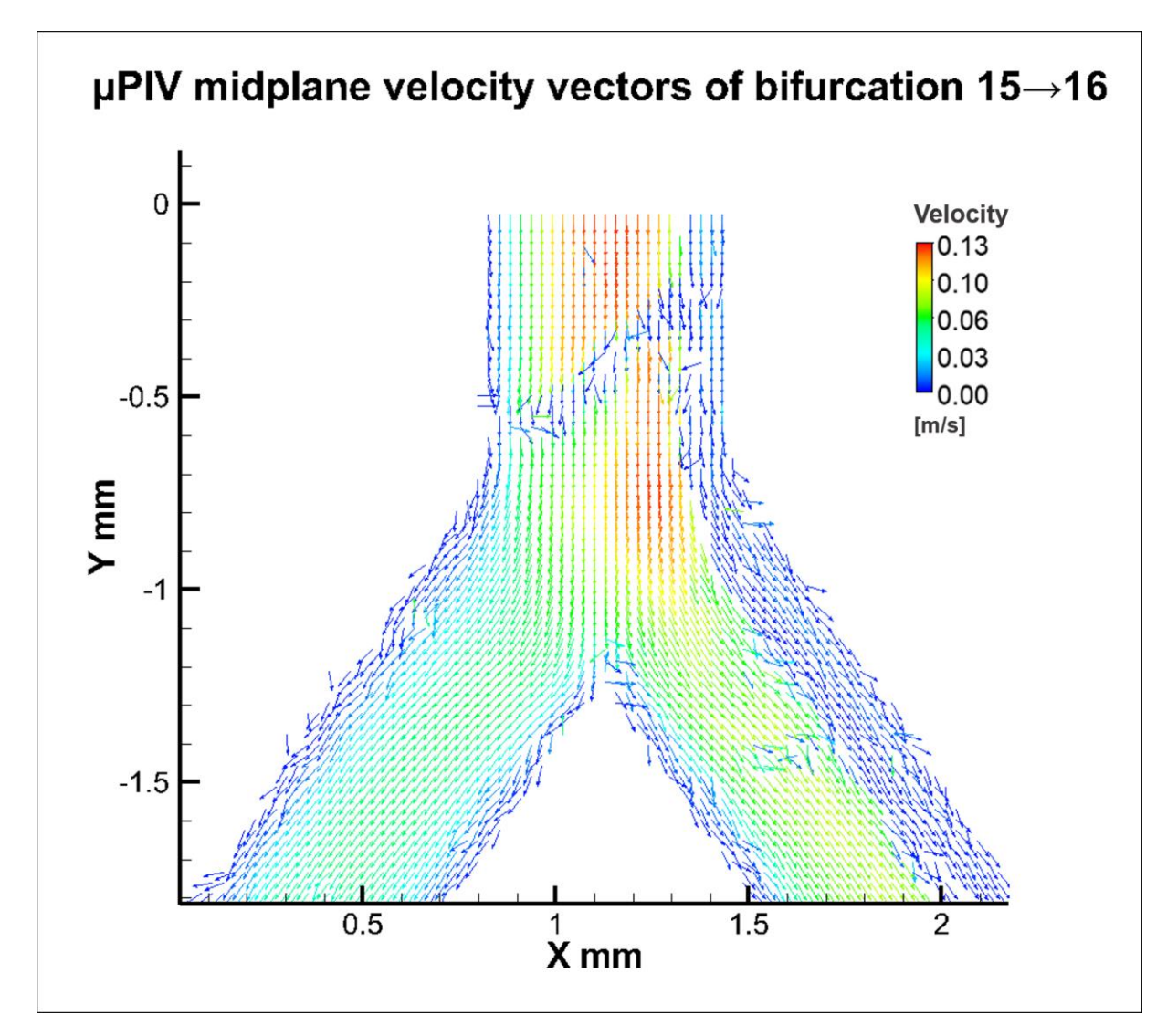


Figure 44: Midplane velocity vector field of splitting generations 15 to 16 resulting from μPIV experiments.

While a clear splitting of the mainstream into two subsequent streams is visible, the velocity vectors pointing towards the right duct maintain their maximal velocity magnitude deeper into the bifurcating region. They also stay at a higher central velocity magnitude of approximately 0.09 meters per second in generation 16. The fluid in the left duct travels slightly slower in the center of the duct at 0.07 meters per second. Also, for the right duct, the band of slow velocity magnitudes towards the outer wall is wider than for the left duct. This might correlate to the fact that fluid moves faster in the right duct.

Another interesting occurrence is the line of blue, non-oriented vectors crossing through generation 15. Here, some kind of fiber, likely coming from a piece of clothing, was stuck between the bottom of the microchannel and the sealing cover glass slip (Figure 45). Unfortunately, this fiber was unidentifiable with the naked eye and could only be seen under the microscope. In this area, reasonable images of tracer particles could not be taken, causing the processing algorithm to produce counterintuitive results. Hence, the resulting line of blue vectors should not be taken as the correct flow field, but rather as a disruptive artefact resulting from manufacturing imperfections of the corresponding channel.

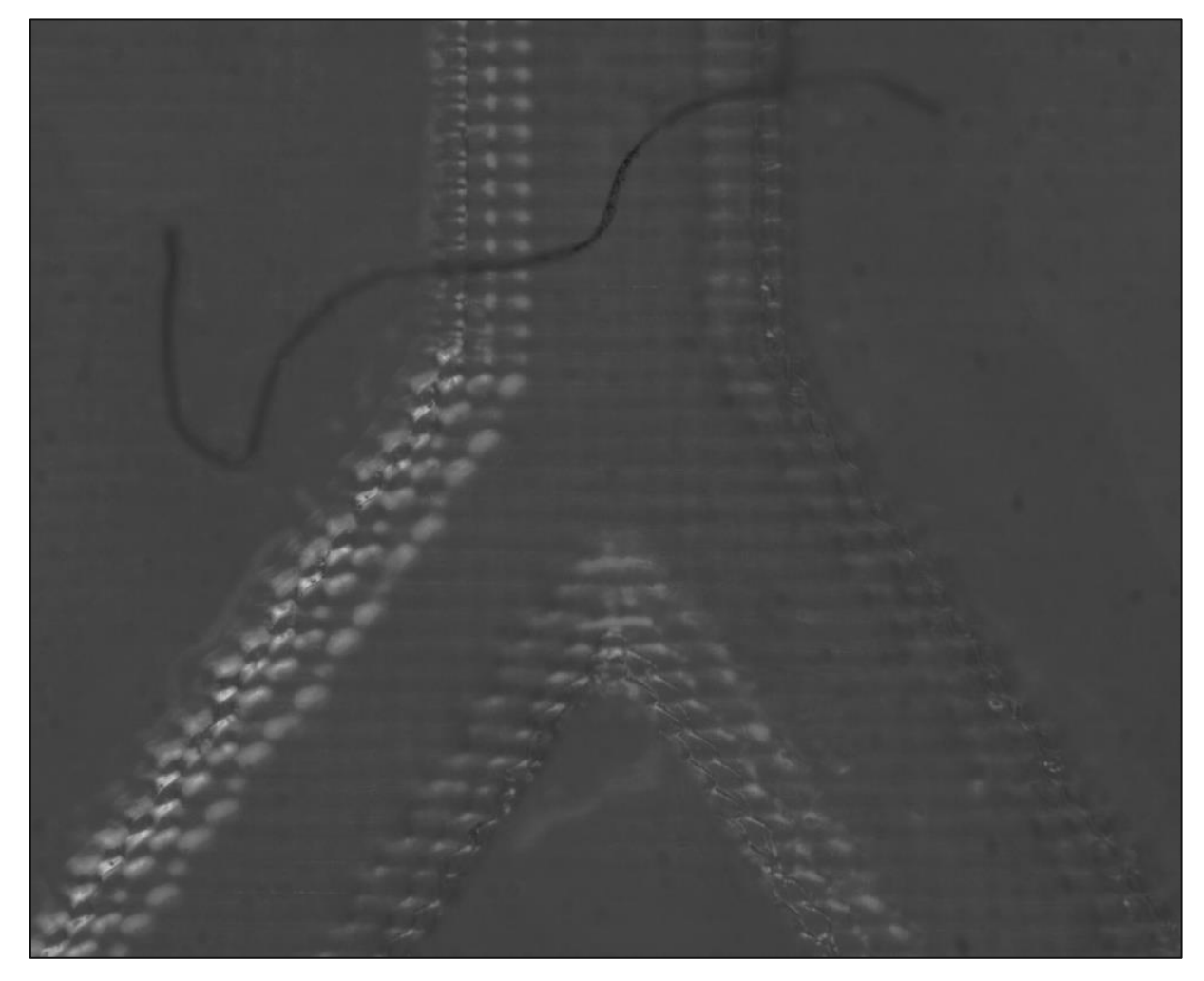


Figure 45: Microscopy image of the bifurcation from generation 15 to 16. An irremovable fiber caught between the printed channel and the cover glass slip obscured the flow field in the respective area.

For the alveolated duct of generation 17 (Figure 46), an overall even distribution of velocity magnitudes presents itself. While in the middle of the duct velocities are highest at around 0.028 meters per second they decrease little by little towards the outside.

On the one hand, vectors inside the duct are nicely aligned, meaning the flow direction is largely uniform. On the other hand, vector directions at the borders of the duct indicate a curved fluid flow into and out of the alveoli on both the right and the left side. The velocity magnitude of these flows is, however, very little.

At the patches of blue vectors in the upper half of the region of interest, particle clots sticking together settled at the bottom of the channel in the same manner as it was already discussed for the bifurcation of generation 10 to 11. This affected the results equivalently in the affected areas.

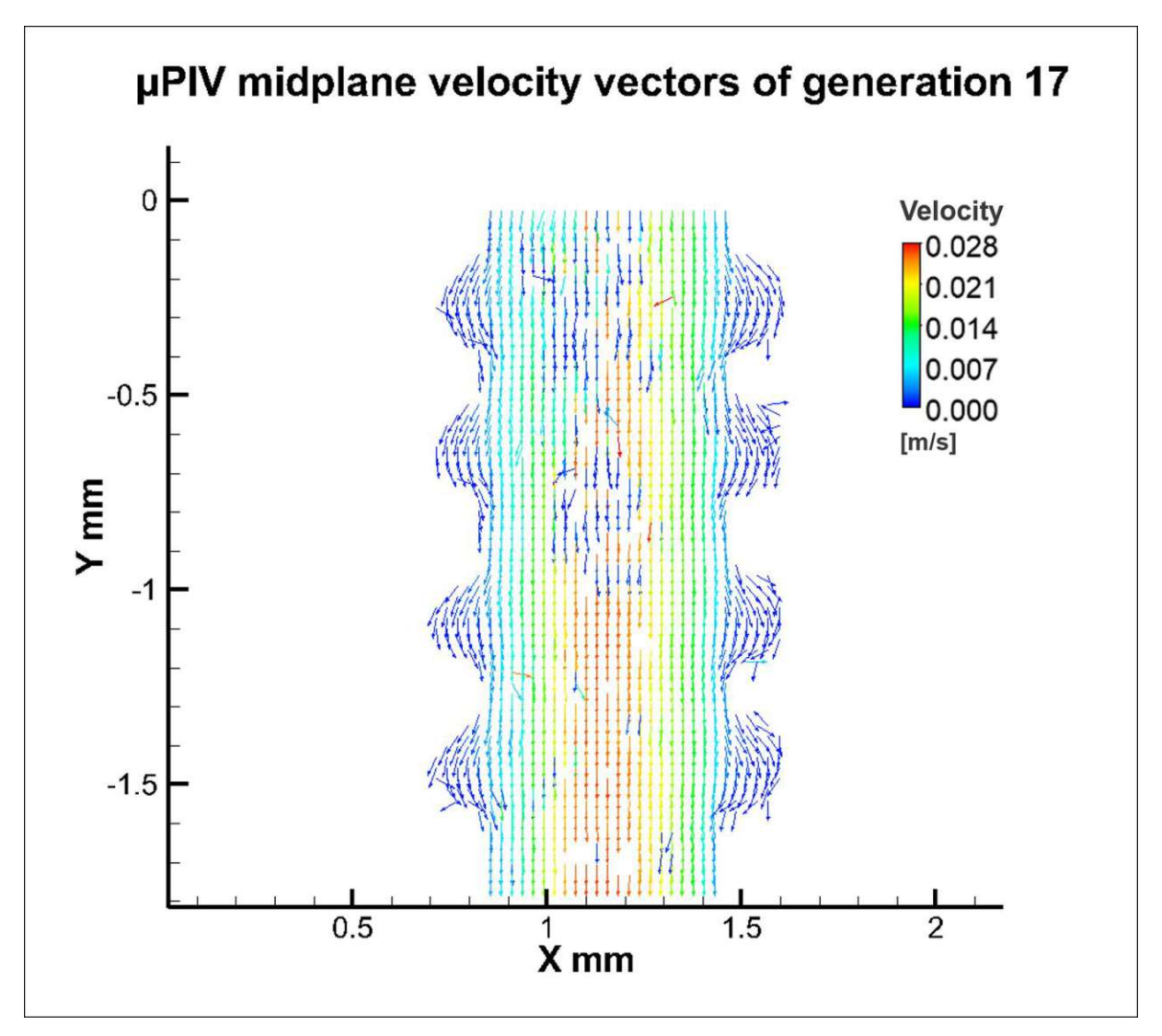


Figure 46: Midplane velocity vector field of an alveolated duct from μPIV experiments.

Altering the region of interest to a closer view of the alveoli (Figure 47), the experimentally determined alveolar flow patterns can be examined in more detail. Measured velocity magnitudes at the opening zone of the alveolus can be determined to be approximately 0.50 millimeters per second. Contrary, close to the alveoli-adjacent duct walls, velocities are still much faster. The deeper the fluid flows in the alveolus, the more the flow magnitude decays until in the most distant regions of the alveolus, air almost stands still.

The aligned vectors curve into the alveolus but also escape it again. This indicates the presence of an area where fluid flows into the alveolus but does not get captured, instead leaving it again. Only the particles escaping into the distant region of the alveolus get trapped. The blue, randomly pointing vectors show the chaotic, slow flow behavior in this capture zone. Here, airflow would be governed by diffusion mechanisms in the lungs, instead of convective transport mechanisms.

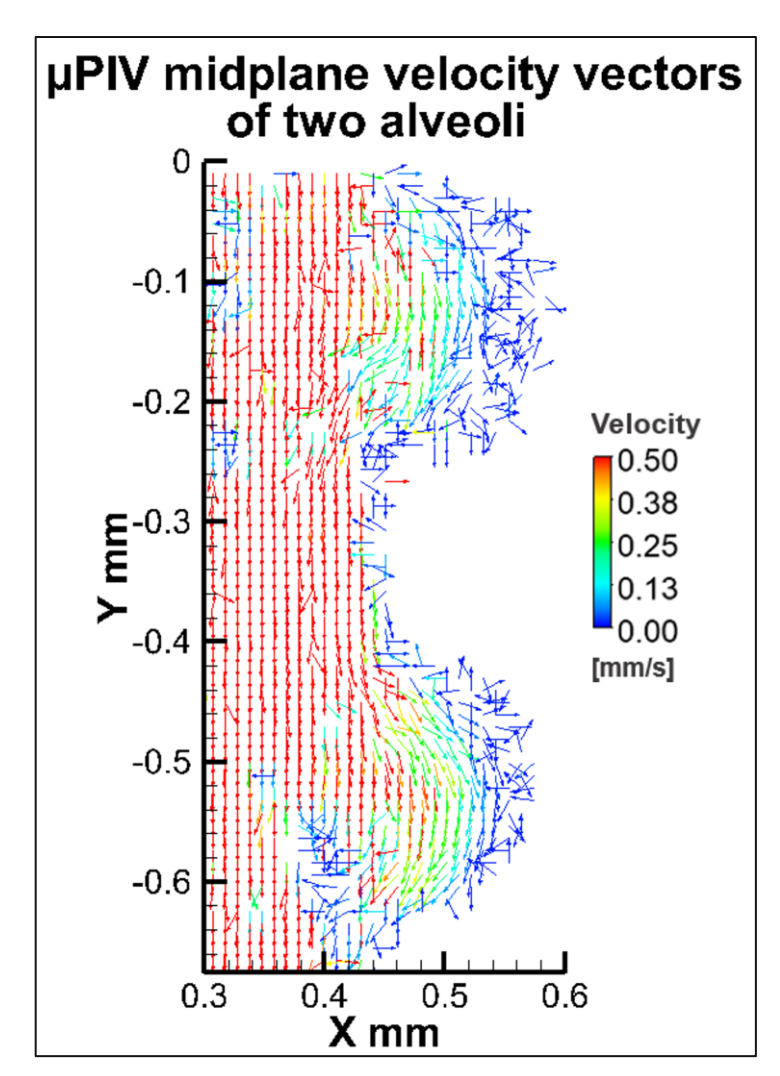


Figure 47: Midplane velocity vector field of two alveoli resulting from μPIV experiments.

In the current experimental investigations, no clear recirculation patterns inside the capture zone of the alveolus could be determined. To observe this phenomenon, more μPIV measurements with varying parameters would definitely be necessary.

As it is easy to detect, experimental results do not perfectly agree with the velocity distributions of simulated results. Two major hinderances concerning almost all trials became obvious during measurements, possibly lowering their accuracy. Firstly, a completely even flow division at the bifurcations was almost never achievable. The reason for this lies in a combination of many small disruptive factors that make real-world measurements much more difficult to implement than simulations. Above all, the presence

of two outlets and small manufacturing differences between the left and right bifurcation resulted in a flow resistance that was always greater in one duct than in the other. Also, factors like gravity, diffusion of particles, or leaks in the microchannels bear the potential to influence the measurements.

Secondly, the time window in which flawless measurements could be taken was very narrow. Already after a few measurement attempts, substantial particle clots and debris depositions obscured certain areas in the defined region of interest.

Nevertheless, these methodological difficulties may be correctable by ruling out potential sources of error like microchannel fabrication, utilized seeding particles, or computational image processing steps. Also, experiments might be performed faster with more experience, resulting in less obscured areas due to stuck particles.

### 4.4 Comparison of simulated and experimental flow patterns

Comparing CFD simulations with µPIV experiments is a powerful approach to validate models, improve their accuracy, and gain valuable insights into complex system phenomena like airflow in the lungs under SHFJV. Through comparisons, simulations and measurements have the possibility to complement each other, thereby enhancing the accuracy and reliability of the overall analysis. The found correlations and discrepancies could be valuable for improved modeling and experimental strategies in the future.

A visual comparison between the midplane velocity fields yielded from all turbulence models and the generated real-world flow fields is given in Figure 48. The first thing that catches the eye is that for all three simulation types employed, the holistic properties of the vector fields are almost identical. Only through a targeted search are minimal differences detectable, which, however, do not play a role in the overall evaluation and hence will not be further discussed. This is different for the comparison between simulations and experiments, where some clear differences are apparent.

For the bifurcation from generation 10 to 11, velocity distributions generally look similar. Vectors with a higher velocity magnitude penetrate deeper into the bifurcation zone for the μPIV results, indicating that airflow is faster than predicted by the models. Also, a flow stall is visible in the experimental findings, which is not distinguishable for the simulations. While the velocity distribution looks alike for generation 10, in generation 11 there are differences. The fastest flow speeds indicated by the yellow vectors are more shifted towards the medial walls

for μPIV. In contrast, they are rather in the center of the ducts for the CFD solutions.

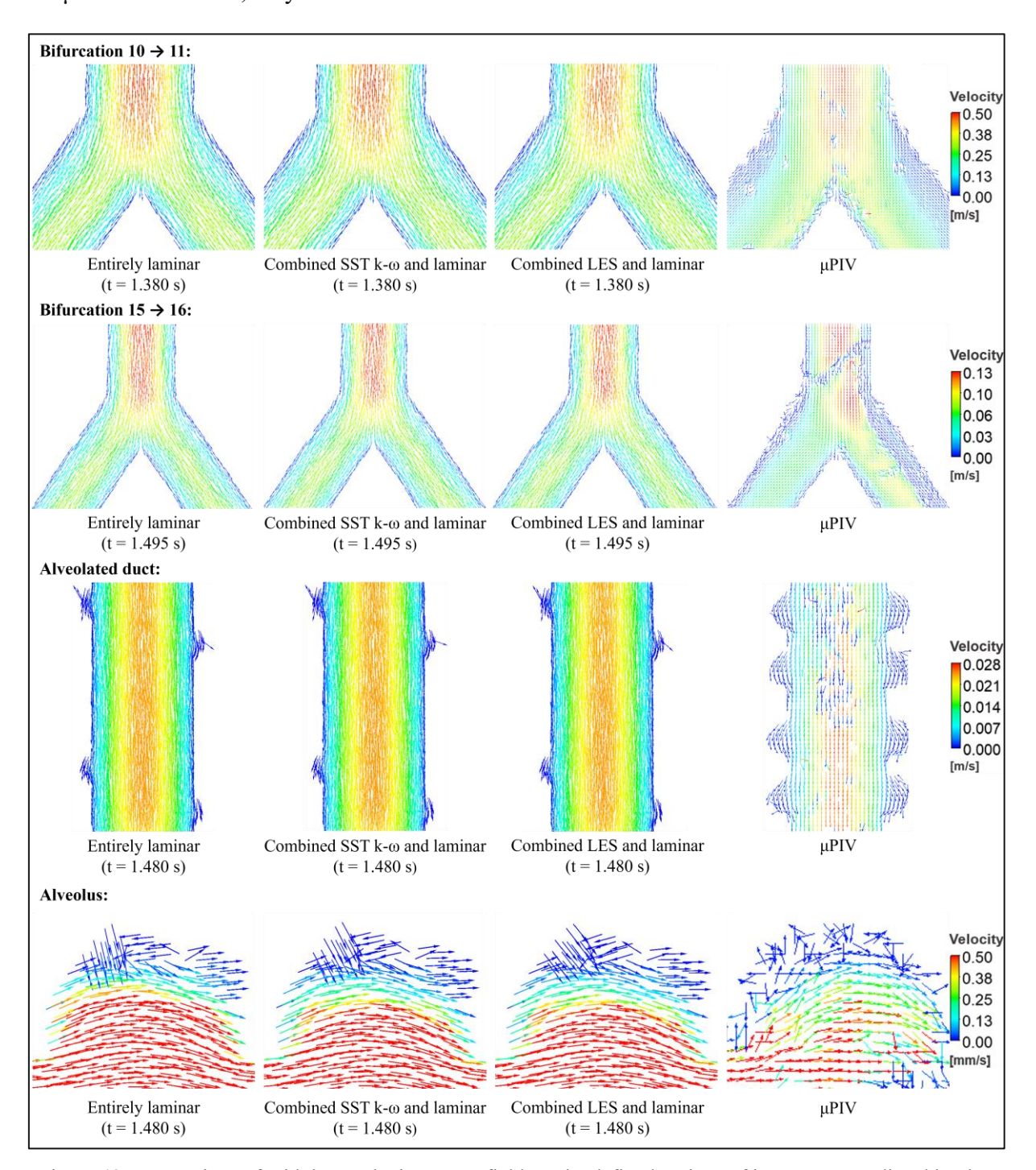


Figure 48: Comparison of midplane velocity vector fields at the defined regions of interest, as predicted by the entirely laminar, combined SST  $k-\omega$  and laminar, and combined LES and laminar simulations, as well as  $\mu$ PIV.

Looking at the bifurcation from generation 15 to 16, results are not as clear as for the previously discussed bifurcation. On the one hand, all CFD simulations agree on the general look of the flow field. On the other hand, the µPIV result deviates to a great extent in some areas. Disregarding the line of blue vectors in generation 15 caused by an obscured view, obvious differences can still be spotted. Mainly, while the vector field seems to be symmetrical for simulations, a faster flow towards the right duct is specified in the experimental findings.

Regarding the alveolated duct, the comparison of results seems more consistent again. For both CFD and µPIV findings, a clear, symmetrical decrease of velocity magnitude from the center of the duct towards the walls is visible. Furthermore, the curving of the lesser velocity vectors near the walls into and out of the alveoli is discernible for both. It is also detectable that the alveolar geometries used for CFD models and µPIV channels are not exactly alike. Instead, it can be observed from the flow field that the amount and diameter of the alveoli has been increased for the µPIV channels.

For the flow field at a single alveolus, similarities and discrepancies can be found once again. Both simulations and results show a correlation between flow depth into the alveolus and decreased flow velocity. The deeper fluid flows into the distant regions of an alveolus, the slower it gets. The µPIV measurement shows the velocity to drop a bit faster. However, this might be because the microchannel alveoli were larger than those employed for the simulations. Looking at vector directions, the homogenous path of the aligned velocity vectors curving into and out of the alveolus is similar. The results only greatly vary for the most distant areas of the alveolus where air is almost standing still. While for the CFD findings, there is still a patch-wise orientation of the field distinguishable, vectors in this area obtained from µPIV experiments are randomly pointing in different directions.

## 5 Conclusion and Outlook

Meaningful results of the simulations and experiments carried out were already presented and discussed in the previous chapter. In the following, those findings are now classified in the overall context in order to answer the defined research questions.

An assessment of the influence of the chosen turbulence model on the airflow in the lungs during SHFJV is given. The feasibility of PIV experiments to gain insight into the airflow behavior in the lungs during SHFJV is summarized. Thoughts on verification and validation of the created model are concluded. Moreover, possible implications of the produced results for the mechanisms of action during SHFJV are deduced. Finally, future perspectives and opportunities for improvement are considered.

#### 5.1 Turbulence model influence on simulated SHFJV

The three turbulence model types under investigation, namely the entirely laminar model, the combined SST  $k-\omega$  and laminar model, and the combined LES and laminar model, were implemented as similar as possible. Boundary conditions and simulation settings were kept consistent across all simulation types to ensure a fair comparison.

Upon analyzing the simulation results qualitatively and quantitatively, it was observed that the laminar, SST  $k-\omega$ , and LES models utilized for the upper airways showed only marginal differences in the predicted airflow patterns and pressure distributions during SHFJV. Consequently, results do not differ crucially for the laminarly governed lower airway branch as well. Despite their differences in turbulence modeling, the computed flow characteristics in the lungs were remarkably consistent across the three applied simulation types.

An explanation on why only minor numerical differences could be detected might be attributed to the fact that the flow turned out to be mostly laminar throughout the entire domain, diminishing the overall effect of turbulence, and accordingly the influence of the chosen turbulence model. Consequently, the added complexity of the SST  $k-\omega$  and LES models did not directly impact the simulation outcomes on the alveoli.

However, it is crucial to note that the observed marginal differences depending on the

chosen turbulence model should not be completely disregarded. Turbulence could be incorporated for the upper airways, for example in the shear layer of flow separations or the mixing zones of two mainstreams during peak exhalation. In these scenarios, energy is definitely dissipated due to turbulence and the laminar airflow patterns are definitely disrupted. These phenomena might also play a role in SHFJV, but just not by contributing directly to the alveolar airflow and the gas exchange.

Concluding, even though all simulation types showed very similar results, it might still be reasonable to incorporate a turbulence model, as nowadays computational limitations are much less of an obstacle than ever before. Without a doubt, there are regions of turbulence at least in the first two airway generations, which may have importance on the effects of SHFJV in a more realistic physiological representation of the lungs. Further investigations would be necessary to deepen the understanding of turbulence modeling in lung CFD simulations.

### 5.2 Feasibility of PIV to study SHFJV

μPIV is a powerful experimental technique widely used to study fluid flow in real-world microfluidic applications. However, its feasibility in investigating SHFJV depends on several critical factors. One of the main problems is that the airflow dynamics occurring in SHFJV can differ strikingly from the steady flow scenarios measurable with the existing μPIV setup at the TU Wien Biofluids Lab. This makes it challenging to produce valuable results applying the standard µPIV techniques directly.

In other words, due to technical limitations, the µPIV setup is currently limited to studying only a steady time frame of the inspiration phase of SHFJV, neglecting the expiration phase or the high-frequency pulsatile flow of the SHFJV cycle. Herby, the challenge lies in capturing the oscillatory nature of SHFJV with conventional µPIV techniques. The current experimental setup only allows for measurements of one steady volume flow, whereas SHFJV involves rapid and variable flow rates. This makes it more difficult to accurately capture the dynamic flow patterns.

Additionally, the prototyping and printing of microchannels suitable for µPIV SHFJV studies required substantial effort, as well as specialized equipment and expertise, making it a resource-intensive endeavor which may not be proportional to the amount of information obtained from the subsequent measurements. Even though a great effort went

into producing the channels, their usability often proved to be suboptimal. In line with the fundamental engineering principle "keep it as simple as possible, but as complicated as necessary" it may have been a reasonable alternative approach to only design the microchannels and outsource their production to external facilities with dedicated capabilities and know-how.

In spite of all these challenges, µPIV offers some promising opportunities for studying SHFJV. Its high spatial resolution enables insights into airflow patterns in the smallest ducts, bifurcations, and even single alveoli. This can possibly provide valuable insights into the complex dynamics of SHFJV effects within the respiratory system. Furthermore, μPIV is non-intrusive and does not significantly disturb the flow dynamics during measurements, allowing accurate and reliable results useable for CFD validation.

Moreover, while not employed in this thesis, 3D PIV techniques have shown promise in capturing the oscillating flow behavior in relevant scientific literature. By extending PIV to a 3D setup, it might be possible to obtain a more complete picture of airflow patterns in the lung during SHFJV. This expansion in measurement capabilities would enable the examination of flow behavior not only in small ducts and alveoli, but also in larger domains like the trachea. Therefore, a more realistic representation of the fluid dynamics might be provided. Summing up, implementing 3D PIV could allow for a more holistic analysis of the flow behavior by providing insights into both the inspiratory and expiratory phases, capturing oscillatory flows, and yielding 3D vector fields. Still, it should not be forgotten that employing 3D PIV demands extensive resources, time, and expertise, thereby significantly expanding the complexity and time investment of experiments and data analysis.

In conclusion, while μPIV experiments can and should be used to validate CFD simulations of SHFJV, the currently available form of µPIV in the TU Wien Biofluids Lab is not sufficient on its own to comprehensively study SHFJV. The experimental setup faces multiple challenges. Nevertheless, with further advancements and adaptations to address these issues, µPIV, and in extension 3D PIV are on a promising way to become suitable techniques for gaining a deeper understanding of SHFJV. The application of PIV in SHFJV research could lead to a better understanding of the interplay between airflow mechanics and lung physiology, which may have implications for respiratory disease treatment strategies in the future.

#### 5.3 Verification and validation of the SHFJV CFD model

The development of CFD models does not only include active design and implementation, but also retrospective verification and validation after all simulations are done. Both terms, verification and validation, stand for the review of a model, but therein consider different aspects [14].

During verification, it is checked whether the implemented CFD model meets the specifications and requirements made when designing the model. In particular, the verification looks for implementation errors and the numerical inaccuracies within the simulations. During validation, it is analyzed whether the CFD model enables a sufficiently accurate representation of the real-life flow phenomena. The validation usually takes place in a comparison of the CFD results with corresponding experimentally determined data [14].

In general, the developed idealized lung CFD model can be verified well. Starting at the grid convergence studies, results show that the mesh is refined enough for the solution to approach a consistent result. This ensures that the results are not overly dependent on the grid and are capturing the essential physics of the problem.

Furthermore, a sensitivity analysis was indirectly conducted by varying turbulence models and comparing them against each other. This helped in identifying that the turbulence simulation type hardly affects the overall properties of the results and speaks for the model's robustness when using different governing equations.

Additionally, investigating the results using physical reasoning, it seems that no inappropriate or unphysiological results were produced anywhere in the representative fluid domain. The occurring orders of magnitude for pressure and velocity results are conceivable as well. This also helps in arguing that the model assumptions result in physical consistency, further verifying the model.

Another step towards verifying the used model would be to check the transient simulations for timestep independency. Running the simulation with different timesteps should not significantly affect the results. While an analysis for timestep independence was not performed in the thesis at hand, the simulation results have still been verified in many other ways.

Regarding the validation of the model, the situation is more demanding. Some areas of the velocity flow fields predicted by the simulations are in good agreement to experimental

results from µPIV measurements, while others show less similarities. Difficulties regarding the experimental setup and measurement techniques, especially the microchannels, make it more difficult to produce the ideal experimental results needed for perfect validation. While this discrepancy is surely noteworthy, it is still true that the experiments at least to some extent but not completely validate the simulations, thereby increasing confidence in the CFD model and its ability to represent real-world fluid flow phenomena.

Concluding, verification of numerical uncertainties through comparison of simulations among themselves and validation through comparison with experimental results both suggest that the generated idealized lung CFD model for SHFJV is capable of producing reasonable predictions. However, one should remember that verification and validation are ongoing processes, and as the model evolves or is applied to new scenarios, it is crucial to keep ensuring integrity and reliability of performed simulations.

## 5.4 Implications for the mechanisms of action during SHFJV

SHFJV is an innovative mechanical ventilation form that combines conventional ventilation with high-frequency, small-amplitude jet ventilation. This approach aims to optimize gas exchange, enhance alveolar recruitment, and improve overall respiratory efficiency in critical patients. To gain a deeper understanding of the mechanisms of action underlying SHFJV, simulations and experiments have been conducted and presented in this thesis. Within the results, many ideas for possible acting mechanisms arise.

Firstly, HFJV causes many rapid cyclic velocity- and pressure changes, whose effects even reach down to the alveoli. While the airflow due to HFJV may not directly contribute to the gas exchange, as it is likely that HFJV only induces dead-space ventilation, the pressure- and velocity changes might still have a mechanical effect on the alveolar walls. A mechanism of action causing changes in structural properties of the alveoli, similar to how material fatigue from dynamic loads changes mechanical properties in conventional engineering materials, is quite possible. Further speaking for this idea, it should be considered that the alveoli were assumed to be rigid and uniform in the thesis at hand, while in reality they are an elastic tissue. Hence, it is conceivable that for collapsed alveoli, like in ARDS, these cyclic, rapid acting changes on the alveolar walls are responsible for the better recruitment during SHFJV due to mechanical influences of the HFJV.

The LFJV on the other hand seems to have its purpose in creating airflows that ventilate

the lungs sufficiently and contribute to gas exchange. Through the superimposing principle, both requirements, slow-acting LFJV for gas exchange and fast-acting HFJV for mechanical influences on the alveoli, are satisfied, providing benefits for both respiration and alveolar recruitment.

Secondly, the subtle turbulences caused by SHFJV in the upper airways may be of importance. While these turbulences are highly unlikely to directly influence the airflow in the alveoli, they are still distinct for SHFJV and do not occur as often in conventional ventilation. It is possible that the turbulences in the upper airways play a role in better mixing of the respiratory gas, which could have long-term effects on the patient. It could already be shown for the idealized lung model, that especially during expiration phases a strong mixing of air coming from different areas occurs. This improved homogenization, happening more frequently in SHFJV compared to classic ventilation techniques, could improve the outcome of ventilating a patient.

Thirdly, another important aspect to be mentioned is the possible appearance of secondary airflows due to SHFJV. The influence of secondary flows on the mechanisms of action is difficult to conclude, as secondary flows are strongly influenced by the patient-specific geometry of the airways and usually do not persist for extended periods of time. Hence, they are difficult to assess in an idealized lung model. However, it should not be completely ruled out that certain secondary flows can develop in the lungs and significantly influence the results of SHFJV.

Additionally, it is essential to note that the conducted studies provide insights into the fluid dynamics during SHFJV, but the conclusions were drawn completely from results stemming from an idealized model and should be further validated with clinical studies and experimentation. To understand the true physiological impacts and mechanisms of action of SHFJV on patients, CFD simulations and µPIV experiments alone are not enough evidence.

### 5.5 Future perspectives and opportunities for improvement

The investigation of SHFJV effects on the lung holds great potential for advancing the understanding of respiratory physiology and creating novel mechanical ventilation possibilities. Therefore, efforts towards researching SHFJV via CFD simulations and PIV experiments should be continued. One key aspect of the performed methods in this project is the substantial amount of generated data from simulations, which can be further utilized for various different types of analyses. Beyond the primary outcomes presented in the current thesis, future research could look into additional properties, such as vorticity, or analyze the investigated variables like pressure distributions, turbulence characteristics, or three-dimensional velocity fields more precisely on different spatial and temporal scales. This may help in gaining deeper insights into the respiratory fluid dynamics of SHFJV.

Another area that offers opportunities for future SHFJV studies is particle tracking in CFD simulations. By tracking particles in the fluid flow, it may be possible to examine potential correlations between fluid dynamics, gas transport, and alveolar gas exchange better. This information could have implications for the mechanisms of action of SHFJV on specific lung regions.

Additionally, improving the geometry of the idealized lung model is a crucial step towards achieving more realistic simulation results. One approach might be to refine the idealized lung model by incorporating more anatomical details. Alternatively, a hybrid approach could be adopted, where computed tomography data is used for a precise representation of the upper airways, and an idealized design constitutes the lower airways. Any form of enhanced representation of the lungs would provide a more accurate basis for CFD and could lead to more realistic results.

What is more to be mentioned is that currently, rigid alveoli represent a limitation, as the mechanical behavior of the alveoli can significantly differ depending on their implementation. To address this problem and give the alveoli elasticity, applying techniques like moving or sliding meshes would be an opportunity for further improvement. This addition would facilitate the effects of lung compliance and better simulate physiological breathing patterns.

Another interesting direction for future SHFJV research lies in comparing healthy lung areas with collapsed ones in the CFD simulations. By simulating lung collapse scenarios, one could gain insights into more potential SHFJV mechanisms of action and assess the effects of this ventilation technique in conditions such as ARDS or other lung injuries even better.

Still, while CFD provides valuable data, experimental validation is needed to confirm the accuracy and reliability of the findings. µPIV experiments have already been employed in the current thesis, with the conclusion that further exploration of this technique seems

promising. More precise and thorough measurements with better microchannels could yield even better results. Also, as aforementioned, the possibility of using 3D PIV could offer a more comprehensive understanding of the real-world flow patterns within the lungs during SHFJV.

In conclusion, the investigation of SHFJV effects on the lung through CFD simulations and µPIV experiments have already delivered compelling results, but also present exciting opportunities for future research. Making use of the abundance of data from simulations, exploring particle tracking, refining the lung geometry, incorporating elastic alveolar walls, as well as comparing healthy and collapsed lung areas could collectively enhance the understanding of SHFJV and its potential as a respiratory therapy. Validating further findings through experimental techniques like µPIV and 3D PIV might also be likely to impact future respiratory research with a focus on SHFJV. These advancements could ultimately lead to improved respiratory treatments and patient outcomes.

## **List of References**

- Tobin, M. and C. Manthous, Mechanical Ventilation. American Journal of Respiratory 1. and Critical Care Medicine, 2017. 196(2): p. 3-4.
- 2. Rezaie-Majd, A., et al., Superimposed high-frequency jet ventilation (SHFJV) for endoscopic laryngotracheal surgery in more than 1500 patients. British Journal of Anesthesia, 2006. **96**(5): p. 650-659.
- 3. Aloy, A. and E. Schragl, Jet-Ventilation. Technische Grundlagen und klinische Anwendungen. 1995, Vienna: Springer Verlag.
- 4. Jiyuan, T., Y. Guan-Heng, and L. Chaoqun, Computational Fluid Dynamics: A Practical Approach. 3 ed. 2018, Oxford: Elsevier Ltd.
- 5. Raffel, M., et al., Particle Image Velocimetry: A Practical Guide. 3 ed. 2018, Berlin: Springer Verlag.
- 6. Lederer, V., Gas flow behaviour in the deep lung under superimposed high-frequency jet ventilation and high frequency oscillation. 2022, TU Wien: Vienna.
- Sznitman, J., et al., Respiratory Flow Phenomena and Gravitational Deposition in a 7. Three-Dimensional Space-Filling Model of the Pulmonary Acinar Tree. Journal of Biomechanical Engineering, 2009. 131(3): p. 1-16.
- 8. Behrends, J.C., et al., Duale Reihe Physiologie. 4 ed. 2021, Stuttgart: Georg Thieme Verlag.
- 9. Weibel, E.R., B. Sapoval, and M. Filoche, Design of peripheral airways for efficient gas exchange. Respiratory Physiology & Neurobiology, 2005. 148: p. 3-21.
- 10. CarlReiner, Product Brochure Jet Laryngoscopes. 2022, CarlReiner GmbH: Vienna.
- 11. CarlReiner, Product Brochure TwinStream. 2022, CarlReiner GmbH: Vienna.
- 12. Guttmann, J., Grundlagen der Lungenmechanik unter Beatmung. Intensivmedizin und Notfallmedizin, 1999. 36: p. 1-8.
- 13. Oczenski, W., Atmen - Atemhilfen. 8 ed. 2008, Stuttgart: Georg Thieme Verlag.
- 14. Schwarze, R., CFD-Modellierung: Grundlagen und Anwendungen bei Strömungsprozessen. 2013, Berlin: Springer Verlag.
- 15. MRCFD, Y+ and Grid Types (https://www.mr-cfd.com/y-and-grid-types/). Last

- accessed 08.06.2023.
- 16. Sharma, A., Introduction to Computational Fluid Dynamics: Development, Application and Analysis. 2022, Cham: Springer Verlag.
- 17. ANSYS, Ansys Fluent User's Guide. 2022, Canonsburg: ANSYS Inc.
- 18. Kajishima, T. and K. Taira, Computational Fluid Dynamics: Incompressible Turbulent Flows. 2017, Cham: Springer Verlag.
- 19. Tsega, E.G., Computational Fluid Dynamics Modeling of Respiratory Airflow in Tracheobronchial Airways of Infant, Child, and Adult. Computational and Mathematical Methods in Medicine, 2018. 2018: p. 1-9.
- 20. Koullapis, P.G., et al., Towards whole-lung simulations of aerosol deposition: A model of the deep lung. Journal of Aerosol Science, 2020. 144: p. 1-17.
- 21. ANSYS, Ansys Fluent Theory Guide. 2022, Canonsburg: ANSYS Inc.
- Launder, B.E. and D.B. Spalding, The numerical computation of turbulent flows. 22. Computer Methods in Applied Mechanics and Engineering, 1974. **3**(2): p. 269-289.
- 23. Wilcox, D.C., Formulation of the k-w Turbulence Model Revisited. AIAA Journal, 2008. **46**(11): p. 2823-2838.
- 24. Wilcox, D.C., Turbulence Modeling for CFD. 3 ed. 2006, La Canada: D C W **Industries**
- 25. Menter, F.R., Two-Equation Eddy-Viscosity Turbulence Models for Engineering Applications. AIAA Journal, 1994. 32(8): p. 1598–1605.
- 26. Phuong, N.L. and I. Kazuhide, Investigation of Flow Pattern in Upper Human Airway including Oral and Nasal Inhalation by PIV and CFD. Building and Environment, 2015. **94**(2): p. Pages 504-515.
- 27. Sul, B., et al., Assessing Airflow Sensitivity to Healthy and Diseased Lung Conditions in a Computational Fluid Dynamics Model Validated In Vitro. Journal of Biomechanical Engineering, 2018. **140**(5): p. 1-14.
- 28. Xu, X., et al., *Investigation of inhalation and exhalation flow pattern in a realistic* human upper airway model by PIV experiments and CFD simulations. Biomechanics and Modeling in Mechanobiology, 2020. 19: p. 1679–1695.
- 29. Gemci, T., et al., CFD Study of Dry Pulmonary Surfactant Aerosols Deposition in Upper 17 Generations of Human Respiratory Tract. Atmosphere, 2022. 2022(13): p. 1-18.

- 30. Wedel, J., et al., Anatomy matters: The role of the subject-specific respiratory tract on aerosol deposition - A CFD study. Computer Methods in Applied Mechanics and Engineering, 2022. 401: p. 1-32.
- 31. Orszag, S.A., et al., Renormalization Group Modeling and Turbulence Simulations. International Conference on Near-Wall Turbulent Flows, 1993.
- 32. Shih, T.H., et al., A New k-ε Eddy-Viscosity Model for High Reynolds Number Turbulent Flows - Model Development and Validation. Computers & Fluids, 1995. **24**(3): p. 227-238.
- 33. Srivastav, V.K., R.P. Akshoy, and J. Anuj, Capturing the wall turbulence in CFD simulation of human respiratory tract. Mathematics and Computers in Simulation, 2019. **160**: p. 22-38.
- 34. Rahman, M.M., et al., Nanoparticle transport and deposition in a heterogeneous human lung airway tree: An efficient one path model for CFD simulations. European Journal of Pharmaceutical Sciences, 2022. 177: p. 1-13.
- 35. Kim, J. and M.P. Ramana, Computational Analysis of Lung and Isolated Airway Bifurcations under Mechanical Ventilation and Normal Breathing. Fluids, 2021. **2021**(6): p. 1-18.
- 36. Wimshurst, A., Large Eddy Simulation (LES): An Introduction (https://www.youtube.com/watch?v=r5vP45 6fB4). Last accessed 08.06.2023.
- 37. Smagorinsky, J., General Circulation Experiments with the Primitive Equations. Monthly Weather Review 1963. 91(3): p. 99-164.
- 38. Nicoud, F. and F. Ducros, Subgrid-Scale Stress Modelling Based on the Square of the Velocity Gradient Tensor. Flow, Turbulence and Combustion, 1999. 62(3): p. 183-200.
- Gemci, T., et al., Computational model of airflow in upper 17 generations of human 39. respiratory tract. Journal of Biomechanics, 2008. 41(9): p. 2047-2054.
- 40. Radhakrishnan, H. and S.C. Kassinos, CFD Modeling of Turbulent Flow and Particle Deposition in Human Lungs. 31st Annual International Conference of the IEEE EMBS, 2009.
- Alzahrany, M., A. Banerjee, and S. G., Flow transport and gas mixing during invasive 41. high frequency oscillatory ventilation. Medical Engineering & Physics, 2014. 36: p. 647-658.

- 42. Calmet, H., et al., Large-scale CFD simulations of the transitional and turbulent regime for the large human airways during rapid inhalation. Computers in Biology and Medicine, 2016. 69: p. 166-180.
- 43. Cui, X., et al., LES study of the respiratory airflow field in a whole-lung airway model considering steady respiration. Journal of the Brazilian Society of Mechanical Sciences and Engineering, 2021. 43: p. 1-17.
- 44. ANSYS, Ansys Meshing User's Guide. 2022, Canonsburg: ANSYS Inc.
- 45. Courant, R., K. Friedrichs, and H. Lewy, Über die partiellen Differenzengleichungen der mathematischen Physik. Mathematische Annalen, 1928. 100(1): p. 32-74.
- Kármán, T., Mechanische Ähnlichkeit und Turbulenz. Nachrichten von der 46. Gesellschaft der Wissenschaften zu Göttingen, Fachgruppe 1 (Mathematik), 1930. 5: p. 58-76.
- 47. Wimshurst, A., What are Wall Functions and How do they work? (https://www.youtube.com/watch?v=fJDYtEGMgzs). Last accessed 09.06.2023.
- 48. Lindken, R., et al., Micro-Particle Image Velocimetry (mPIV): Recent developments, applications, and guidelines. Lab on a Chip, 2009. 2009(17): p. 2551-2567.
- 49. Huber, L., Experimental investigation of the flow in a model of a blood vessel with an inserted flow obstacle. 2023, TU Wien: Vienna.
- 50. Soodt, T., et al., Analysis of basic flow regimes in a human airway model by stereoscanning PIV. Experiments in Fluids, 2013. 54: p. 1-10.
- 51. Ramuzat, A. and M.L. Riethmuller, PIV Investigation of Oscillating Flows within a 3D Lung Multiple Bifurcations Model. 11th International Symposium on Applications of Laser Techniques to Fluid Mechanics, 2002: p. 1-10.
- 52. Vermeulen, M., et al., Flow analysis in patient specific lower airways using PIV. 15th International Symposium on Applications of Laser Techniques to Fluid Mechanics, 2010: p. 1-11.
- Timmerman, B., G. Gibbons, and P. Bryanston-Cross, Study of flows in 53. physiologically realistic patient specific airway models. 10th International Symposium on Particle Image Velocimetry, 2013: p. 1-5.
- 54. Bauer, K., T. Janke, and R. Schwarze, Oxygen transport during liquid ventilation: an in vitro study. Scientific Reports, 2022. 12: p. 1-8.
- Keshavarz-Motamed, Z., et al., Effect of coarctation of the aorta and bicuspid aortic 55.

- valve on flow dynamics and turbulence in the aorta using particle image velocimetry. Experiments in Fluids, 2014. **55**: p. 1-16.
- 56. Lee, W.J., M. Kawahashi, and H. Hirahara, Analysis of Respiratory Flow Dynamics in a Model of Human Terminal Airway Bifurcation using Micro PIV. 6th International Symposium on Particle Image Velocimetry, 2005: p. 1-9.
- 57. Kim, J.K., et al., Experimental Analysis of Oscillatory Airflow in a Bronchiole Model with Stenosis. Journal of Visualization, 2009. 12(2): p. 109-118.
- 58. Bing, H., Fluid Dynamics in Bronchioles of Human Lung. 2016, Saitama University: Saitama.
- Fishler, R., M.K. Mulligan, and J. Sznitman, Acinus-on-a-chip: A microfluidic 59. platform for pulmonary acinar flows. Journal of Biomechanics, 2013. 46(16): p. 2817-2823.
- Tenenbaum-Katan, J., et al., Biomimetics of fetal alveolar flow phenomena using 60. microfluidics. Biomicrofluidics, 2015. 9(1): p. 1-14.
- 61. Fishler, R., et al., Particle dynamics and deposition in true-scale pulmonary acinar models. Scientific Reports, 2015. 5: p. 1-11.
- 62. Lv, H., et al., Microflow in a rhythmically expanding alveolar chip with dynamic similarity. Lab on a Chip, 2020. 2020(12): p. 2394-2402.
- 63. Weibel, E.R., Morphometry of the Human Lung. 1963, Berlin: Springer Verlag.
- 64. Fung, Y.C., A model of the lung structure and its validation. Journal of Applied Physiology, 1988. 64(5): p. 2132-2141.
- Kumar, H., et al., The effects of geometry on airflow in the acinar region of the human 65. lung. Journal of Biomechanics, 2009. 42: p. 1635-1642.
- Yorov, T., Methodology of Micro-PIV Investigation of Blood Flow in Channels with 66. Micro-Structures. 2020, TU Wien: Vienna.
- Insight4G, Insight 4G User's Guide. 2020, Shoreview: TSI Inc. 67.
- 68. Formlabs, The Ultimate Guide to Stereolithography (SLA) 3D Printing. 2017, Berlin: Formlabs GmbH.
- 69. ELEGOO, https://www.elegoo.com/products/elegoo-mars-2-pro-mono-lcd-3d-printer. Last accessed 22.06.2023.
- ELEGOO, https://www.elegoo.com/products/washing-and-curing-station-v2-0. Last 70.

- accessed 22.06.2023.
- 71. Rajasekaran, J., On the flow characteristics behind a backward-facing step and the design of a new axisymmetric model for their study. 2011, University of Toronto: Toronto.
- 72. Pedley, T.J., Pulmonary fluid dynamics. Annual Review of Fluid Mechanics, 1977. 9: p. 229-274.
- 73. Pedley, T.J., R.C. Schroter, and M.F. Sudlow, Flow and pressure drop in systems of repeatedly branching tubes. Journal of Fluid Mechanics, 1971. 46(2): p. 365-383.
- 74. Hyatt, R.E. and R.E. Wilcox, The pressure-flow relationship of the intrathoracic airways in man. Journal of Clinical Investigation, 1973. 42: p. 29-39.

# **List of Figures**

Figure 1: Sketch of human airway system with generations of branching from trachea to
alveoli [9]4
Figure 2: Working principle of the TwinStream ventilation system. SHFJV is performed via
applying the high- and low-frequency jet streams through the jet laryngoscope. By monitoring
gas concentrations and pressure changes, a closed feedback loop is created. Modified after
[11]
Figure 3: Schematic drawing of the jet laryngoscope. Two cannulas for HFJV and LFJV are
integrated apart from each other. A third and fourth cannula (not shown in this figure)
continuously measures pressure and gas concentrations at the tip [2]6
Figure 4: Symbolic pressure curve during SHFJV. Two cycles of LFJV are superimposed
with continuous HFJV [2].
Figure 5: Lung X-ray of a patient with ARDS. Bright areas mark dense tissue or obstructions,
while dark areas indicate cavities. A: Patient receiving conventional ventilation. B: The same
patient after 24 hours of SHFJV. Modified after [3].
Figure 6: Physical model of the respiratory system composed of a cylindrical tube with
resistance $\mathbf{R}$ and an elastic balloon with the compliance $\mathbf{C}$ . Modified after [13]
Figure 7: Schematic drawing of the alveolar pressure response without SHFJV. A pressure
${\it pin}$ is applied to the system from the outside. The static, alveolar pressure ${\it palv}$ lags behind
the changing <b>pin</b> . When no volume flow is present, <b>pin</b> equals <b>palv</b> 9
Figure 8: Graphical representation of the pressure profiles <i>pin</i> and <i>palv</i> for SHFJV.
Although it might look like $pin$ and $palv$ are identical, $palv$ is shifted to the right along the
x-axis by 0.002 seconds, creating a delayed pressure response. In a more detailed view, this
shift is visible
Figure 9: Framework of the three main elements and tasks handled within a CFD analysis [4].
Figure 10: Different types of mesh elements, which can be seamlessly combined to fill up the
fluid flow domain. Modified after [15].
Figure 11: Comparison between differently sized vortices, represented by closed arrow loops.



While those spanning over four or more mesh cells are directly resolved, smaller ones must be
modeled. Modified after [36]
Figure 12: Schematic comparison of turbulence mode types. A: An original flow field, B: Its
RANS model via Reynolds-averaging, C: Its LES model via grid-averaging. Modified after
[14]
Figure 13: The law of the wall. The exact behavior of the dimensionless velocity can be
approximated by a linear function in the viscous sublayer, and a logarithmic function in the
log-law region. Modified after [47]
Figure 14: Schematic representation wall treatment approaches. A: Resolved through multiple
inflation layers, $y + \approx 1$ . B: Modeled through a wall function for a single cell, $y + > 30$ .
Modified after [47]
Figure 15: Illustration of a typical 2D PIV experiment setup [5]25
Figure 16: Flow chart and illustration of the steps involved in tomographic 3D PIV [5]26
Figure 17: Illustration of a typical 2D $\mu$ PIV experiment setup [5]
Figure 18: Different PIV-compatible channels for fluid guidance. A: Sketch of a microchannel
consisting of idealized airway generations 18-21. Modified after [56]. B: Computed
tomography-based silicone model representing airway generations 0-2. Modified after [52].
C: Schematics of a microchannel for researching alveoli. Modified after [61]29
Figure 19: A: Model of a respiratory bronchiole using truncated octahedra. Modified after
[65]. B: Microscopic image showing a cross-section of an alveolar duct. Alveoli (A) can be
seen surrounding the duct (D). Modified after [9]
Figure 20: Overview of the created human lung geometry. A: Complete the upper airways
(red) and single lung branch from the lower airways (blue). B: Generations 17 to 22 with
increasingly alveolated surfaces. C: Detailed view of generation 21 and 22. Small spaces
between the alveoli can be distinguished
Figure 21: Velocity-time graph of the derived inlet velocity profile. The three simulated
regions, "Baseline", "Inhalation", and "Exhalation" are marked with their respective red box.
34
Figure 22: Virtual sections of the airway to compute the average area-weighted velocity
magnitude. A: Sections A-A' to D-D' of the upper airways. The green outflow boundary
marks where the lung parts are theoretically connected. B: Sections E-E' to G-G' of the lower
airway branch. The green inlet boundary marks where the lung parts are theoretically

connected. C: Sections G-G' to I-I' of the lower airway branch. G-G' is given again for better
orientation
Figure 23: Meshing of the upper airways. A: Upper airways cut into separate bodies with
shared topologies, marked by color. B: Section cut through generations 1-3 of the medium-
sized mesh. Prismatic inflation layers near the walls and volume-filling tetrahedral elements
can be distinguished. C: Overview of the coarse mesh. Hexagonal elements filling generation
0 can be seen. D: Overview of the very fine mesh. For lower generations, single elements
cannot be distinguished in this figure
Figure 24: Meshing of the lower airway branch. A: Lower airway branch cut into separate
bodies with shared topologies, marked by color. B: Overview of the medium mesh. For lower
generations, single elements cannot be distinguished in this figure. C: Detailed view of alveoli
of the coarse mesh. D: Detailed view of alveoli of the very fine mesh41
Figure 25: Overview of a typical $\mu PIV$ setup as used in the TU Wien BioFluids Lab46
Figure 26: CAD design of the microchannels. A: Top of a microchannel with applied luer
locks. B: Bottom of the alveolated microchannel. C: Bottom of the microchannel bifurcating
from generation 15 to 16. D: Bottom of the microchannel bifurcating from generation 10 to
1147
Figure 27: ELEGOO Mars 2 Pro printer and Mercury Plus washing and curing station.
Modified after [69, 70]49
Figure 28: Produced parts for experimental μPIV investigations. A: Three plates incorporating
flow channels. Outlines of the microchannels and luer locks glued to the top of the plates can
be seen. B: Bottom of a plate. The red arrow indicates the edge of the cover slip glued to the
bottom of the channel with additional resin
Figure 29: Image processing methodology. Raw images are taken and calibrated. After
preprocessing and masking, the pictures can be algorithmically correlated and processed into
a velocity vector plot
Figure 30: Wall shear stresses of the coarse, medium, fine, and very fine meshes of the upper
and lower airways, resulting from the mesh independence simulations
Figure 31: Average and maximum $y$ +-values of the coarse, medium, fine, and very fine
meshes of the upper airways, resulting from the mesh independence simulations54
Figure 32: Area-averaged velocities of generational sections through the lung geometry,
resulting from the mesh independence simulations. The coarse, medium, fine, and very fine

meshes of the upper and lower airways are compared against each other
Figure 33: The SHFJV cycle, divided into three groups: HFJV cycle, inspiration SHFJV
cycle, and expiration SHFJV cycle. The time points are plotted over the inlet velocity to gain
sense of their position within the complete cycle
Figure 34: Illustrative depiction of flow separation at a backwards facing step. Behind the
edge, the flow separates, creating a shear layer containing vortices, and a recirculation area.
Modified after [71]
Figure 35: Maximal inhalation and exhalation velocities for the upper airways as predicted by
the SST $k$ - $\omega$ simulation. A: Streamline plot during maximal inspiration. Circulating
streamlines with low velocity can be seen. B: 3D assembly of midplane velocity contours
during maximal inspiration. The flow stall at the left and right bifurcation edges is visible. C:
Streamline plot during maximal expiration, indicating the presence of recirculation. D: 3D
assembly of midplane velocity contours during maximal expiration. The flow separation
phenomena can still be distinguished
Figure 36: Midplane velocity contours and vectors of the bifurcation from generation 1 to 2.
The recirculation bubbles are getting carried upwards from generation 2 to generation 1 with
the main expiration stream during HFJV. Flow stalls transforming to higher speed regions
during HFJV expiration are indicated through the red dashed lines. Results taken from the
LES59
Figure 37: Maximal area-averaged velocities at the end of each generation during the
inspiration SHFJV and expiration SHFJV subcycles for all simulation types61
Figure 38: Velocity contours and vectors of an alveolus during the three subcycles of SHFJV.
Results taken from the combined SST $k-\omega$ and laminar simulations
Figure 39: 3D velocity vector plot of a recirculating flow inside an alveolus of generation 17.
Results taken from the entirely laminar simulations
Figure 40: 3D assembly of midplane turbulence kinetic energy and turbulence intensity
contours as representative turbulence quantities. Results taken from the SST $\emph{k-}\omega$ simulation.
A: Turbulence kinetic energy during peak SHFJV inhalation. B: Turbulence kinetic energy
during peak SHFJV exhalation. C: Turbulence intensity during peak SHFJV inhalation. D:
Turbulence intensity during peak SHFJV exhalation
Figure 41: Maximal wall pressure drops occurring in the examined cycles for each employed
turbulence model

Figure 42: Time-dependent pressure-velocity relations during one HFJV subcycle. The
pressure and velocity curves show a phase-shift, causing the oscillating behavior69
Figure 43: Midplane velocity vector fields of splitting generations 10 to 11 resulting from
μPIV experiments
Figure 44: Midplane velocity vector fields of splitting generations 15 to 16 resulting from
μPIV experiments
Figure 45: Microscopy image of the bifurcation from generation 15 to 16. An irremovable
fiber caught between the printed channel and the cover glass slip obscured the flow field in
the respective area
Figure 46: Midplane velocity vector field of an alveolated duct from μPIV experiments74
Figure 47: Midplane velocity vector field of two alveoli resulting from $\mu PIV$ experiments75
Figure 48: Comparison of midplane velocity vector fields at the defined regions of interest, as
predicted by the entirely laminar, combined SST $k$ - $\omega$ and laminar, and combined LES and
laminar simulations, as well as $\mu PIV$ .

# **List of Tables**

Table 1: Time-dependent functions mimicking the pressure profile from the TwinStream jet
ventilator and the according alveolar pressure response
Table 2: Outline of applicable fluid flow models for respiratory CFD simulations20
Table 3: Dimensions, as well as anatomical and physiological equivalents of the human
airway model
Table 4: Numerical mesh quality indicators given by Ansys Meshing and their appointed
meaning [21]
Table 5: Quality indicators of the meshes generated for the mesh independence study of the
upper airways
Table 6: Quality indicators of the meshes generated for the mesh independence study of the
lower airway branch
Table 7: Settings and boundary conditions for the mesh independence studies
Table 8: Settings and boundary conditions for the entirely laminar simulations
Table 9: Settings and boundary conditions for the combined SST $k-\omega$ and laminar
simulations43
Table 10: Settings and boundary conditions for the combined SST $k-\omega$ and laminar
simulations
Table 11: Used channels, their specified regions of interest, as well as chosen settings for the
μPIV measurements
Table 12: Numerical values of tracked flow properties to assess mesh independence53
Table 13: Maximal area-averaged velocities at the end of each generation during inspiration
SHFJV and expiration SHFJV subcycles for all simulation types
Table 14: Maximal wall pressure drops occurring in the examined cycles for each employed
turbulence model
Table 15: Midplane velocity contours and vectors of selected regions during one cycle of
HFJV. Results taken from the entirely laminar "Baseline" simulation
Table 16: Midplane velocity contours and vectors of selected regions during one inspiration
cycle of SHFJV. Results taken from the entirely laminar "Inhalation" simulation

Table 17: Midplane velocity contours and vectors of selected regions during one expiration
cycle of SHFJV. Results taken from the entirely laminar "Exhalation" simulation
Table 18: Midplane velocity contours and vectors of selected regions during one cycle of
HFJV. Results taken from the combined SST $k-\omega$ and laminar "Baseline" simulation 109
Table 19: Midplane velocity contours and vectors of selected regions during one inspiration
cycle of SHFJV. Results taken from the combined SST $k$ - $\omega$ and laminar "Inhalation"
simulation
Table 20: Midplane velocity contours and vectors of selected regions during one expiration
cycle of SHFJV. Results taken from the combined SST $k$ - $\omega$ and laminar "Exhalation"
simulation
Table 21: Midplane velocity contours and vectors of selected regions during one cycle of
HFJV. Results taken from the combined LES and laminar "Baseline" simulation
Table 22: Midplane velocity contours and vectors of selected regions during one inspiration
cycle of SHFJV. Results taken from the combined LES and laminar "Inhalation" simulation.
Table 23: Midplane velocity contours and vectors of selected regions during one expiration
cycle of SHFJV. Results taken from the combined LES and laminar "Exhalation" simulation.
119
Table 24: Wall pressure contours of the upper airways and lower airway branch during
examined subcycles of SHFJV. Results taken from the entirely laminar simulations121
Table 25: Wall pressure contours of the upper airways and lower airway branch during
examined subcycles of SHFJV. Results taken from the combined SST $k$ - $\omega$ and laminar
simulations
Table 26: Wall pressure contours of the upper airways and lower airway branch during
examined subcycles of SHFJV. Results taken from the combined LES and laminar
simulations

# **List of Abbreviations**

2D	Two-Dimensional
3D	Three-Dimensional
ARDS	Acute Respiratory Distress Syndrome
CAD	
CFD	Computational Fluid Dynamics
CFL	
FRW	Flow Rate Weighting
HFJV	High-Frequency Jet Ventilation
LES	Large Eddy Simulation
LFJV	Low-Frequency Jet Ventilation
LRN	Low Reynolds Number
MART	Multiplicative Algebraic Reconstruction Technique
PEEP	Positive End-Expiratory Pressure
PIV	
μPIV	Micro-Scale Particle Image Velocimetry
PISO	Pressure-Implicit with Splitting of Operators
RANS	Reynolds-Averaged Navier-Stokes
RNG	Renormalization Group
SHFJV	Superimposed High-Frequency Jet Ventilation
SIMPLE	Semi-Implicit Method for Pressure-Linked Equations
SLA	Stereolithography
SST	
WALE	Wall Adapting Local Eddy Viscosity

## **List of Symbols**

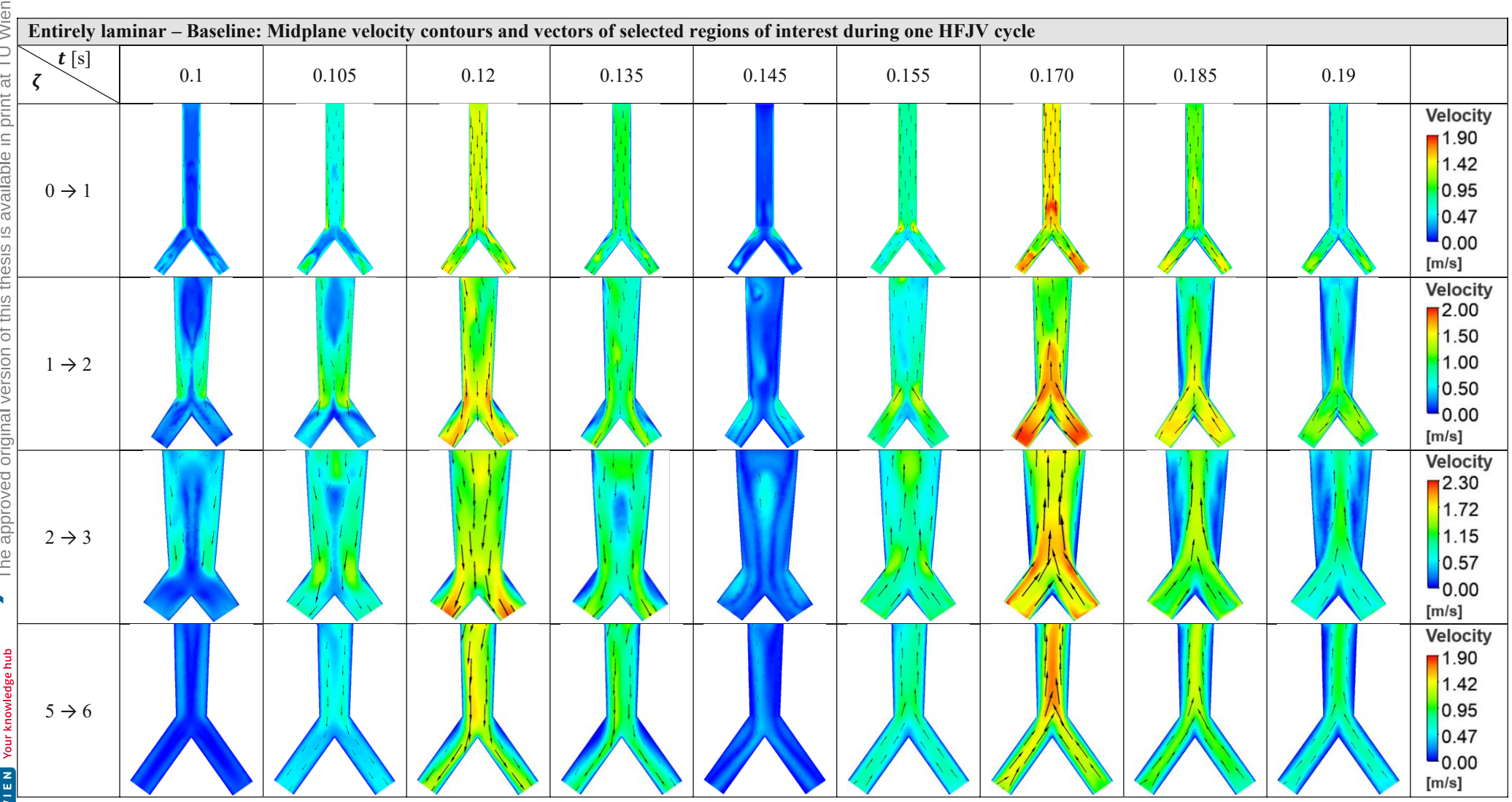
cCourant number	C
c <sub>max</sub> maximal Courant number	c
C compliance	C
identity tensor	
kturbulent kinetic energy	k
Lcharacteristic linear dimension	L
p <sub>alv</sub> alveolar pressure	p
p <sub>in</sub> incoming pressure	p
p <sub>res</sub> resistive pressure	p
$P_k$ production of turbulent kinetic energy	P
<b>R</b> resistance	R
<b>Re</b> Reynolds number	R
sdisplacement vector	<u>s</u>
S modulus of mean strain-rate tensor	
ttime	t
<u>u</u> flow velocity vector	u
u <sup>+</sup> dimensionless velocity	u
u, v, w cartesian flow velocity components	u
Vvolume	V
volume flow	Ù
x, y, z cartesian coordinates	x
y <sup>+</sup> dimensionless wall-distance	y
$\mathcal{C}_{1\varepsilon},\mathcal{C}_{2\varepsilon},\mathcal{C}_{\mu},\sigma_{k},\sigma_{\varepsilon}$	C

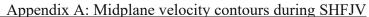
<u><u>t</u></u>	Reynolds stress tensor
ε	dissipation of turbulence
ζ	lung branching generation
μ	dynamic viscosity
$\mu_t$	turbulent eddy viscosity
ρ	density
ω	. specific dissipation of turbulence

..... empirical constants for the standard  $k-\varepsilon$  model  $\sigma_k, \sigma_\omega, \beta^*, \beta, \gamma$  ..... empirical constants for the standard k- $\omega$  model  $\alpha, F_1, F_2$ ...... constants and blending functions for the SST k- $\omega$  model κ, B.....empirical constants for the law of the wall



# Appendix A: Midplane velocity contours during SHFJV





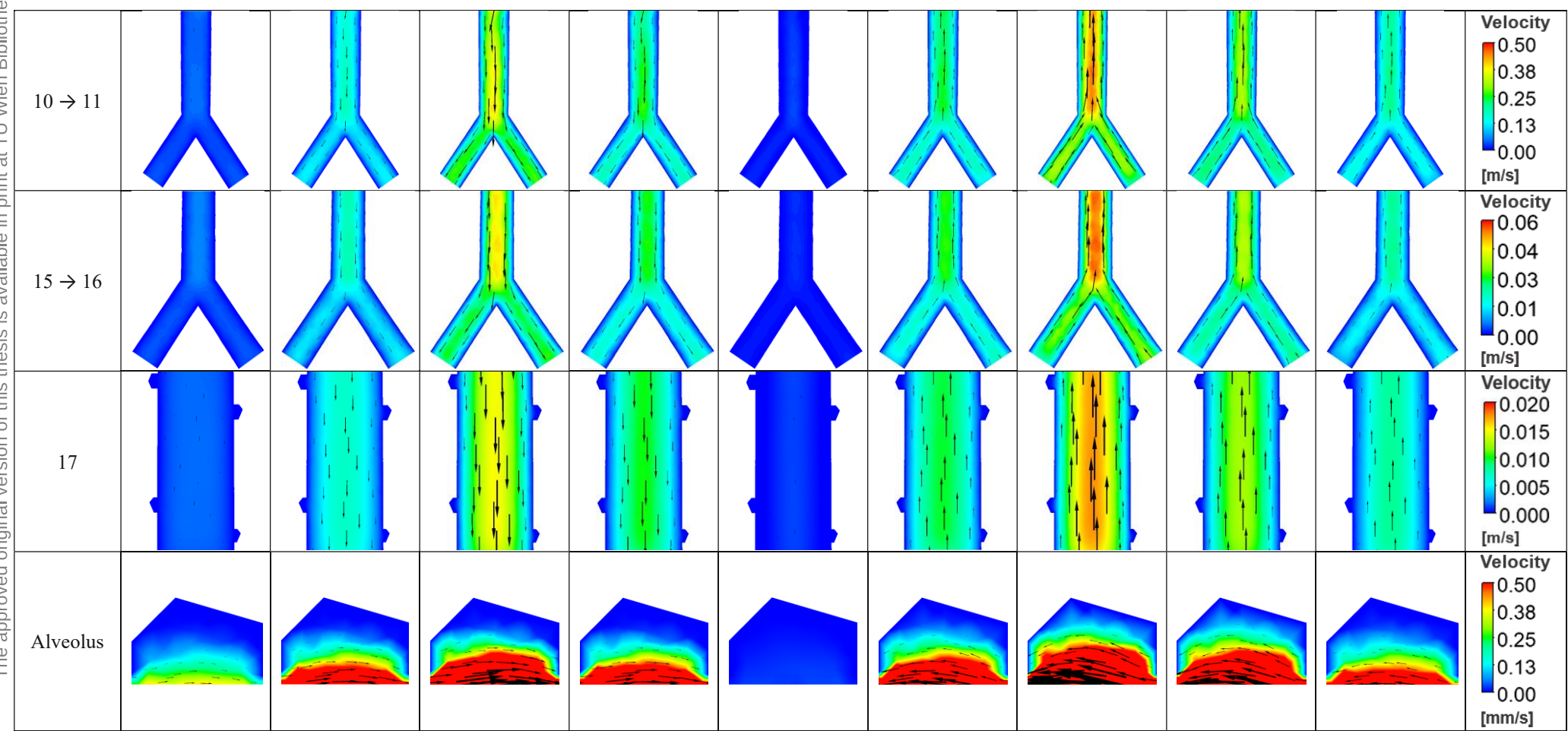
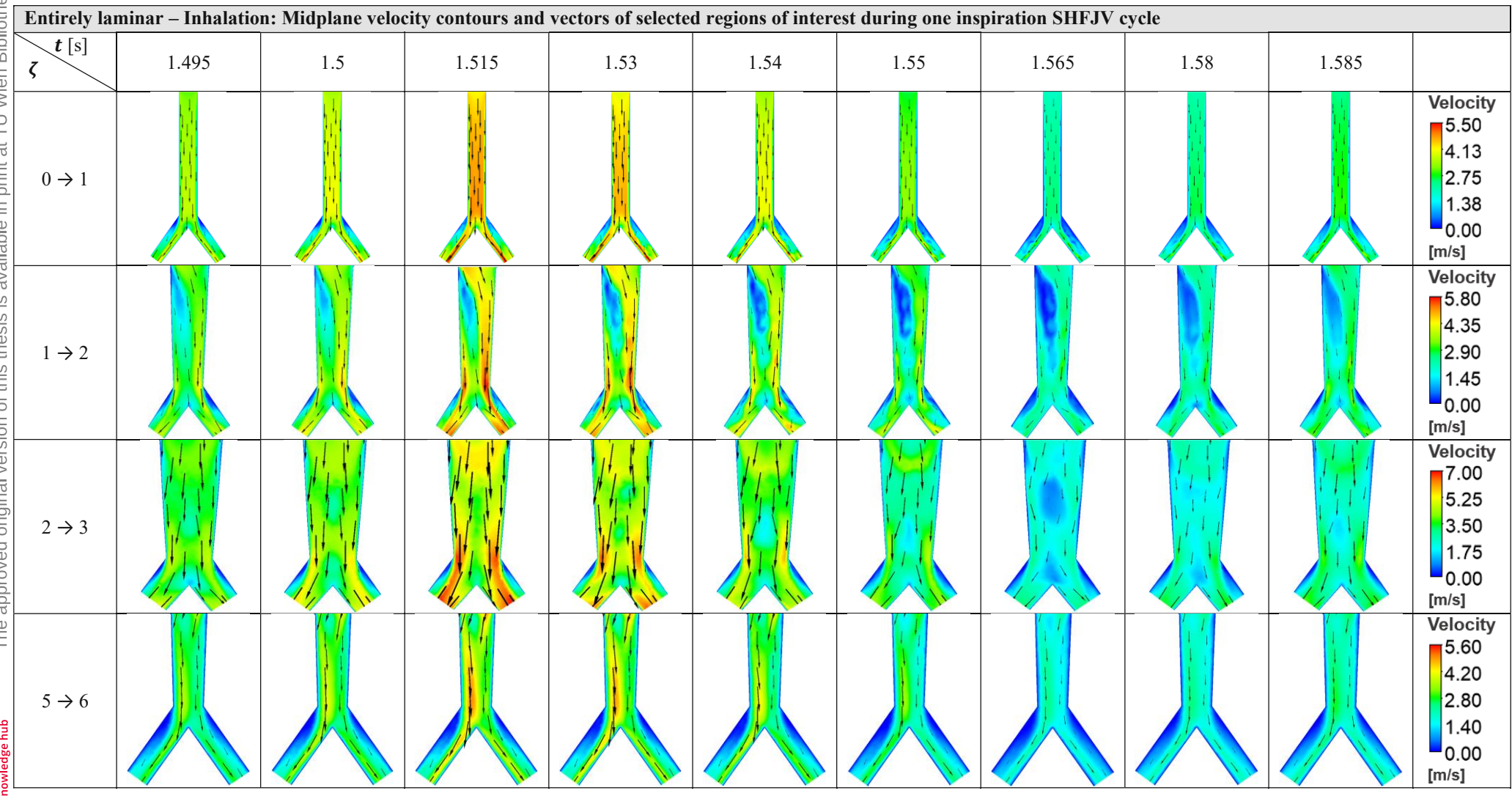


Table 15: Midplane velocity contours and vectors of selected regions during one cycle of HFJV. Results taken from the entirely laminar "Baseline" simulation.

Appendix A: Midplane velocity contours during SHFJV





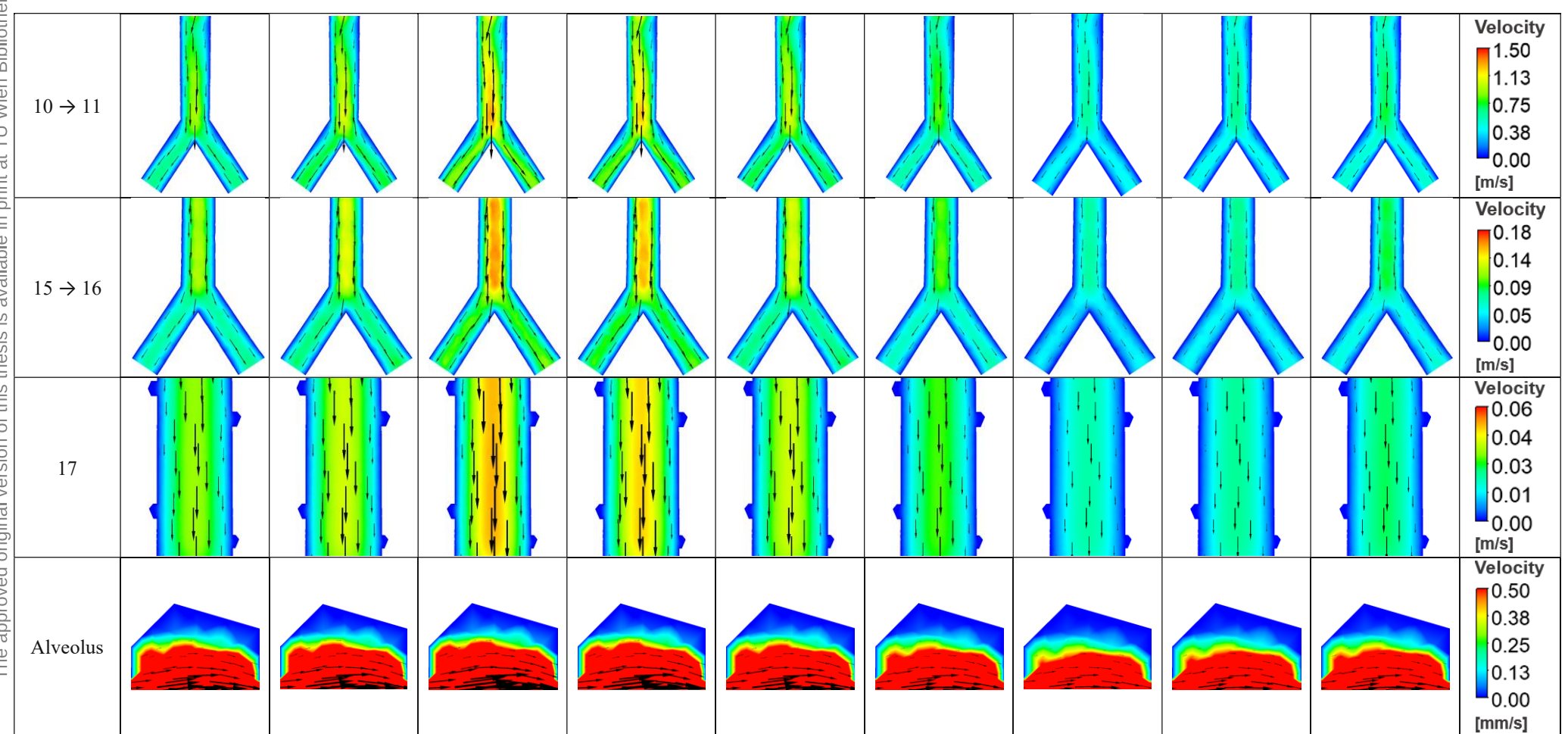
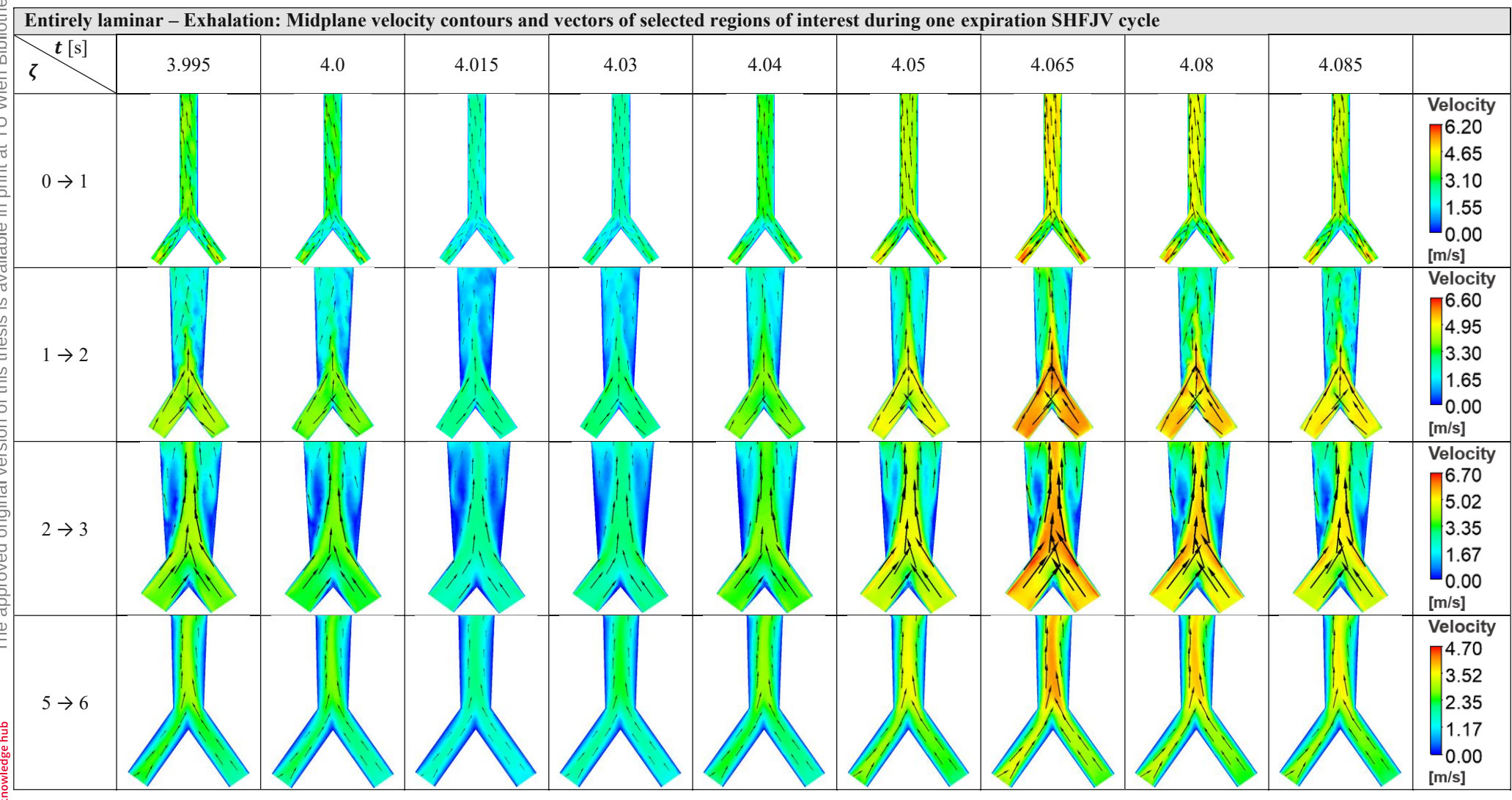
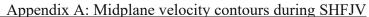


Table 16: Midplane velocity contours and vectors of selected regions during one inspiration cycle of SHFJV. Results taken from the entirely laminar "Inhalation" simulation.

Appendix A: Midplane velocity contours during SHFJV





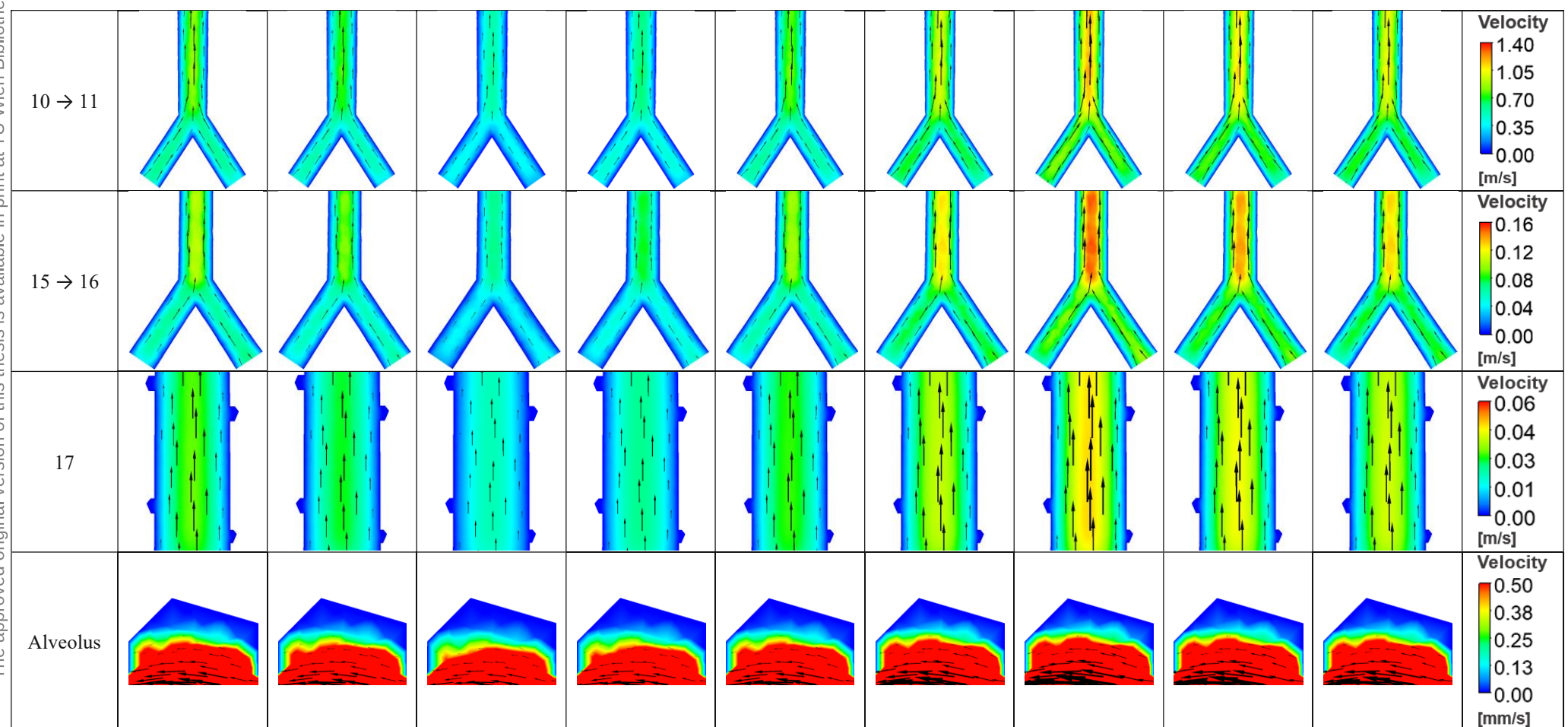
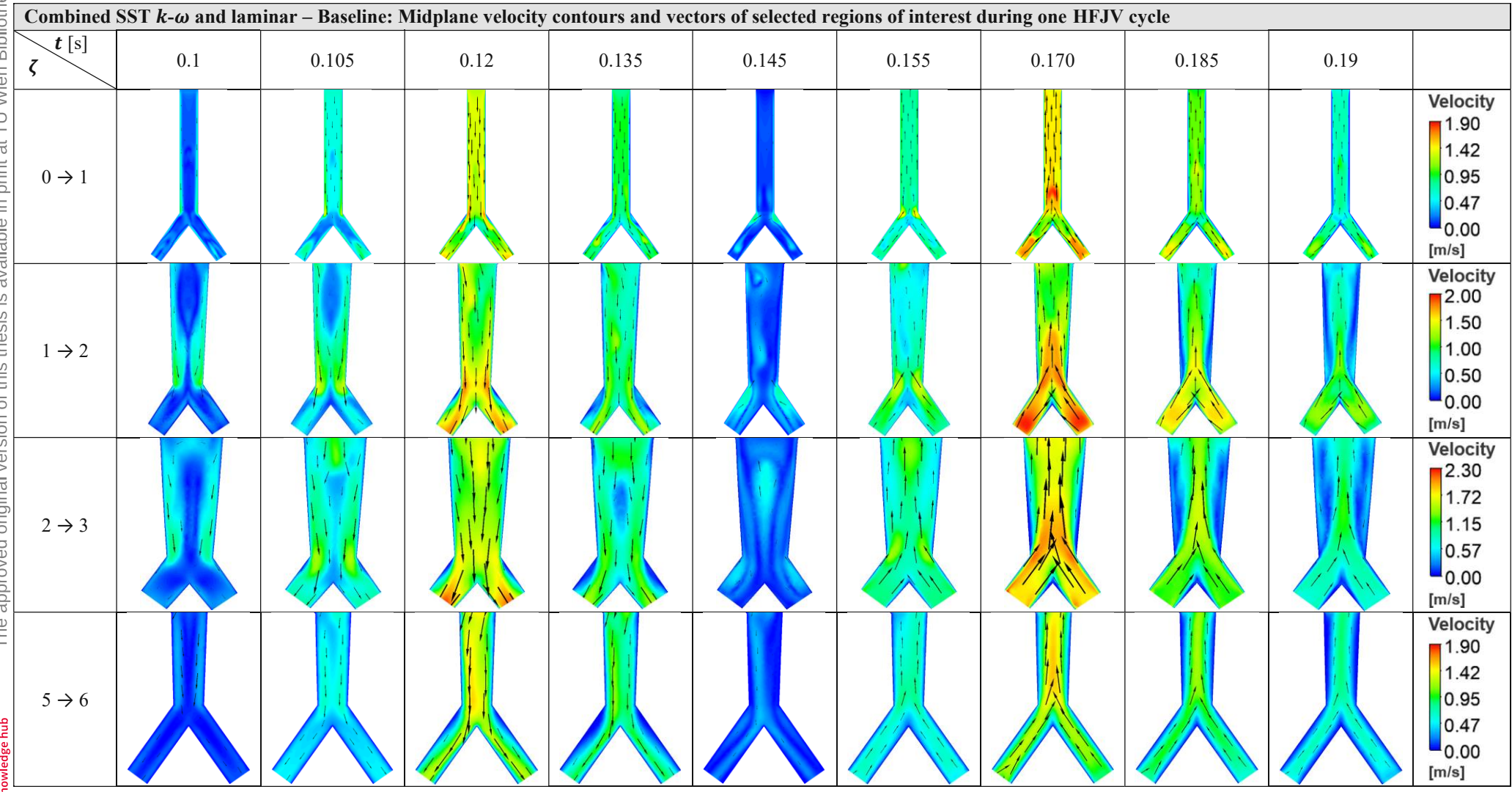


Table 17: Midplane velocity contours and vectors of selected regions during one expiration cycle of SHFJV. Results taken from the entirely laminar "Exhalation" simulation.

Appendix A: Midplane velocity contours during SHFJV



## Appendix A: Midplane velocity contours during SHFJV

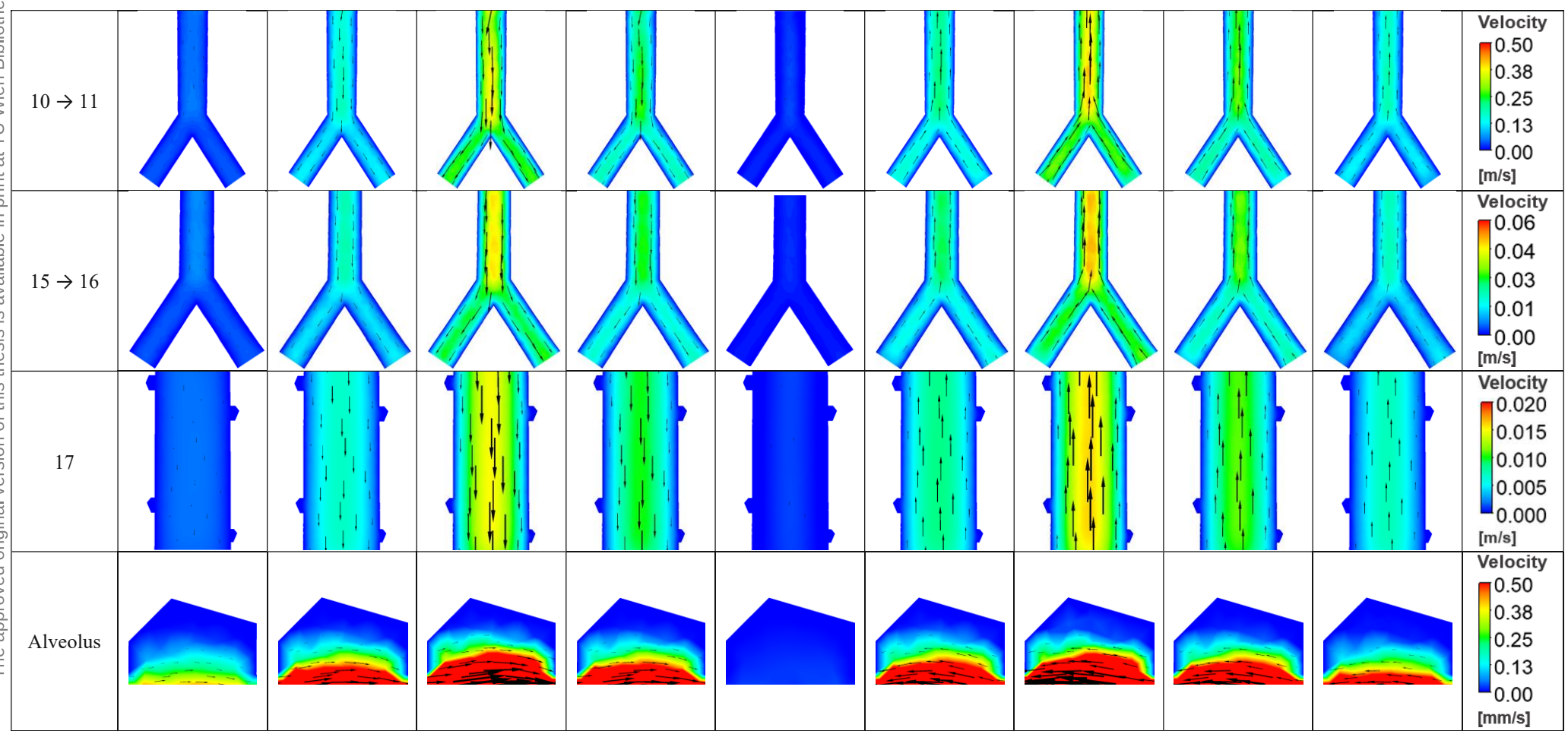
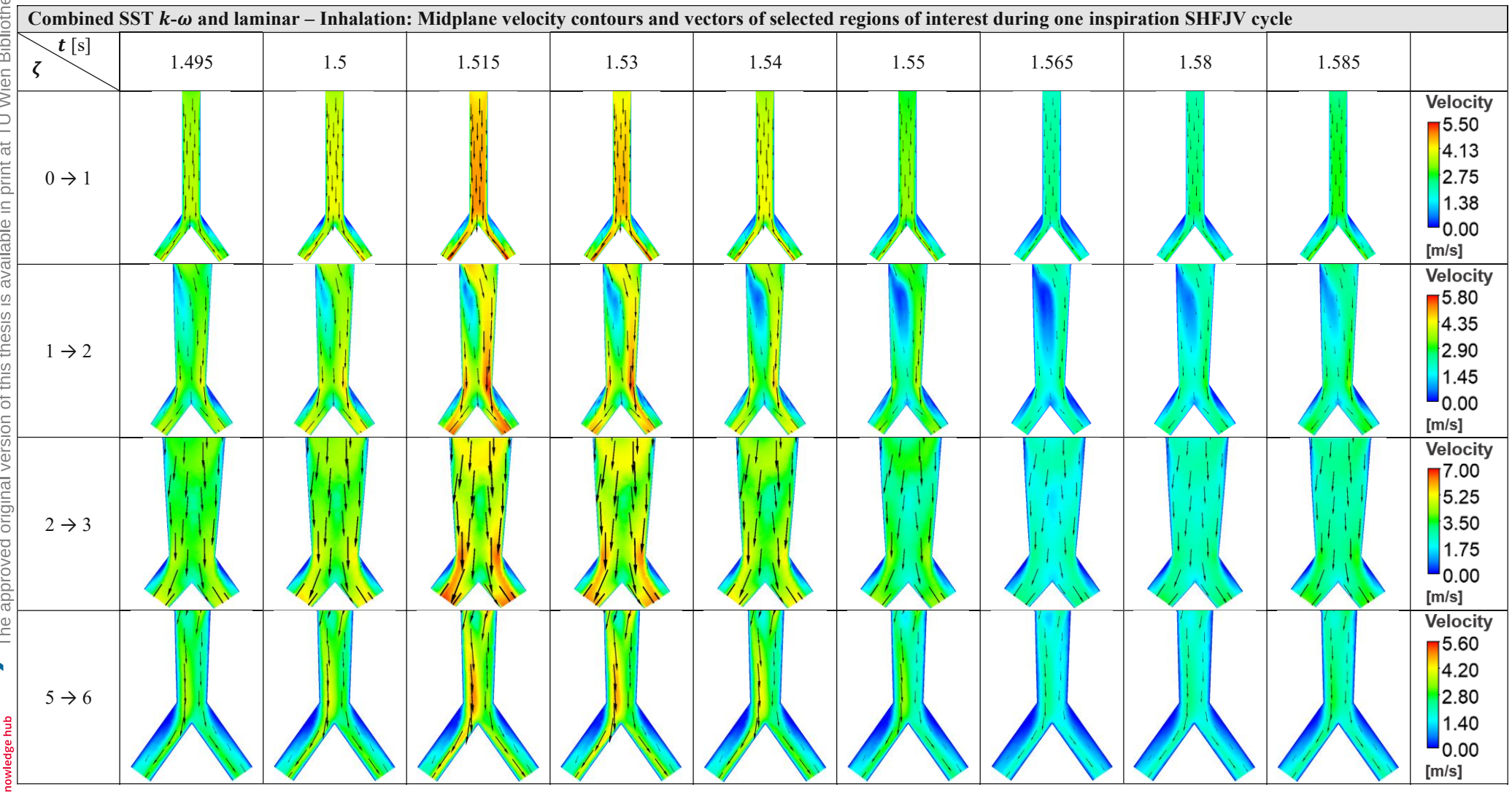
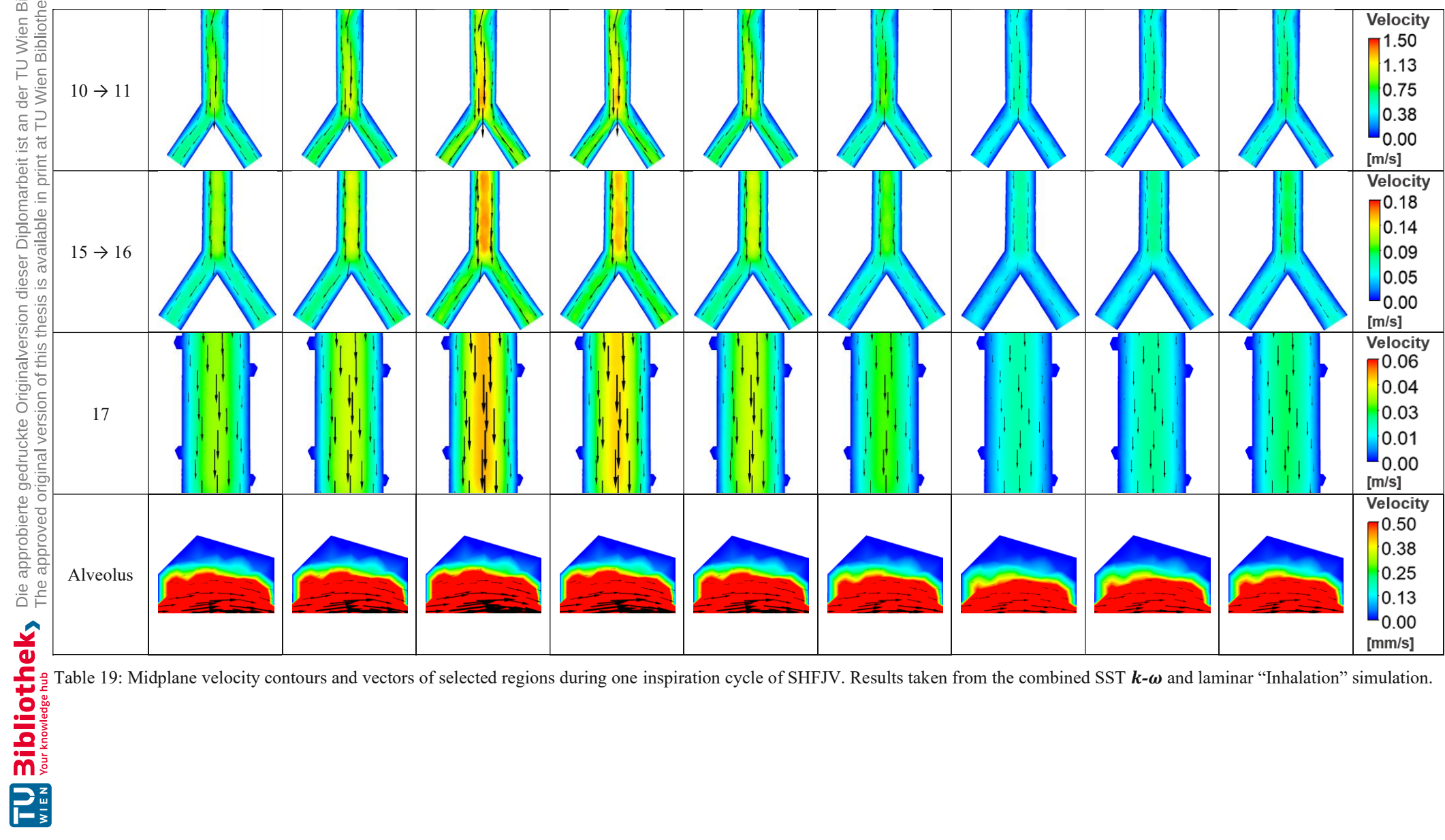


Table 18: Midplane velocity contours and vectors of selected regions during one cycle of HFJV. Results taken from the combined SST *k*-ω and laminar "Baseline" simulation.

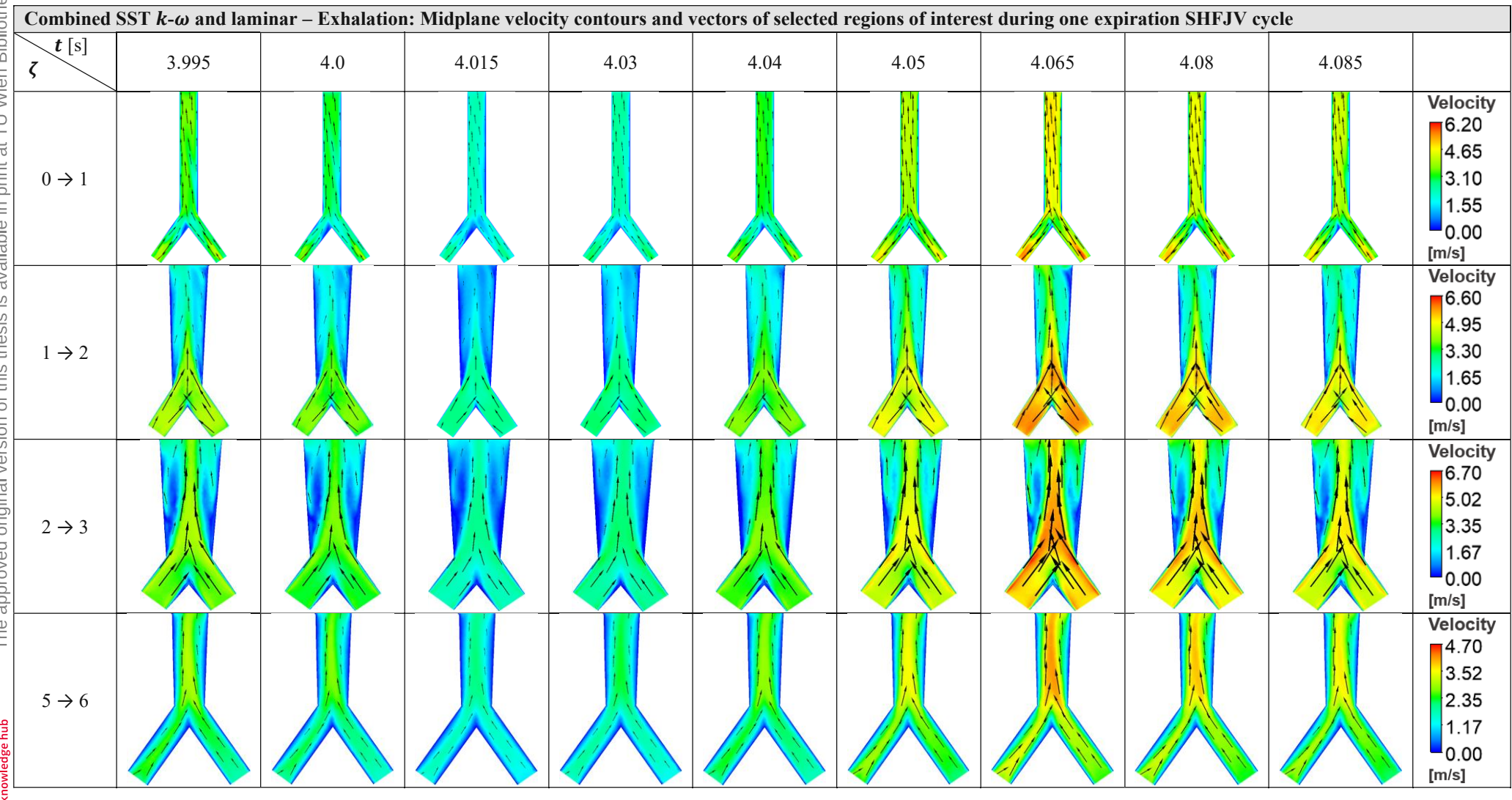
Appendix A: Midplane velocity contours during SHFJV



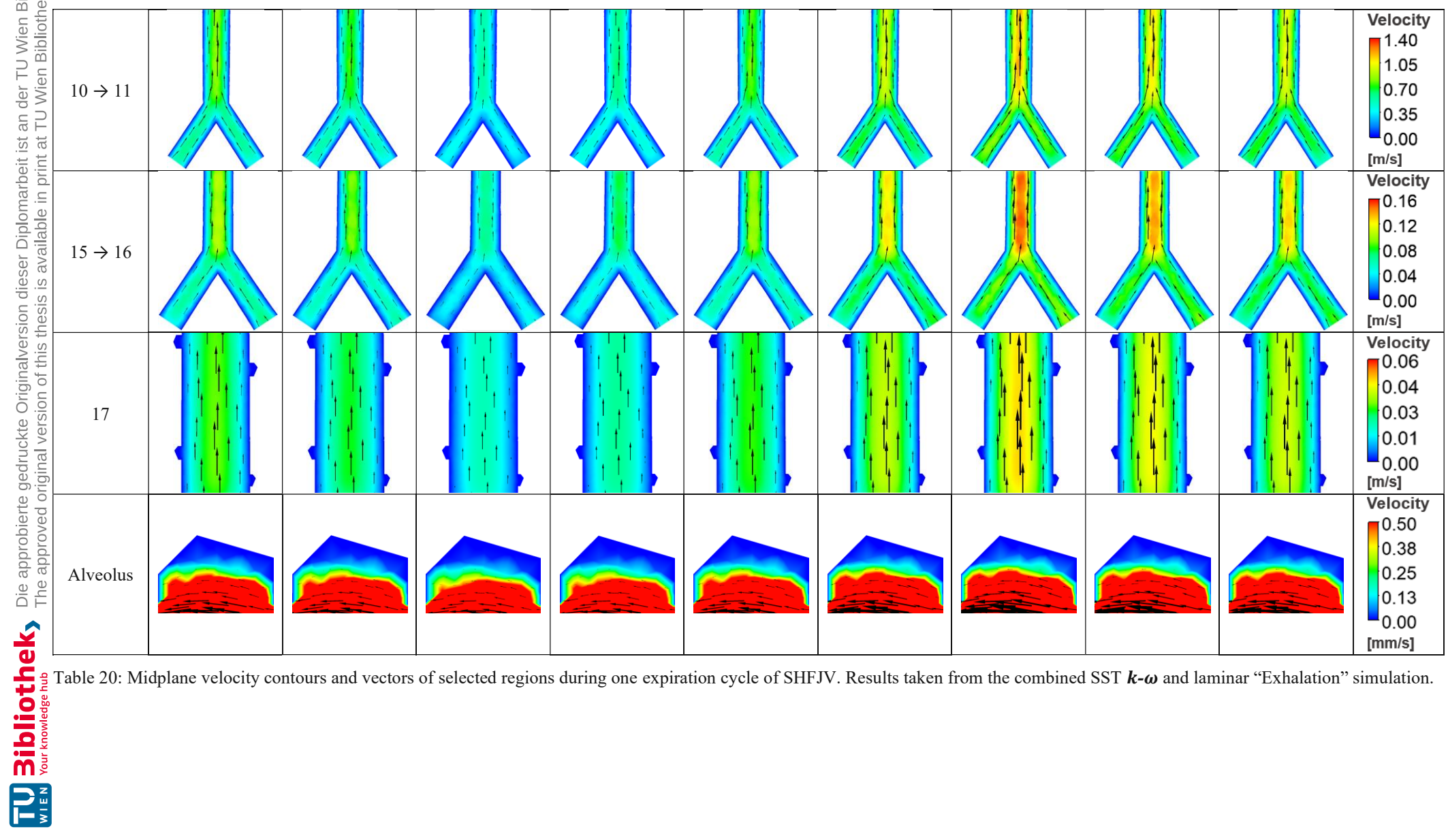




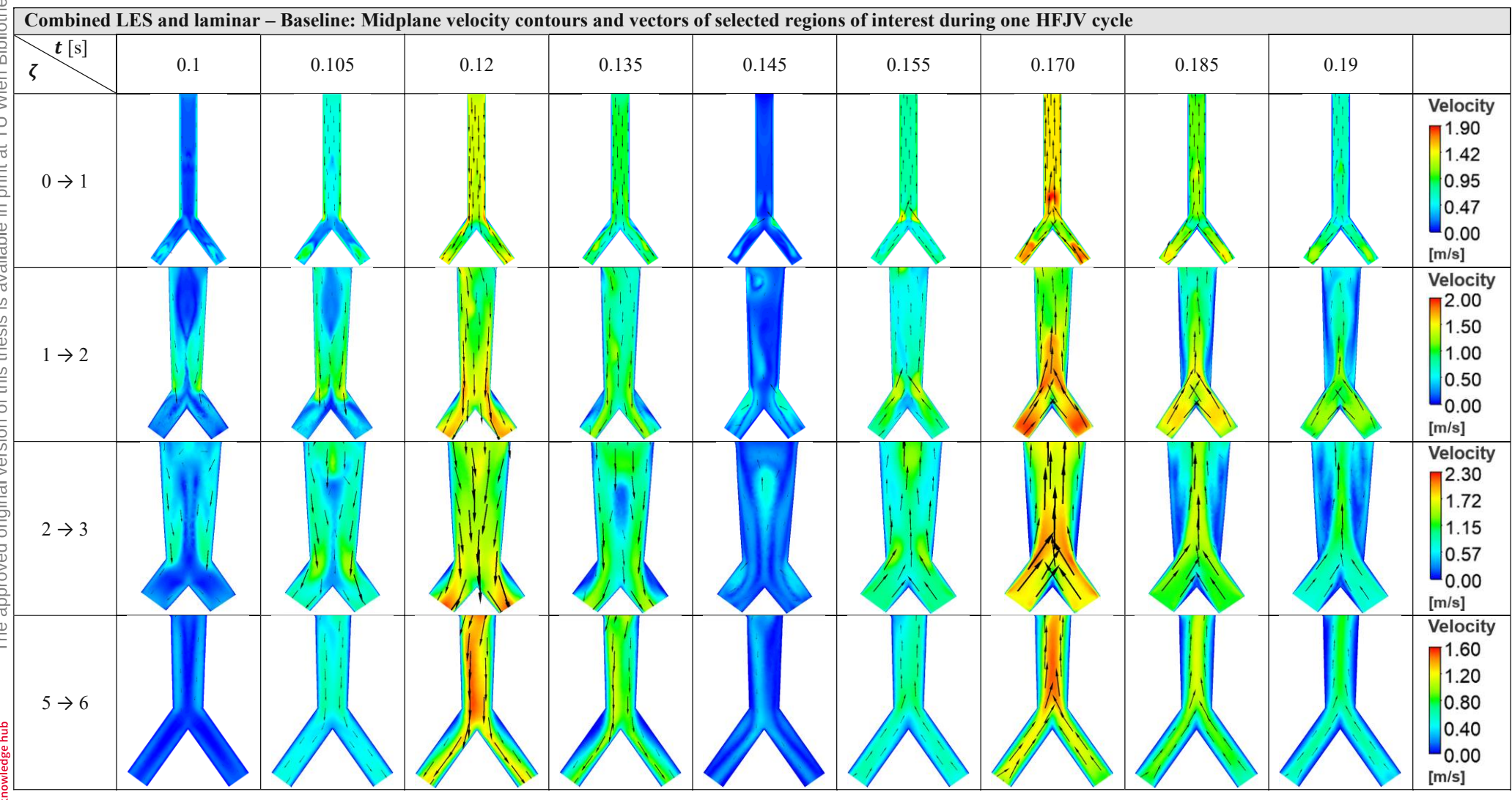
Appendix A: Midplane velocity contours during SHFJV

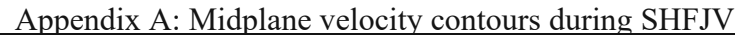


## Appendix A: Midplane velocity contours during SHFJV



Appendix A: Midplane velocity contours during SHFJV





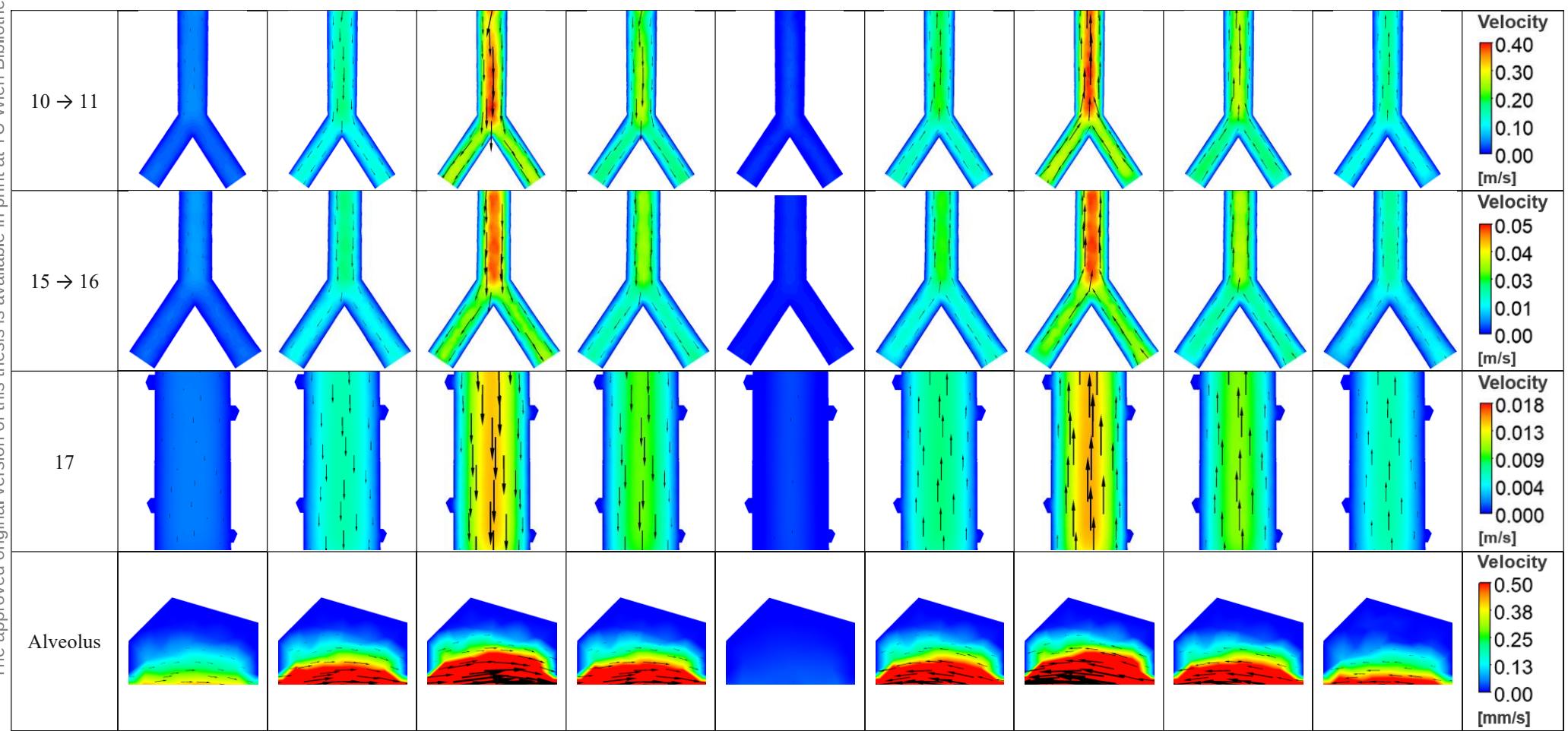
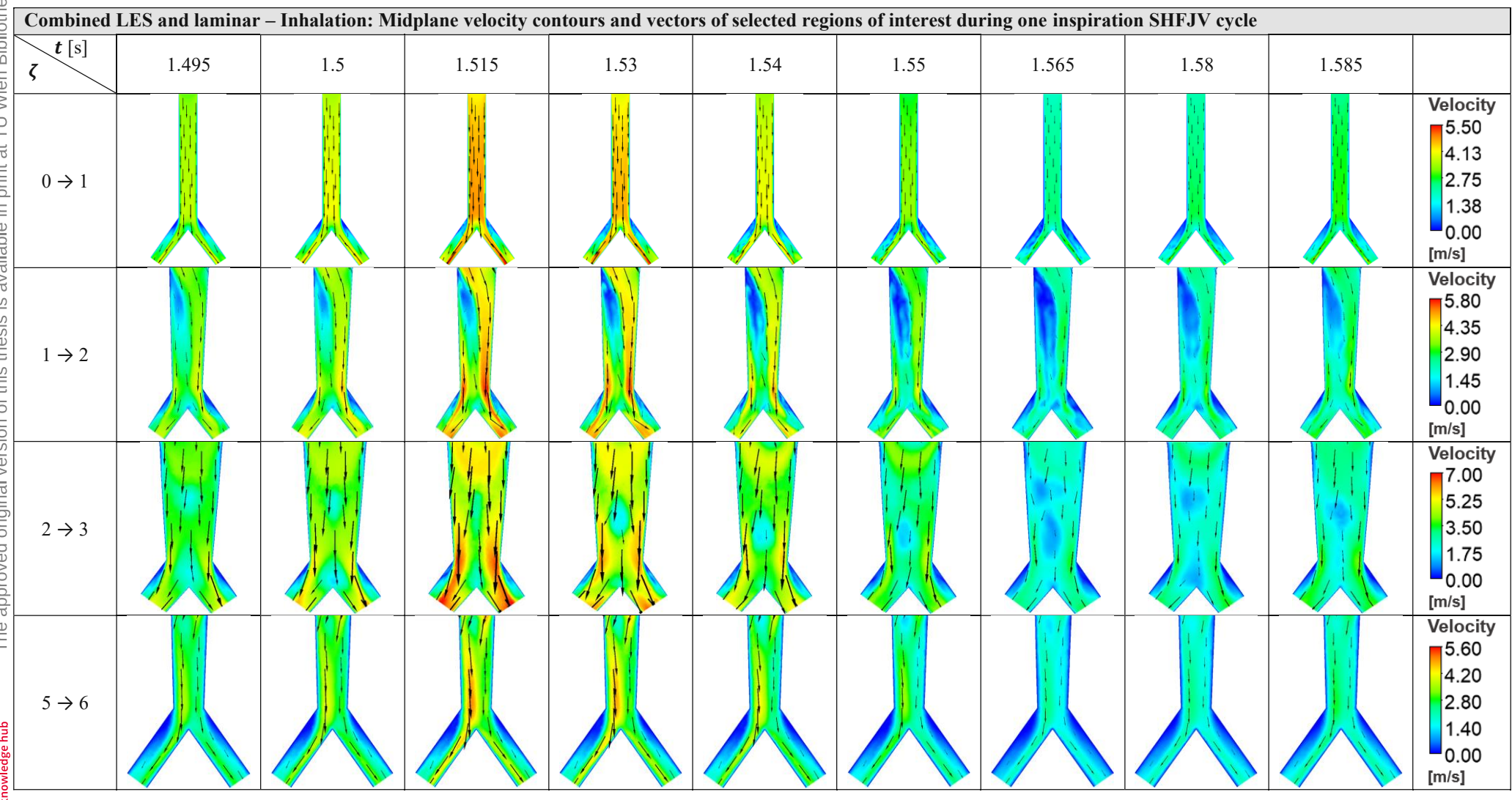


Table 21: Midplane velocity contours and vectors of selected regions during one cycle of HFJV. Results taken from the combined LES and laminar "Baseline" simulation.

Appendix A: Midplane velocity contours during SHFJV



## Appendix A: Midplane velocity contours during SHFJV

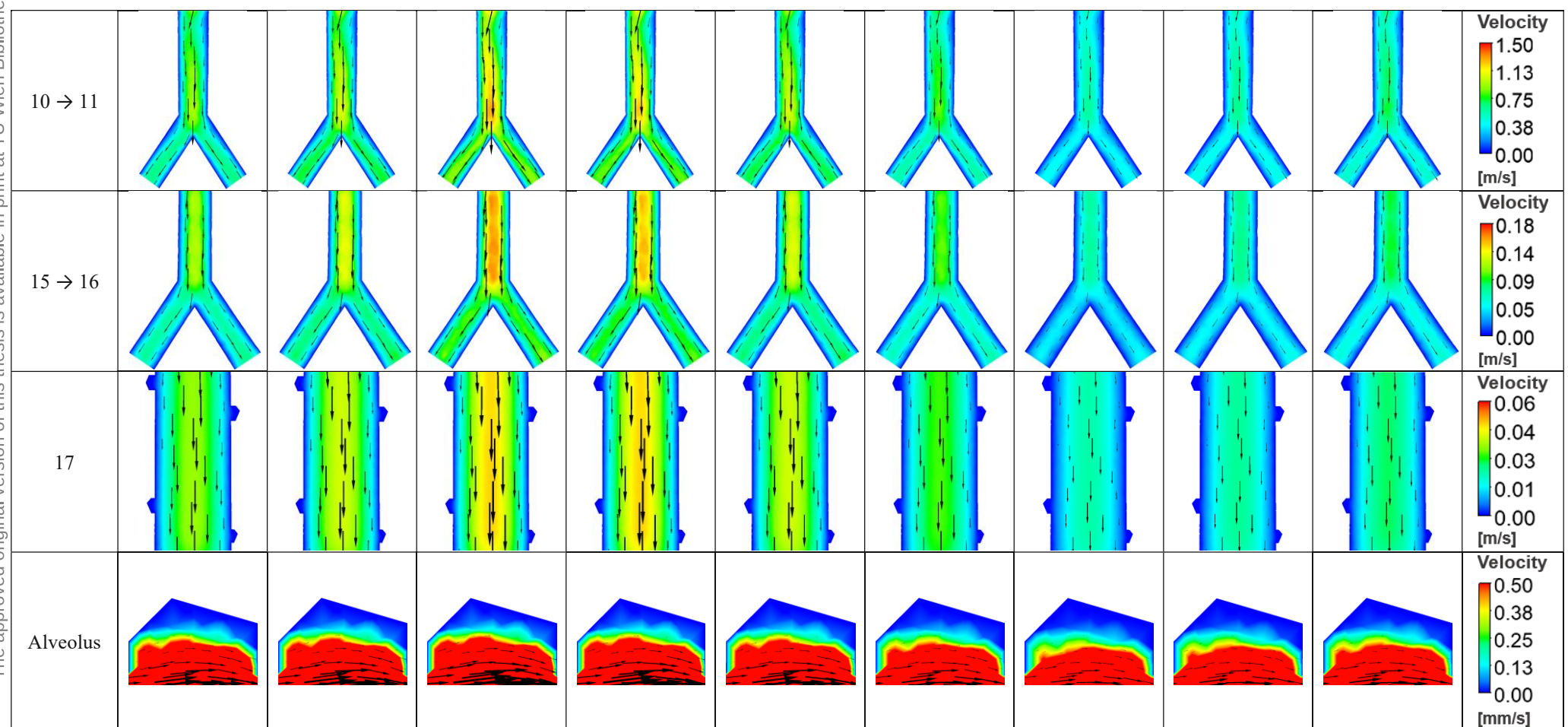
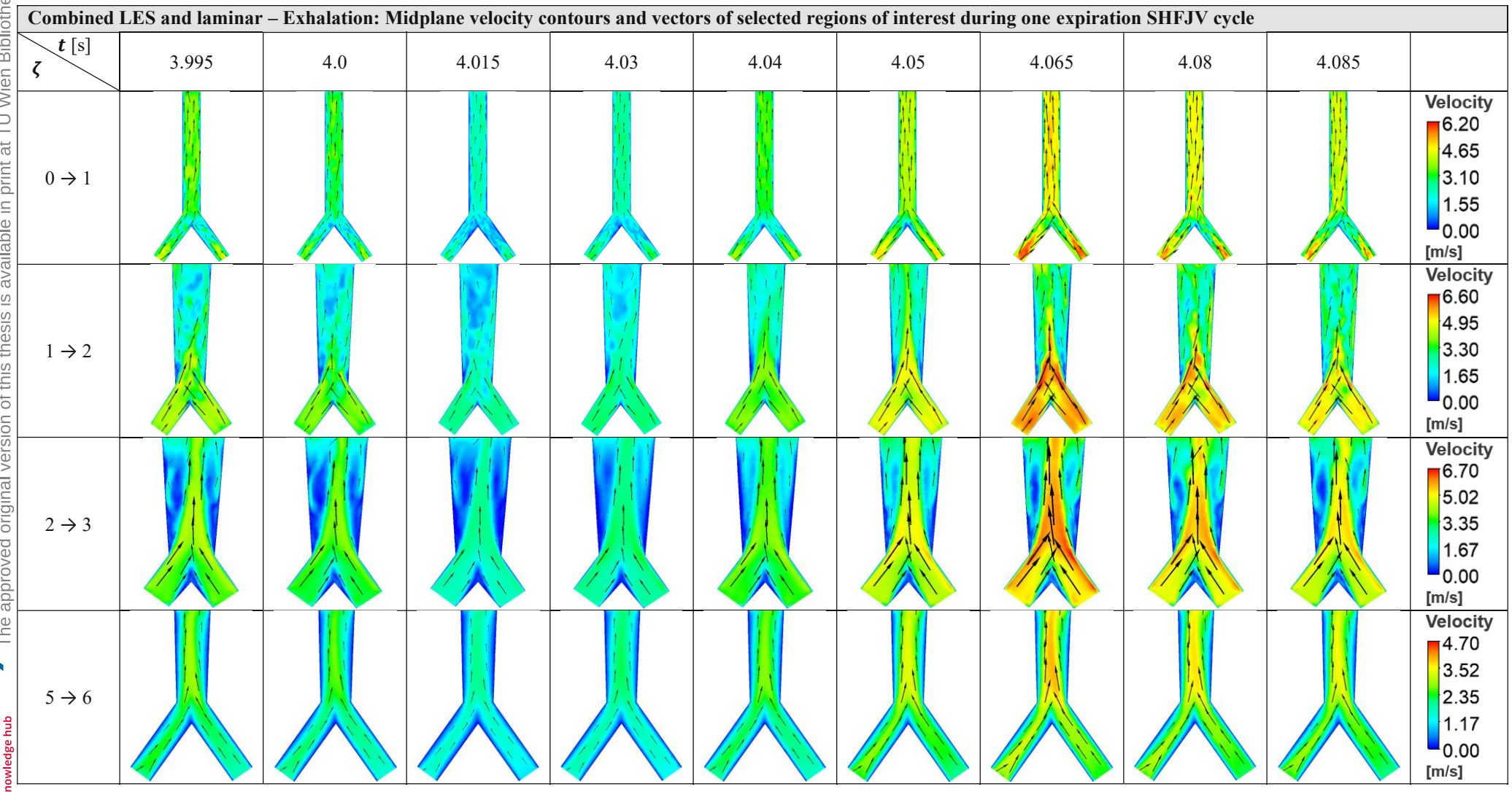
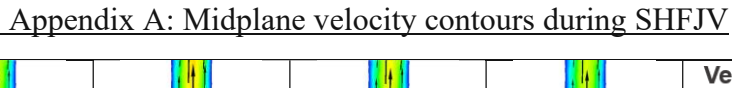


Table 22: Midplane velocity contours and vectors of selected regions during one inspiration cycle of SHFJV. Results taken from the combined LES and laminar "Inhalation" simulation.

Appendix A: Midplane velocity contours during SHFJV





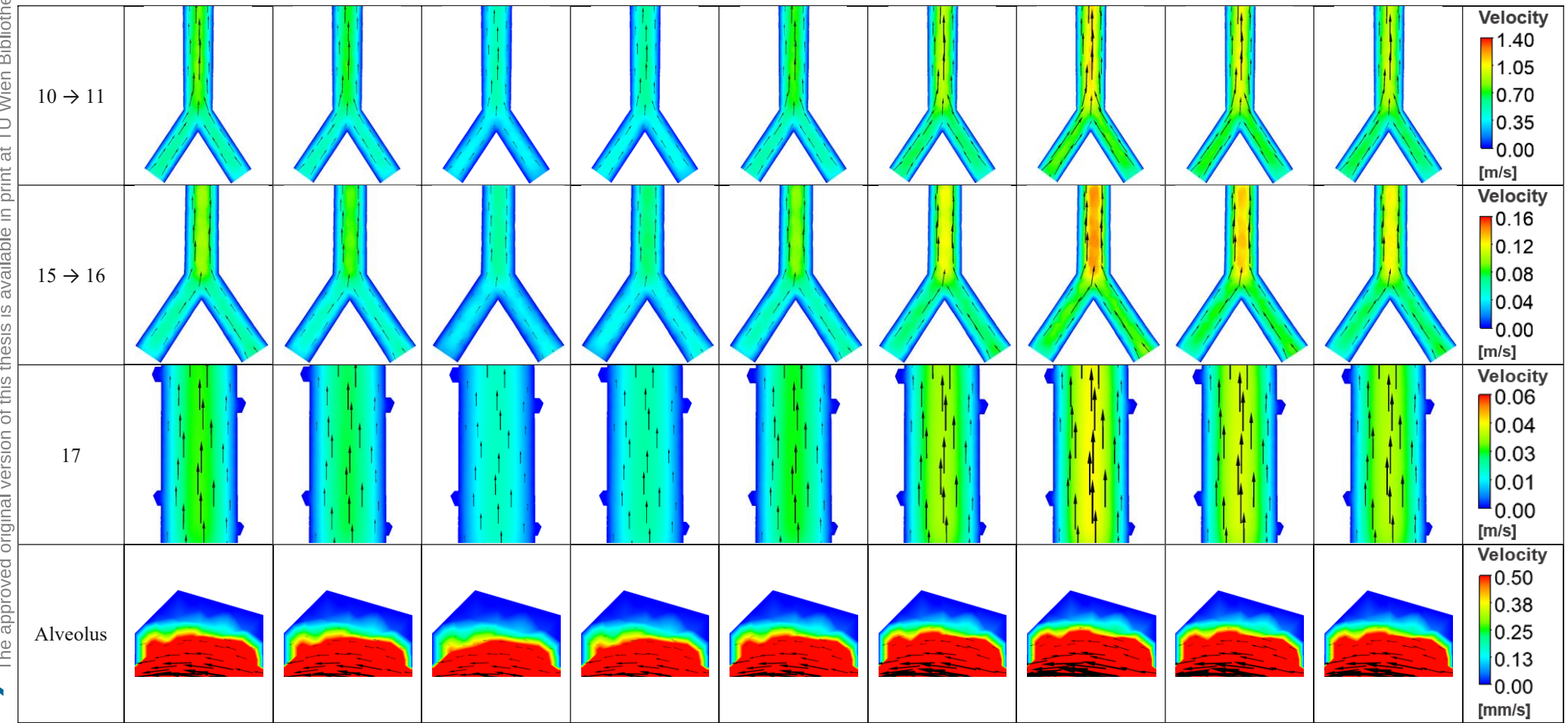
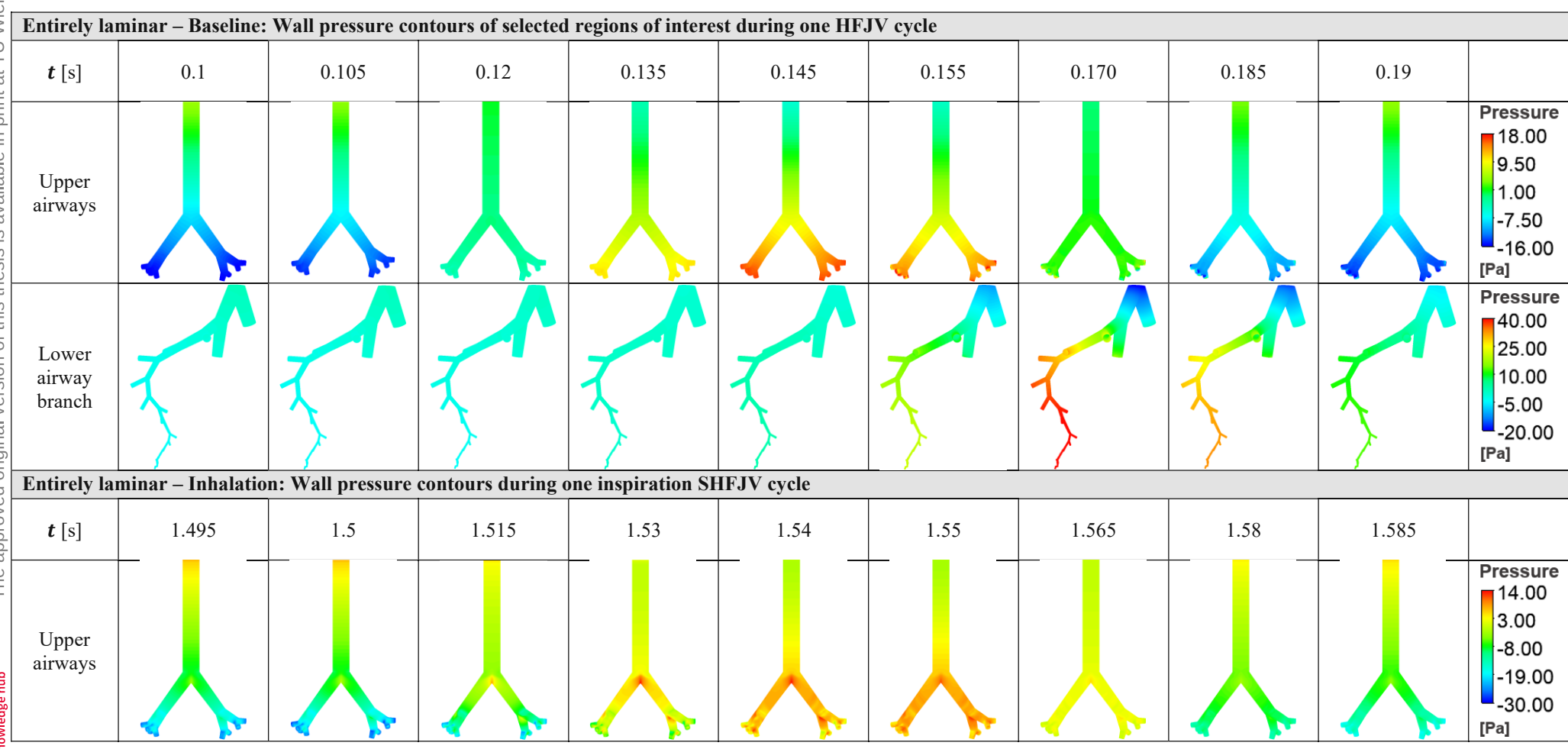
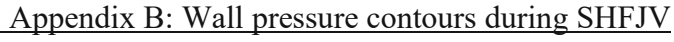


Table 23: Midplane velocity contours and vectors of selected regions during one expiration cycle of SHFJV. Results taken from the combined LES and laminar "Exhalation" simulation.

# Appendix B: Wall pressure contours during SHFJV





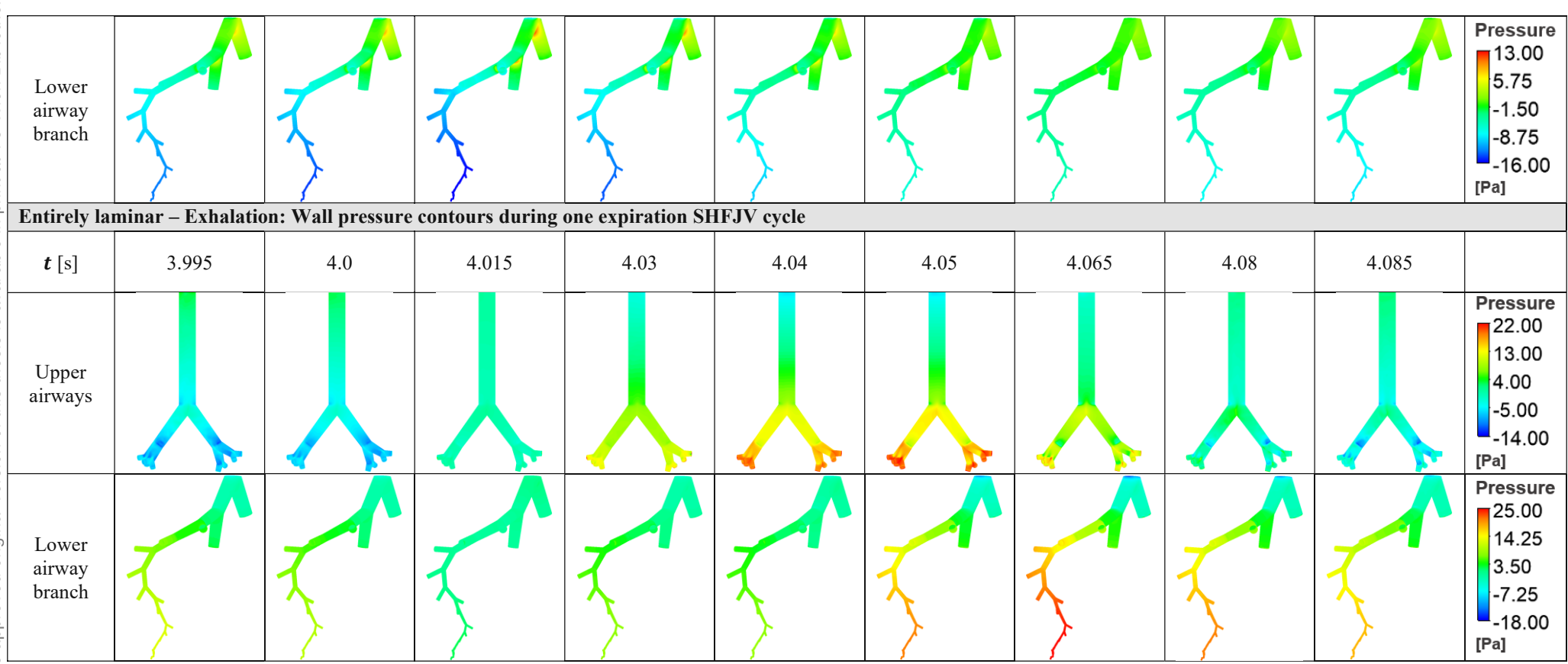
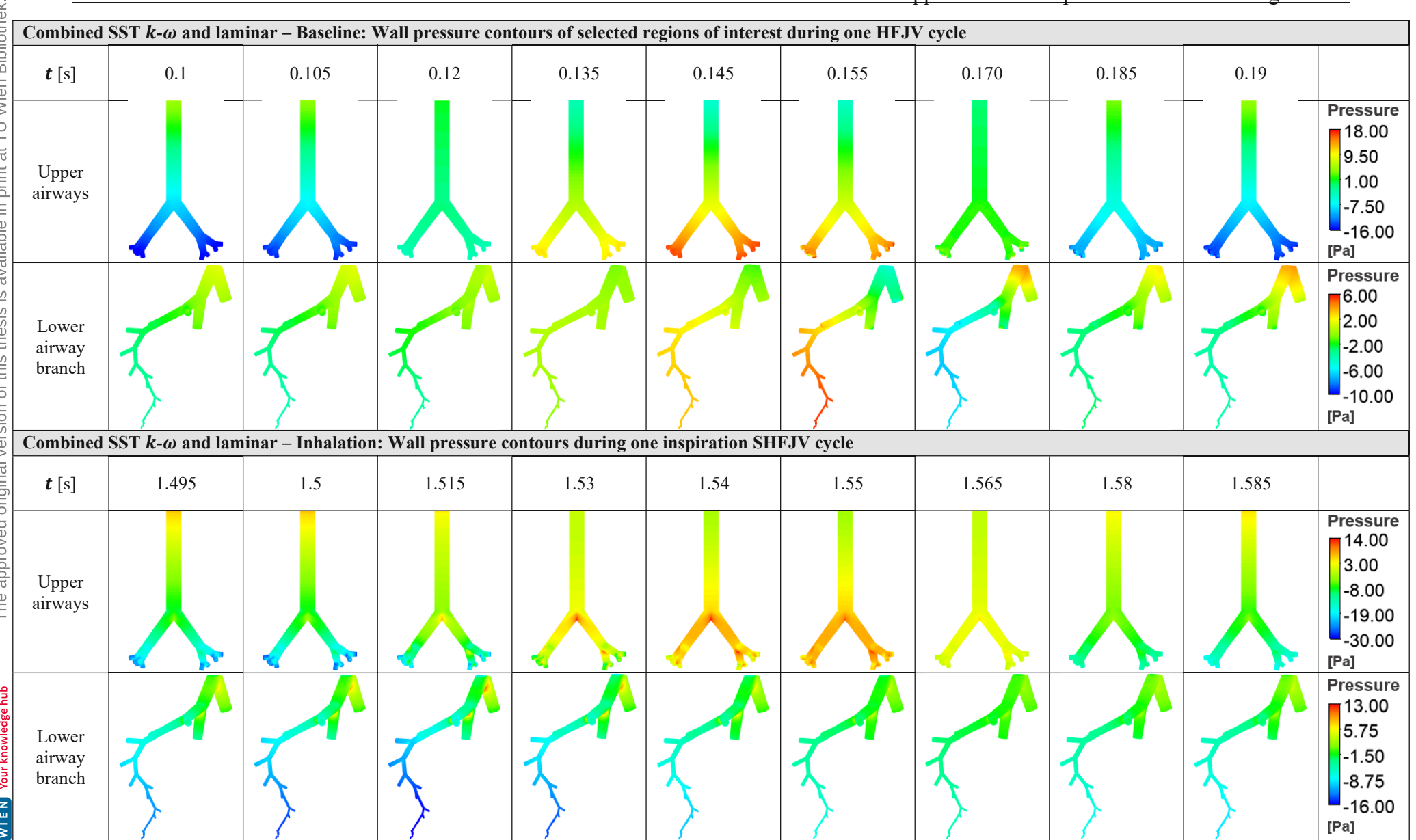


Table 24: Wall pressure contours of the upper airways and lower airway branch during examined subcycles of SHFJV. Results taken from the entirely laminar simulations.

Appendix B: Wall pressure contours during SHFJV



# Appendix B: Wall pressure contours during SHFJV

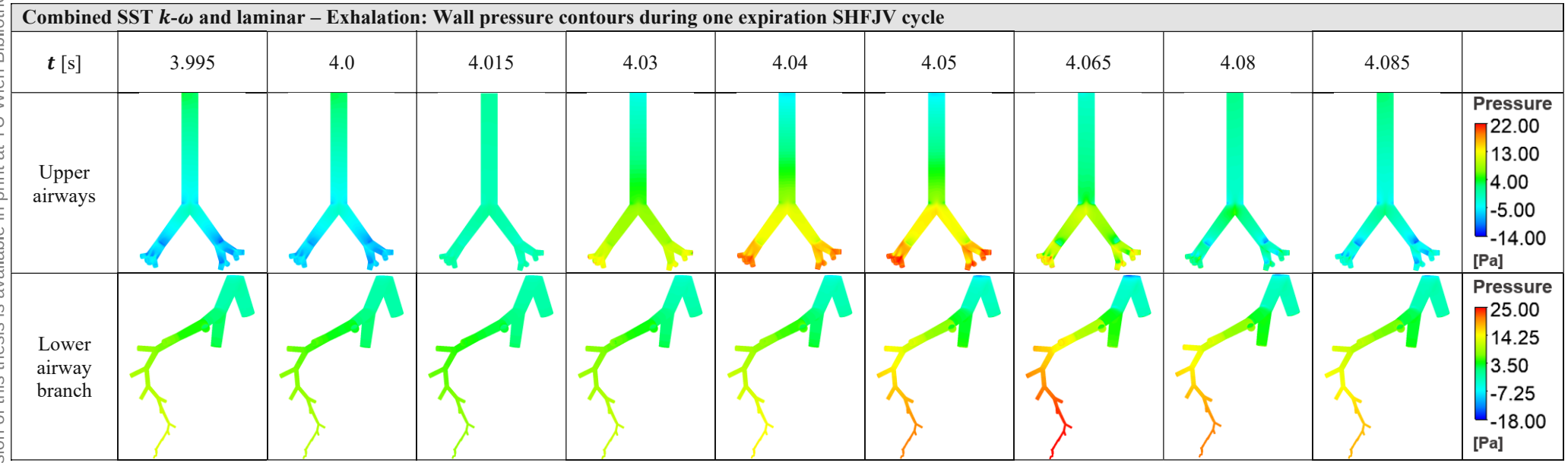
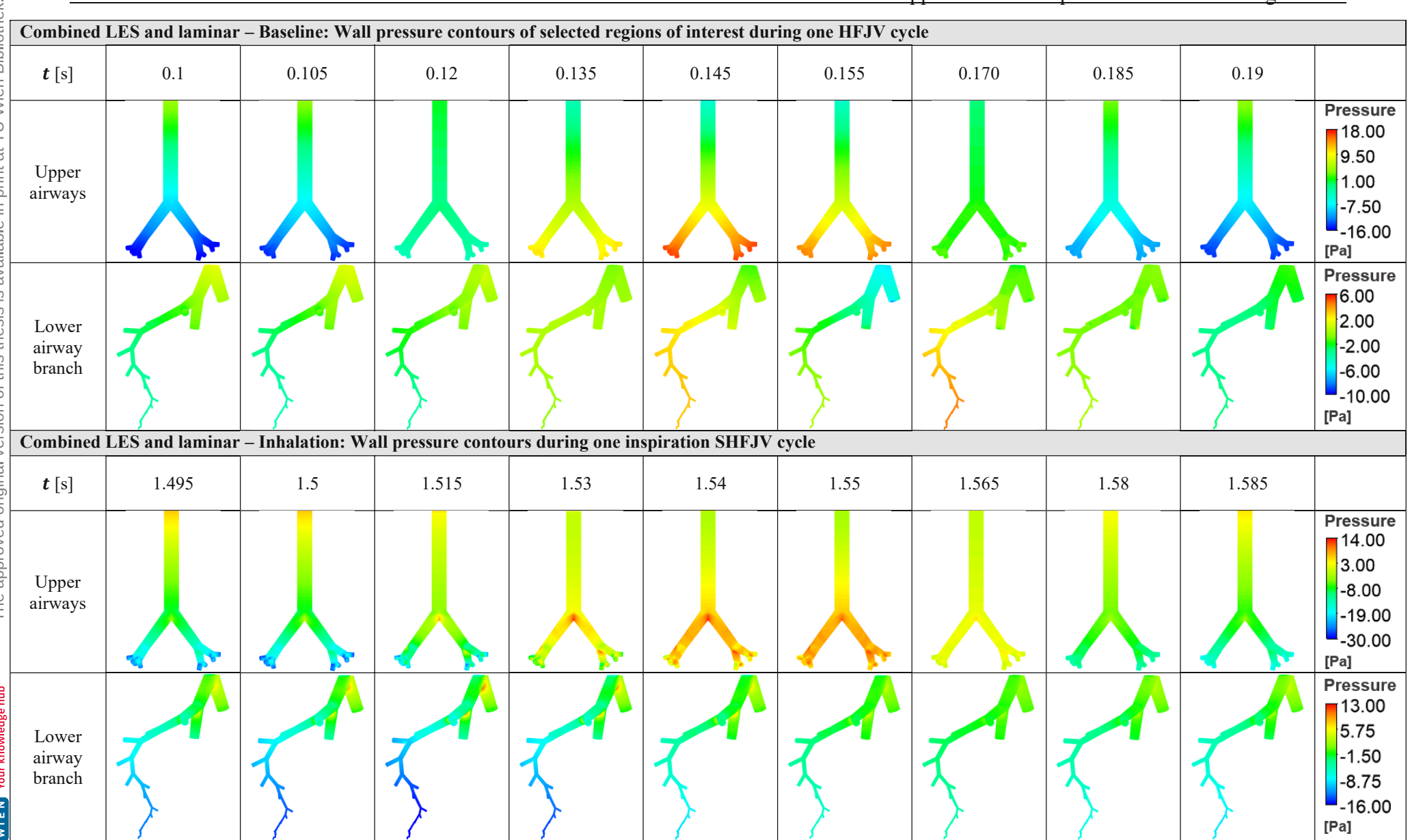


Table 25: Wall pressure contours of the upper airways and lower airway branch during examined subcycles of SHFJV. Results taken from the combined SST **k**-ω and laminar simulations.

Appendix B: Wall pressure contours during SHFJV



# Appendix B: Wall pressure contours during SHFJV

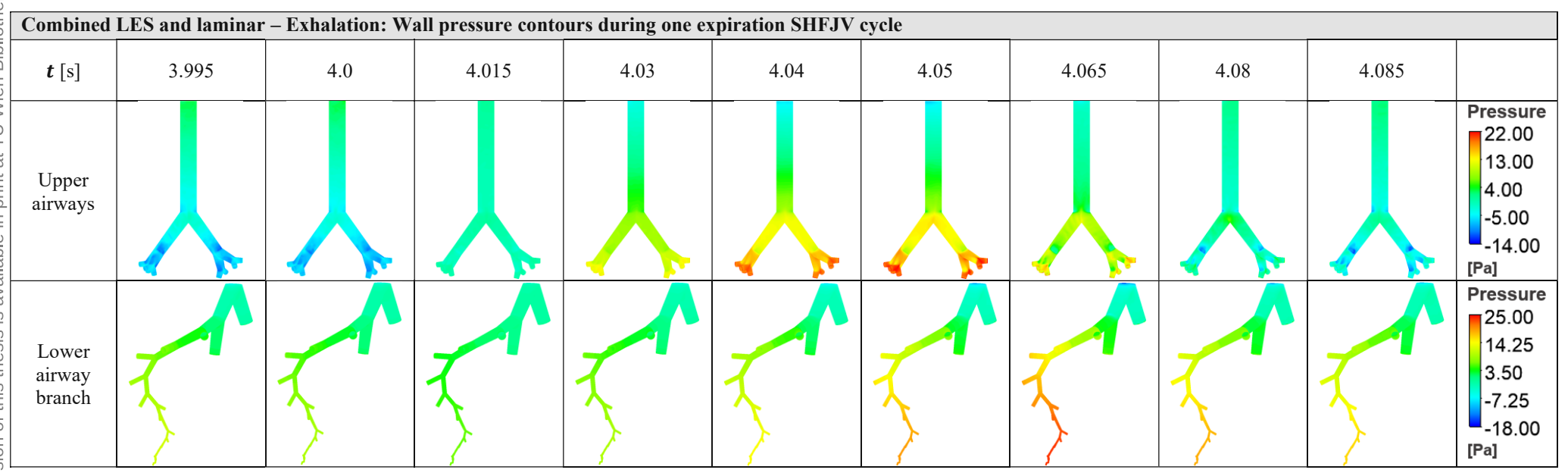


Table 26: Wall pressure contours of the upper airways and lower airway branch during examined subcycles of SHFJV. Results taken from the combined LES and laminar simulations.